DETECTION OF HIDDEN GRATINGS USING LIGHT AND SOUND

Stephen Edward

DETECTION OF HIDDEN GRATINGS USING LIGHT AND SOUND

Stephen Edward

Detection of hidden gratings using light and sound

Stephen Edward

Ph.D. Thesis, University of Amsterdam, June 2020
Detection of hidden gratings using light and sound
Stephen Edward

ISBN: 978-94-92323-36-1
Cover design: Zhuang-Yan Zhang

This work is carried out at the Advanced Research Center for Nanolithography (ARCNL), a public-private partnership of the University of Amsterdam (UvA), the Vrije Universiteit Amsterdam (VU), the Netherlands Organisation for Scientific Research (NWO), and the semiconductor equipment manufacturer ASML.

Detection of hidden gratings using light and sound

Academisch Proefschrift

ter verkrijging van de graad van doctor

aan de Universiteit van Amsterdam

op gezag van de Rector Magnificus

prof. dr. ir. K.I.J. Maex

ten overstaan van een door het College voor Promoties

ingestelde commissie,

in het openbaar te verdedigen

op donderdag 18 juni 2020, te 12:00 uur

door

Stephen Edward

geboren te Alappuzha, Kerala

Promotiecommissie

Promotor:

prof. dr. P. C. M. Planken	Universiteit van Amsterdam/ARCNL

Co-Promotor:

dr. S. Witte	Vrije Universiteit Amsterdam/ARCNL

Overige leden:

prof. dr. H. J. Bakker	Universiteit van Amsterdam/AMOLF
prof. dr. A. F. Koenderink	Universiteit van Amsterdam/AMOLF
prof. dr. H. B. van Linden van den Heuvell	Universiteit van Amsterdam
prof. dr. I. Setija	ASML/Technische Universiteit Eindhoven
prof. dr. H. P. Urbach	Technische Universiteit Delft

Faculteit der Natuurwetenschappen, Wiskunde en Informatica

Contents

1 Introduction **1**

2 Theory **7**
2.1 Introduction 7
2.2 Theory of laser-induced acoustic wave generation, propagation and detection 8
2.2.1 Acoustic wave generation 9
2.2.2 Acoustic wave propagation 11
2.2.3 Optical detection of the acoustic wave 12
2.3 Fraunhofer diffraction from a displaced grating 14
2.4 Transient-grating pump-probe setup 17

3 Experimental details **21**
3.1 Laser system 21
3.2 Pump-probe setup 23
3.3 Determining the pump-probe temporal overlap 24
3.3.1 Sum-frequency generation 24
3.3.2 Transient grating in BBO 26
3.4 Sample preparation 27

4 Detection of gratings through opaque metal layers by optical measurements of ultrafast electron dynamics **31**
4.1 Introduction 32
4.2 Experimental setup 33
4.3 Numerical calculations 35
4.3.1 Laser pulse absorption calculation 35

4.3.2 Two temperature model 37
4.4 Results and Discussion 39
4.4.1 Dependence of electron dynamics on Au layer thickness 40
4.4.2 Electron dynamics in Gold-Platinum bilayers 43
4.4.3 Electron dynamics in bilayers with other metals . . . 48
4.4.4 Detection of a buried grating 50
4.5 Conclusion 53

5 Acoustic waves in flat metal and dielectric layers 55
5.1 Introduction 56
5.2 Experimental setup 57
5.3 Results and discussion 57
5.3.1 Acoustic waves in Au 57
5.3.2 Acoustic waves in Ni and W 62
5.3.3 Acoustic waves in Au-SiO_x-Au samples 66
5.4 Conclusion 70

6 Detection of gratings buried underneath multi-layer dielectrics and metallic layers 71
6.1 Introduction 72
6.2 Experimental setup 74
6.2.1 Sample fabrication 75
6.3 Results and discussion 76
6.3.1 Grating under flat metal layer 76
6.3.2 Complex multilayer samples 84
6.3.3 Effective acoustic properties of the bilayer dielectric stack 88
6.3.4 Optical excitation of Au and Ni layers 90
6.3.5 Displacement amplitude at the glass-metal interface 92
6.3.6 Linear reflectance measurements on multi-layer sample 94
6.3.7 Visualization of strain propagating in “Au-multilayer” sample 96
6.3.8 Material properties 99
6.4 Conclusion 100

7 Detection of low amplitude buried gratings and the role of

surface roughness **103**
7.1 Introduction 104
7.2 Experimental setup 105
7.3 Results and discussion 107
7.3.1 Pump-probe experiments and simulation 107
7.3.2 Displacement of glass-Ni interface 110
7.3.3 Strain-optic effect in glass substrate 111
7.3.4 Strain-optic effect in Ni 112
7.3.5 Thermal grating in Ni 112
7.3.6 Surface roughness 113
7.3.7 All contributions combined: 117
7.4 Conclusion 119

Bibliography **121**

Summary **135**

Samenvatting **139**

Acknowledgements **145**

1 Introduction

The semiconductor industry has driven many technological developments over the past several decades. As a result, we have phones nowadays that have 100,000 times the processing power of the computer aboard the Apollo 11 spacecraft that landed a man on the moon in 1969 [1]. The manufacturing of modern-day computer chips is an extremely complicated process that involves various repetitive processing steps. One of the most critical steps in the whole process is that of photolithography [2]. Photolithography is the process that uses light to transfer a specific pattern from a mask to a light-sensitive material (a photoresist), which is deposited onto a silicon wafer. The photolithography techniques used in today's semiconductor industry require various complicated processing steps. A basic scheme of photolithography is illustrated in Figure 1.1. The process starts with spin-coating a photoresist onto a chemically cleaned silicon wafer substrate. The photoresist is then irradiated with UV light through a photo-mask to induce chemical reactions, which changes its solubility. The silicon wafer is then washed in a developer solution to remove either the part of the resist exposed to UV light or the portion which was unexposed to the UV light. As a result, the pattern on the mask is transferred to the resist. Finally, in the etching process, the etching agents remove the uppermost layer of the substrate in areas that are not protected by the photoresist, and the pattern from the mask is on the silicon substrate [2].

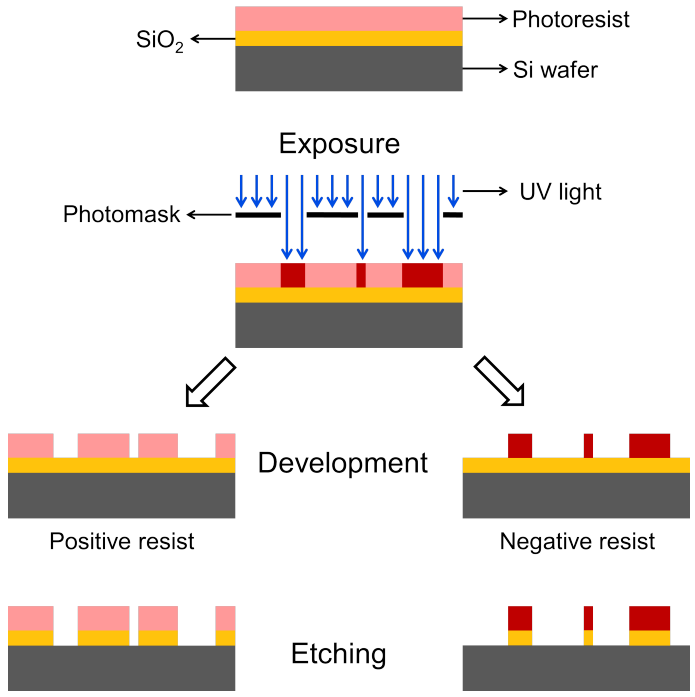

Figure 1.1: Simplified illustration of the various steps involved in photolithography

The need for faster and cheaper computer chips has pushed the semiconductor industry to improve the design of integrated circuits along with reducing the size of transistors. The shrinking of transistor size has been achieved with the help of improvements in the processing steps in the chip manufacturing procedure. In 1965, a prediction was made by Gordon Moore, co-founder of Intel, that the number of transistors in an integrated circuit doubles approximately every year [3]. Ten years later, in 1975, he revised the forecast rate to doubling every two years [3–5]. In the past several decades, the semiconductor industry has followed the predictions set down by Moore's law, which has subsequently been used to guide future plans and to set targets for research and development. Figure 1.2 shows that the number of transistors per microprocessor over the few decades has approximately doubled every two years [6].

The technological developments in nano-lithography have lead to the production of semiconductor devices with feature sizes as small as 7 nm [7].

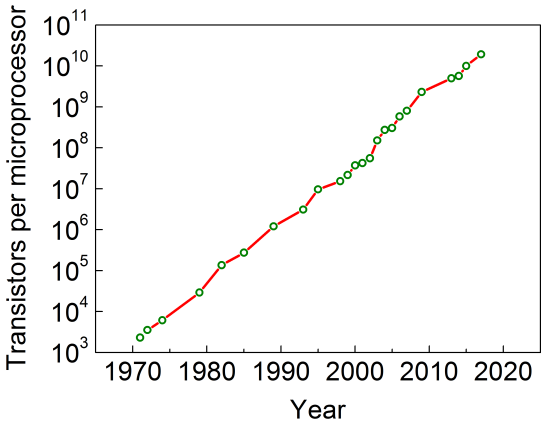

Figure 1.2: Number of transistors per microprocessor as a function of the year of introduction [6].

The size of the smallest features which can be printed, commonly referred to as the critical dimension (CD), is given by the well-known Rayleigh equation [8],

$$\mathrm{CD} = k_1 . \frac{\lambda}{\mathrm{NA}}, \tag{1.1}$$

where k_1 is a constant related to the lithographic process, λ is the wavelength of the light used in the exposure of the resist, and NA is the numerical aperture of the optical system. In the past few decades, the continuous lowering of the CD was made possible by improving all three of these parameters. The exposure wavelength λ was scaled down in steps from 436 nm to 365 nm, 248 nm, and 193 nm while the numerical aperture was increased to a hyper-NA of 1.35 using immersion lithography in the systems that use an exposure wavelength of 193 nm [9]. These improvements were combined with multi-patterning techniques to achieve a CD of 10 nm. Recently, the industry has moved to 13.5 nm exposure wavelength with an NA of 0.33, which allows printing of features down to 7 nm [7] or even smaller [10, 11]. This shrinking of feature size allows the manufacturers to increase the density of transistors in a modern chip and increase memory density in a storage device.

To print such extremely small features, alignment sensors must be used in the lithography machines that measure the lateral position of the wafer

inside the machine. The wafer needs to be positioned with sub-nanometer accuracy in order to print new patterns on the resist, on top of the underlying product patterns. Modern nanolithography machines use optical tools that measure wafer location at many (≈20–40) points on a wafer to determine the wafer distortion and therefore align the wafer with sub-nanometer accuracy. In order to perform these measurements, many gratings, called alignment gratings, are etched into the area between the individual product dies in the Si wafer. These gratings are illuminated with a light source, and optical sensors measure the diffracted orders emerging from the grating. A small translation of the wafer in the direction of the grating wavevector has no effect on the diffraction efficiency. However, it does change the optical phase-difference between the $+n^{th}$ and $-n^{th}$ diffracted orders (n=1,2,3,..). A change in the phase difference between, for example, the $+1^{st}$ and -1^{st} order diffracted beams can be measured by interfering the two beams. Measuring these changes makes it possible to align wafers with an accuracy of less than a nanometer [12].

Unfortunately, this optical technique works as long as the materials deposited on top of the alignment gratings, during the semiconductor device fabrication, are transparent to light. Therefore such an optical sensor is inadequate when it comes to detecting alignment gratings buried under optically opaque materials. This is the case during the fabrication of the new generation, 3D NAND flash memory. In 3D NAND, rather than a single layer of small memory cells in a side by side layout, multiple memory cells are stacked on top of each other, increasing the memory density [13–17]. A 3D NAND memory consists of thin alternating layers of silicon oxide and nitride films on a silicon substrate. A thick hard-mask layer, most often opaque to visible/IR light, is deposited on top of the oxide/nitride stack. The hardmask layer is essential to protect the patterned areas during the etching process, which comes after the lithography step in the manufacturing of a 3D NAND memory. The new generation of 3D NAND has up to 100 pairs of oxide/nitride layers and hardmasks that are few microns thick. Unfortunately, the all-important alignment gratings that are etched in the silicon wafer get buried under hundreds of dielectric layers and also under the thick hard-mask [13, 16]. As a result, the alignment gratings are invisible or difficult to detect with visible and IR light, while using light

with wavelengths in the UV range is not possible due to the risk of resist exposure [12]. This poses a big challenge for wafer alignment in the nanolithography industry [6].

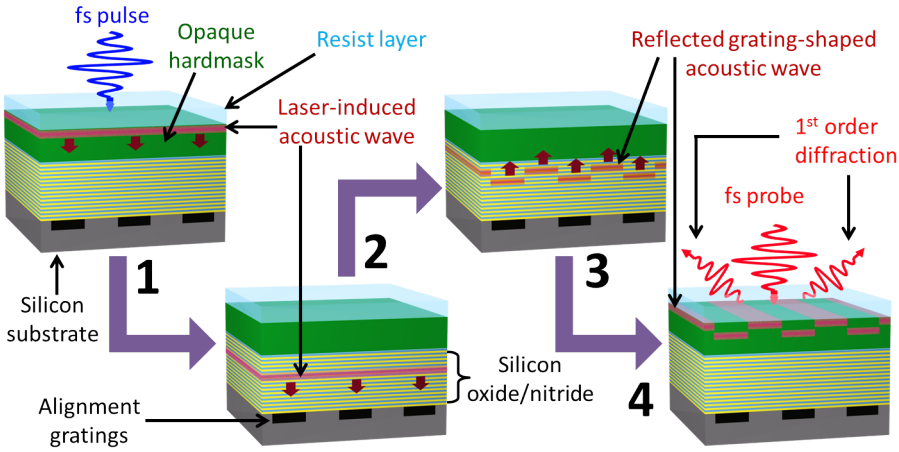

Figure 1.3: Schematic explaining the technique to detect buried gratings underneath optically opaque materials using laser-induced ultrasound.

Fortunately, materials that are opaque to visible/IR light are often transparent to sound. Therefore, in this thesis, the use of laser-induced ultrasound waves is proposed to detect hidden alignment gratings. This concept is based on the fact that ultrafast laser pulses can generate acoustic waves inside different materials (step 1 in Figure 1.3). These ultrasound waves have the ability to propagate through optically opaque materials, and can, therefore, probe an alignment grating in situations where light can not penetrate (step 2 in Figure 1.3). These ultrasound waves reflect from the alignment grating and propagate back towards the surface of the stack. The shape and amplitude of the alignment grating is encoded on the spatial phase of the reflected ultrasound wave (step 3 in Figure 1.3). This returning grating-shaped acoustic wave can be probed by optical means, as it gives rise to two optically observable effects: i) the returning wave causes a grating-like physical displacement of the surface and, ii) the stress related to the acoustic waves induces a grating-like change to the optical constants of the surface via the strain-optic effect. By diffracting a second, time-

delayed optical pulse from the surface at the return time of the acoustic wave, the acoustic response from the buried target can be detected (step 4 in Figure 1.3). This alignment concept combines the speed and resolution of optical detection with the penetration depth of ultrasound waves.

Outline of this thesis

This thesis demonstrates the application of laser-induced ultrasound to detect buried gratings in the context of wafer alignment and aims to improve the understanding of light-metal interactions. This is the culmination of the work performed in the 'Light-Matter Interaction' group (formerly 'EUV Targets') , in collaboration with the 'EUV Generation and Imaging' group at the Advanced Research Center for Nanolithography (ARCNL), Amsterdam.

In Chapter 2, the theory underlying the generation, propagation, and detection of laser-induced acoustic waves is discussed. A description of the laser amplifier, details of the experimental setups, and details of the sample fabrication are presented in Chapter 3. Chapter 4 address the first step in the formation of an acoustic wave: heating and cooling of the electron gas. The demonstration of how ultrafast electron dynamics can be used to detect the presence of gratings buried underneath optically opaque gold layers is also discussed in this chapter. In Chapter 5, the results of transient-grating photoacoustic pump-probe experiments on different metals and bi-layer samples are presented. The detection of buried gratings on a sample similar to that of a 3D NAND is shown in Chapter 6. The effect of multiple dielectric interfaces in the propagation of acoustic waves is discussed in this chapter. Finally, the limits and sensitivity of this technique are studied in Chapter 7, where the amplitude of the buried grating is reduced to below 1 nm. Here the significant role played by interface roughness in understanding the pump-probe measurements is discussed.

2

Theory

2.1 Introduction

The study of materials using femto/picosecond laser-induced high-frequency acoustic waves is usually referred to as laser-induced ultrasonics, or femto or picosecond ultrasonics. When ultrafast laser pulses (typically < 1 ps in duration) are incident on absorptive solids, some part of the optical energy is absorbed and converted to heat. The rapid heating of the lattice leads to thermal stress, which launches a strain wave propagating in all directions. In this thesis, we mainly focus on the longitudinal acoustic waves in metals generated using femtosecond optical pulses, which are acoustic waves propagating normal to the surface with frequencies in the gigahertz (GHz) to terahertz (THz) range.

An advanced numerical model developed by Hao Zhang, which captures the generation, propagation, and detection of high-frequency acoustic waves by ultrafast laser pulses, is used to simulate the experimentally measured diffracted signals [18]. The model consists of three main parts, (i) absorption of light and the subsequent generation of the acoustic wave, (ii) propagation of the acoustic wave, (iii) detection of the acoustic wave. The

absorption of the femtosecond laser pulse and the subsequent heating and cooling of the electron gas inside a metal layer is described by the well-known Two Temperature Model (TTM) [19–24]. The heating of the lattice calculated from the TTM sets up an isotropic thermal stress, which leads to the generation of the high-frequency acoustic wave. The equation of motion for an isotropic, linear elastic wave is used to describe the propagation of the acoustic wave inside the metal and dielectric layers. Finally, by propagating the complex electric field of the light pulse after the optical excitation by the femtosecond laser pulse, through the sample, we can calculate the diffraction efficiency as a function of time delay. The model calculates the first-order diffracted signal by accounting for the spatially periodic changes in the refractive index due to the thermo-optic effect and the strain-optic effect, and the spatially periodic displacement of the surface. In this chapter, we explain the theory underlying the generation, propagation, and detection of acoustic waves in metal layers, which is used in the numerical model.

2.2 Theory of laser-induced acoustic wave generation, propagation and detection

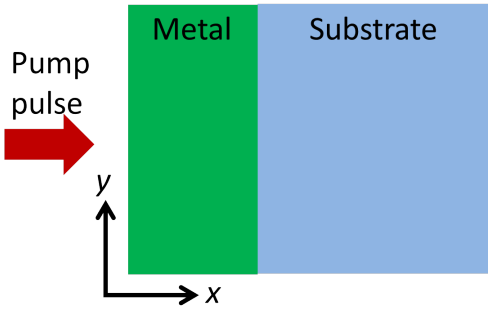

Figure 2.1: Schematic depiction of a metal on a substrate. The laser pulse is incident from x <0. The coordinate directions are used throughout this section.

The model solves a set of time-dependent equations in two spatial dimensions, x and y. In the convention we use, the pump pulse is incident along the x-axis, and when the sample has a buried grating, the k-vector of the grating is along the y-axis (see Figure 2.1).

2.2.1 Acoustic wave generation

The first step in laser-induced ultrasonics is the absorption of the femtosecond pulse, which causes the rapid heating of the lattice. To calculate the intensity of light absorbed inside a thick metal layer, we can use a simple Lambert-Beer law with a correction term for the reflection. This is sufficient to describe laser intensity attenuation inside the sample. Therefore, the intensity of the light inside the layer $I(x, y, t)$ can be written as,

$$I(x, y, t) = (1 - R)I_0(x, y, t)e^{(-x/L)}, \tag{2.1}$$

where R is the reflectivity of the sample, I_0 is the intensity of the incident laser pulse, and L is the optical penetration depth. The optical penetration depth is related to the absorption coefficient α at the pump wavelength by $L = 1/\alpha$. The relation in Eq. 2.1 describes the absorption of the pump light when the thickness of the metal layer is much larger than the optical penetration depth. When the layer thickness is smaller than the optical penetration depth, or for multilayered structures where reflections at each interface must be considered, the transfer matrix method [25,26] is a more suitable method to calculate the intensity of the absorbed light. If the absorption layer contains sub-wavelength structures, optical near field effects become important, and in this case, a more general method for the solution of Maxwell's equations must be used. After calculating the intensity distribution of light inside the metal, we can calculate the increase in lattice temperature $\Delta T_l(x, y, t)$ using the two-temperature model [19]. The two temperature model, originally proposed by Anisimov et al. [19], is a widely used phenomenological model that describes electron-lattice dynamics after optical excitation with a laser pulse. In this model, the electron gas is assumed to be thermalized at all times during and after excitation and is described by a time-dependent temperature T_e. The lattice is also described as having a time-dependent temperature T_l. For time scales greater than the electron thermalization time (which is smaller than a few hundred femtoseconds for most metals), the two-temperature model provides a good description of the spatial and temporal evolution of electron temperature T_e and lattice temperature T_l. The electron gas and the lattice, exchange energy through electron-phonon coupling, which tends to equilibrate the two temperatures. The equation describing the electron gas temperature

includes a source term $S(x, y, t) = \alpha I(x, y, t)$, which describes when and where energy is deposited in the metal layer by the laser pulse. Initially, the optical energy is absorbed by the electron gas system, increasing the electron temperature while the lattice remains at room temperature. The hot electron gas diffuses into the metal layer and transfers energy to the lattice subsystem, as described by the following coupled equations [27, 28]

$$\begin{aligned} C_e(T_e)\frac{\partial T_e}{\partial t} &= \nabla \cdot K_e \nabla T_e - g(T_e - T_l) + \alpha I(x, y, t), \\ C_l \frac{\partial T_l}{\partial t} &= \nabla \cdot K_l \nabla T_l + g(T_e - T_l), \end{aligned} \tag{2.2}$$

where C_e and C_l are the respective heat capacities of the electron gas and lattice respectively, K_e and K_l denotes the thermal conductivities of the electron gas and the lattice respectively, and g is the electron-phonon coupling constant [27, 28]. The temperature dependence of lattice heat capacity, lattice thermal conductivity as well as electron-phonon coupling strength are neglected as the lattice temperature increase in our experimental conditions is calculated to be only a few tens of K. We use the relations $C_e = A_e T_e$ and $K_e = K_0 \times T_e/T_l$ [21] and solve the TTM numerically to calculate the time evolution of the electron temperature T_e and the lattice temperature T_l. Here, A_e is the electron specific heat constant and K_0 is the thermal conductivity at 273 K.

In metals, the rapid increase of the lattice temperature $T_l(x, y, t)$ sets up an isotropic thermal stress σ^{th} which is the dominant mechanism for acoustic wave generation [29, 30]. This is this source term for the acoustic wave generated in the metal layer. The relation between the thermal stress and lattice temperature change $\Delta T_l(x, y, t)$ is given by,

$$\sigma_x^{th} = \sigma_y^{th} = -3B\beta\Delta T_l(x, y, t), \tag{2.3}$$

where $\sigma_x^{th} = \sigma_y^{th}$ are the two cartesian components of the thermal stress, B is the bulk modulus of the metal and β denotes the linear expansion coefficient. We solve the two-temperature model using Eq. 2.2, to obtain the lattice temperature increase $\Delta T_l(x, y, t)$. With this, we can calculate the thermal stress σ^{th} using Eq. 2.3.

2.2.2 Acoustic wave propagation

The propagation of an acoustic wave in a metal can be described by the equation of motion for an isotropic, linear elastic wave [31, 32] where the source term is given by Eq. 2.3. Therefore, the displacement vector $\vec{u}$ of the material can be written as,

$$\rho\frac{\partial^2\vec{u}}{\partial t^2} = \mu\nabla^2\vec{u} + (\mu+\lambda)\nabla(\nabla\cdot\vec{u}) + \nabla\sigma^{th} \tag{2.4}$$

where ρ is the mass density of the material, λ and μ are the so-called two Lamé parameters in the stress-strain relationship.

Expanding Eq. 2.4 in two-dimensional cartesian coordinate leads to the equations for the velocity components v_x and v_y [18],

$$\begin{aligned}\frac{\partial v_x}{\partial t} &= -\frac{1}{\rho}(\frac{\partial\sigma_x^{re}}{\partial x} + \frac{\partial\sigma_{xy}^{re}}{\partial y} - \frac{\partial\sigma_x^{th}}{\partial x}),\\ \frac{\partial v_y}{\partial t} &= -\frac{1}{\rho}(\frac{\partial\sigma_y^{re}}{\partial y} + \frac{\partial\sigma_{xy}^{re}}{\partial x} - \frac{\partial\sigma_y^{th}}{\partial y}).\end{aligned} \tag{2.5}$$

where, σ_x^{re},σ_y^{re} are the normal stress components and σ_{xy}^{re} is the shear stress. Here,

$$\begin{aligned}\sigma_x^{re} &= -(\lambda+2\mu)s_x - \lambda s_y;\quad \sigma_y^{re} = -(\lambda+2\mu)s_y - \lambda s_x,\\ \sigma_{xy}^{re} &= -\mu s_{xy}.\end{aligned} \tag{2.6}$$

where s_x and s_y are the components of normal strain and s_{xy} the shear strain. The superscript "re" stands for "restoring" as they originate from the restoring force. Eq. 2.6 is known as the strain-stress relation. The definition of normal and shear strain come with the expansion as well, i.e.,

$$s_x = \frac{\partial u_x}{\partial x};\quad s_y = \frac{\partial u_y}{\partial y};\quad s_{xy} = \frac{\partial u_x}{\partial y} + \frac{\partial u_y}{\partial x}. \tag{2.7}$$

The equation of motion described in Eq. 2.4 does not include damping. Acoustic damping is included in the model by adding two viscous terms to the equation of motion [33, 34]. Also, the model we use in the numerical simulations includes relaxation damping [35–37]: the sound waves disturb

the distribution function of the thermal phonons, and the return of the system to equilibrium through phonon collisions removes energy from the sound wave. The details of the model explaining how the various damping terms are added are discussed in [18].

2.2.3 Optical detection of the acoustic wave

In a laser-induced ultrasonics pump-probe experiments, the probe pulse detects the response of the material to the presence of an acoustic wave. This is usually done by measuring changes in the sample reflectivity [38], by measuring diffraction efficiency in the case of transient-grating experiments [39, 40] or by using interferometric measurements [41, 42] where the electric-field amplitude and phase of the probe pulse are measured simultaneously. In our experiments, we measure the change in the intensity of the diffracted probe pulse induced by the pump pulse. Diffraction of the probe pulse can arise due to (i) a spatially periodic displacement of the surface, (ii) a spatially periodic change in the refractive index in a layer near the surface, or (iii) a combination of both effects. A change in the refractive index of a medium due to the presence of an acoustic strain wave is commonly referred to as the strain-optic effect. In addition to this, spatially periodic lattice temperature variations at the surface can also give rise to grating-like changes in the refractive index near the surface. A change in the refractive index of a medium due to a temperature change is commonly referred to as the thermo-optic effect.

The transient change of the refractive index may influence both amplitude and phase of the electric field of the reflected/diffracted probe pulse while the displacement of the surface only changes the phase of the electric field of the reflected/diffracted probe pulse. The change of the refractive index due to the lattice temperature increase, $\Delta\widetilde{n}_T(x, y, t)$, can be expressed in a linear relationship as,

$$\Delta\widetilde{n}_T(x, y, t) = \left(\frac{\partial n}{\partial T} + i\frac{\partial \kappa}{\partial T}\right)\Delta T_l(x, y, t), \tag{2.8}$$

where $\partial n/\partial T$ and $\partial \kappa/\partial T$ are the real and imaginary parts of the thermo-optic coefficient, respectively, and ΔT_l is the lattice temperature increase.

Similarly, the change of the refractive index due to the strain-optic effect, $\Delta\widetilde{n}_s(x,y,t)$, can be expressed as,

$$\Delta\widetilde{n}_s(x,y,t) \quad = \quad \left(\frac{\partial n}{\partial s_x} + i\frac{\partial \kappa}{\partial s_x}\right) s_x(x,y,t). \tag{2.9}$$

where $\partial n/\partial s_x$ and $\partial \kappa/\partial s_x$ are the real and imaginary parts of the strain-optic coefficient respectively and s_x is the longitudinal strain. The two relations in Eq. 2.8 and Eq. 2.9, are valid when the probe pulse is incident normal to the surface and when the strain field doesn't have a large off-axis component ($s_y \approx 0$). If the probe pulse is not incident in a direction normal to the surface, or if the strain field has large off-axis components, the anisotropy of the sound-induced changes in the permittivity tensor should be taken into account. In that case, one has to solve Maxwell's equations in an anisotropic medium to obtain the diffracted/reflected field of the probe pulse. In our experiments, the probe pulse is incident on the surface at almost normal incidence, and the strain-optic effect due to acoustic diffraction is neglected. When the strain-optic and thermo-optic coefficients are known, the total change of the refractive index $\Delta\widetilde{n}(x,y,t) = \Delta\widetilde{n}_T(x,y,t) + \Delta\widetilde{n}_s(x,y,t)$ can be determined. Later, the complex electric field of the probe pulse at the surface, $\widetilde{E}_{p\Delta\widetilde{n}}$, is calculated for each time step using the transfer-matrix method [43].

According to the Fraunhofer diffraction theory, the two dimensional spatial Fourier transform of this electric field should give the far field diffraction pattern. However, we need to include the spatial modulation of this electric field due to the grating-shaped surface displacement from the spatially periodic acoustic wave. It is assumed that the surface displacement by the acoustic wave only introduces a local phase-shift to the electric field. Therefore the complex electric field that takes all the effects into account, $\widetilde{E}_p$, can be written as,

$$\widetilde{E}_p(y,t) = \widetilde{E}_{p\Delta\widetilde{n}}(y,t)e^{i\frac{4\pi n}{\lambda_p}u_{xs}(y,t)}, \tag{2.10}$$

where u_{xs} is the surface displacement as a function of y and $\widetilde{E}_{p\Delta\widetilde{n}}(y,t)$ is the earlier calculated complex electric field of the probe at the surface after accounting for the refractive index changes. The assumption that surface displacement only introduces a phase shift in the electric field is commonly

known as the shallow grating approximation. This is a valid approximation when the peak-to-valley amplitude of the displacement grating is much smaller than the wavelength of the probe pulse (800 nm). This is usually the case for laser-induced ultrasonics experiments where the surface and interface displacement amplitudes are less than a nanometer.

Once we know the complex electric field at the surface that includes any possibles refractive index modulations and possible displacement of the surface, we can take the 2D spatial Fourier transformation to obtain the diffracted electric fields in the far field. The optical intensity of the 1^{st} order diffracted field is then calculated.

In the next section we demonstrate mathematically that when a diffraction grating is translated along the grating vector direction, the $+1^{st}$ order and the -1^{st} order beams acquire opposite phase shifts.

2.3 Fraunhofer diffraction from a displaced grating

We use the Fraunhofer diffraction equation to describe the diffraction of optical fields when the diffraction pattern is viewed at a large distance from the diffracting object. This is the case when we have optical diffraction from a grating. The following is adapted from [44]. The electric field of U, at the far field from a aperture can be described as:

$$U(x,y,z) = \frac{e^{ikz}e^{i\frac{k}{2z}(x^2+y^2)}}{i\lambda z}\iint_{-\infty}^{\infty} U(\xi,\eta,z=0)e^{-i\frac{2\pi}{\lambda z}(x\xi+y\eta)}d\xi d\eta. \quad (2.11)$$

where ξ and η are the source coordinates and x, y, and z, are the coordinates where the field is calculated. Defining the spatial frequencies spatial frequencies as $f_x = x/(\lambda z)$ and $f_y = y/(\lambda z)$, we write Eq. 2.11 as,

$$U(x,y,z) = \frac{e^{ikz}e^{i\frac{k}{2z}(x^2+y^2)}}{i\lambda z}\iint_{-\infty}^{\infty} U(\xi,\eta,z=0)e^{-i2\pi(f_x\xi+f_y\eta)}d\xi d\eta. \quad (2.12)$$

The Eq. 2.12 shows that the diffraction field is related to the source field by a simple Fourier transform relationship. We now define a transmission function t_A which is the ratio of the complex field immediately behind a plane

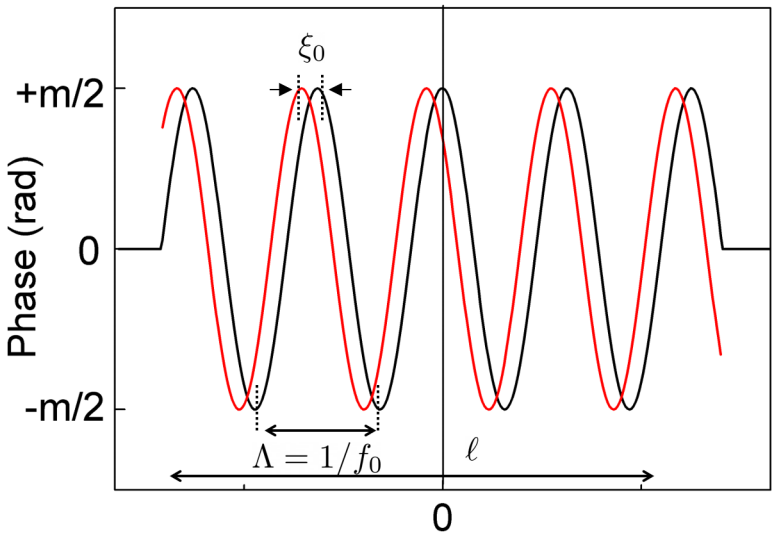

Figure 2.2: An example of a cosine phase grating with grating period Λ (spatial frequency $f_0 = 1/\Lambda$), amplitude $m/2$, and multiplied by a rect function, rect(ξ/ℓ) . The red curve is a grating with the same rect function, but with the phase grating shifted by $-\xi_0$.

to that of the field incident on the plane. If the incident field has amplitude 1 and is incident normally on the screen (so no phase variation across the aperture for the incident beam) then we can write: $t_A(\xi, \eta) = U(\xi, \eta, z = 0)$.

For this calculation we will assume that the grating is a thin cosine phase grating with dimensions in the x and y-direction of ℓ (Figure 2.2). Hence we can write the complex transmission function for this grating as,

$$t_A(\xi, \eta) = \exp\left[i\frac{m}{2}\cos(2\pi f_0(\xi + \xi_0))\right]\text{rect}\left(\frac{\xi}{\ell}\right)\text{rect}\left(\frac{\eta}{\ell}\right), \qquad (2.13)$$

where f_0 is the spatial frequency of the grating, $-\xi_0$ is the distance over which the grating has been displaced compared to the original position (ξ_0 =0) and m is the peak-to-valley variation of the phase.

The Fourier transform will give us the following expression,

$$\begin{aligned}\mathrm{FT}\left[t_A\left(\xi,\eta\right)\right] &= \sum_{q=-\infty}^{\infty}\iint_{-\infty}^{\infty}\ell^2\mathrm{sinc}\left[\ell(f_x-f_1)\right]\mathrm{sinc}\left[\ell(f_y-f_2)\right] \\ &\quad \exp\left(i2\pi f_1\xi_0\right)i^q J_q\left(\frac{m}{2}\right)\delta(f_1-qf_0,f_2)df_1df_2 \\ &= \sum_{q=-\infty}^{\infty} i^q J_q\left(\frac{m}{2}\right)\ell^2\mathrm{sinc}\left[\ell(f_x-qf_0)\right]\mathrm{sinc}\left[\ell f_y\right]\exp\left(i2\pi q f_0\xi_0\right).\end{aligned} \tag{2.14}$$

where, J_q is the Bessel function of the first kind and order q.

Since we are interested it the $+1^{\text{st}}$ and the -1^{st} order diffracted light, we use the value $q=1$ and $q=-1$ to get,

$$U_{q=1}(x,y,z) = \frac{e^{ikz}e^{i\frac{k}{2z}(x^2+y^2)}}{i\lambda z}J_1(\frac{m}{2})\ell^2\mathrm{sinc}[\ell(f_x-f_0)]\mathrm{sinc}[\ell f_y] \exp(2\pi f_0\xi_0+i\frac{\pi}{2}) \tag{2.15}$$

$$U_{q=-1}(x,y,z) = -\frac{e^{ikz}e^{i\frac{k}{2z}(x^2+y^2)}}{i\lambda z}J_{-1}(\frac{m}{2})\ell^2\mathrm{sinc}[\ell(f_x+f_0)]\mathrm{sinc}[\ell f_y] \exp(-i2\pi f_0\xi_0+i\frac{\pi}{2}). \tag{2.16}$$

As expected, the phase terms, $\exp\left(\pm i2\pi f_0\xi_0\right)$ are opposite in phase. Since $J_{-1}\left(\frac{m}{2}\right) = -J_1\left(\frac{m}{2}\right)$, we can write the above expression as,

$$U_{q=1}(x,y,z) = \frac{e^{ikz}e^{i\frac{k}{2z}(x^2+y^2)}}{i\lambda z}J_1(\frac{m}{2})\ell^2\mathrm{sinc}[\ell(f_x-f_0)]\mathrm{sinc}[\ell f_y] \exp(i2\pi f_0\xi_0+i\frac{\pi}{2}) \tag{2.17}$$

$$U_{q=-1}(x,y,z) = \frac{e^{ikz}e^{i\frac{k}{2z}(x^2+y^2)}}{i\lambda z} J_1(\frac{m}{2})\ell^2 \mathrm{sinc}[\ell(f_x+f_0)]\mathrm{sinc}[\ell f_y] \exp(-i2\pi f_0\xi_0 + i\frac{\pi}{2}). \tag{2.18}$$

From the above expression we can see that a translation of the grating along the direction parallel to the grating k vector (ξ_0) changes the phase of the -1^{st} and $+1^{\mathrm{st}}$ order diffracted fields in opposite direction. We can also see that the intensities of the -1^{st} and $+1^{\mathrm{st}}$ order diffracted fields remain the same after the translation.

For a non-displaced cosine grating ξ_0 =0, and the expressions for first-order diffracted electric fields are,

$$U_{q=1}(x,y,z)|_{\xi_0=0} = \frac{e^{ikz}e^{i\frac{k}{2z}(x^2+y^2)}}{i\lambda z} J_1(\frac{m}{2})\ell^2 \mathrm{sinc}[\ell(f_x-f_0)]\mathrm{sinc}[\ell f_y] \exp(i\frac{\pi}{2}) \tag{2.19}$$

$$U_{q=-1}(x,y,z)|_{\xi_0=0} = \frac{e^{ikz}e^{i\frac{k}{2z}(x^2+y^2)}}{i\lambda z} J_1(\frac{m}{2})\ell^2 \mathrm{sinc}[\ell(f_x+f_0)]\mathrm{sinc}[\ell f_y] \exp(i\frac{\pi}{2}) \tag{2.20}$$

Here the phases of the -1^{st} and $+1^{\mathrm{st}}$ order diffracted fields are the same, as expected.

2.4 Transient-grating pump-probe setup

Experiments described in this thesis aim to study the electron-lattice dynamics in metals and to generate grating-shaped acoustic waves in metals, were mostly performed using a transient-grating pump-probe setup. In a

transient-grating pump-probe setup, two pump pulses are crossed at an angle to create an optical interference pattern on the sample. The interference pattern, which has the shape of a grating with a spatial period Λ, excites the sample in a spatially periodic manner. The spatial modulation induced by the interference pattern can result in the diffraction of a delayed probe pulse.

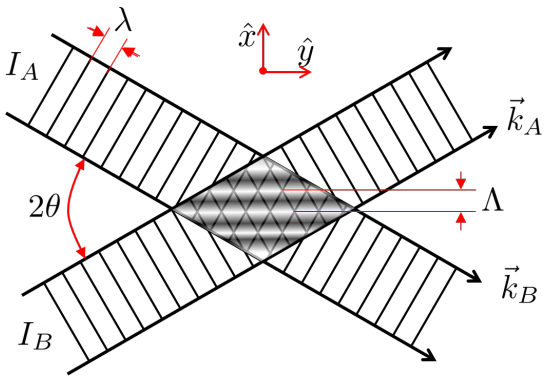

Figure 2.3: Transient-grating produced by two interfering beams with intensities I_A and I_B having wave vectors k_A and k_B respectively.

Here we show the derivation of the transient-grating period Λ, for two plane waves with a wavelength λ crossing at each other at an angle 2θ. A detailed theoretical description of two beam interference under various conditions can be found in here [45]. An experimental configuration for the generation of transient-gratings is shown in Figure 2.3. The output from the laser is split into two beams, denoted here as A and B. The electric field of beams A and B can be written as,

$$\vec{E}_A(\vec{r},t) = E_A \exp[i(\vec{k}_A \cdot \vec{r} - \omega t + \phi_A)]\hat{r} \tag{2.21}$$

and,

$$\vec{E}_B(\vec{r},t) = E_B \exp[i(\vec{k}_B \cdot \vec{r} - \omega t + \phi_B)]\hat{r}, \tag{2.22}$$

respectively, where $\hat{r} = \hat{x} + \hat{y}$. Here, $\vec{k_A}$ and $\vec{k_B}$ are wave-vectors, E_A and E_B are the electric field amplitudes, and ϕ_A and ϕ_B are the optical phases, of beam A and B, respectively. In the coordinate system we use, the wave

vectors can be written as,

$$\begin{aligned} \vec{k}_A &= k\cos\theta\hat{x} + k\sin\theta\hat{y} \\ \vec{k}_B &= k\cos\theta\hat{x} - k\sin\theta\hat{y}. \end{aligned} \tag{2.23}$$

where $k = 2\pi/\lambda$. The two fields interfere on the sample surface and the total electric field due to the interference can be written as,

$$\vec{E}(r,t) = E_A \exp\left[i(\vec{k}_A \cdot \vec{r} - \omega t + \phi_A)\right]\hat{r} + E_B \exp[i(\vec{k}_B \cdot \vec{r} - \omega t + \phi_B)]\hat{r} \tag{2.24}$$

The intensity $I(\vec{r},t)$ of the plane wave is given by the time average of the Poynting vector,

$$I(\vec{r},t) = <\vec{S}> = \frac{\epsilon c n}{2}|\vec{E}(\vec{r},t)|^2 \tag{2.25}$$

where c is the speed of light in vacuum, ϵ is the vacuum permittivity and n is the refractive index of the medium. Since,

$$|\vec{E}(\vec{r},t)|^2 = E_A^2 + E_B^2 + 2E_A E_B \cos(\vec{K}.\vec{r} + \phi_1 - \phi_2) \tag{2.26}$$

where the grating vector $\vec{K}$ is given by,

$$\vec{K} = \pm(\vec{k}_A - \vec{k}_B) = \pm 2k\sin\theta\hat{y}, \tag{2.27}$$

we can write the intensity along the x-axis due to the interfering plane waves as,

$$I = \frac{\epsilon c n}{2}(E_A^2 + E_B^2 + 2E_A E_B \cos(2k\sin\theta + \phi_1 - \phi_2)). \tag{2.28}$$

When the phase difference between the two beams is set to zero: $\phi_A = \phi_B$, the intensity of the interference pattern can be written as,

$$I = I_A + I_B + \frac{\epsilon c n}{2} 2E_A E_B \cos(2k\sin\theta), \tag{2.29}$$

where I_A and I_B are the intensities of the beams A and B respectively. The spatial modulation of the intensity is due to the cosine term in Eq. 2.29 and therefore, the spatial period of the transient grating is then given by,

$$\Lambda = \frac{\lambda}{2\sin\theta} \tag{2.30}$$

where, λ is the pump wavelength and 2θ is the angle between the beams. Here it can be seen that the pitch of the grating can be varied by changing the angle between the beams. The smallest grating pitch that can be achieved is $\lambda/2$ when the angle between the beams is π, and the largest grating pitch that can be achieved is limited by the diameter of the laser beams. In our transient-grating setup, the angle between the beams is such that $\sin\theta = 1/30$, and $\lambda = 400$ nm; therefore, we have a grating period of 6 µm.

3 Experimental details

3.1 Laser system

Most of the pump-probe measurements discussed in this thesis were performed using a Ti:Sapphire amplifier (Femtopower, Spectra-Physics). It is a 1 kHz-repetition rate, multi-pass amplifier seeded with broadband, ultrashort pulses of about 10 fs pulse duration at a repetition rate of approximately 79 MHz from a dispersion controlled oscillator. A functional block diagram of the laser system is shown in Figure 3.1. The pulses from the oscillator are stretched by propagation through thick layers of glass prior to amplification to avoid damaging the Ti:Sapphire crystal inside the amplifier. The pulses are then amplified by multiple passes through the crystal, pumped by a 22 W diode-pumped Nd:YLF laser operating at a wavelength of 527 nm and a repetition rate of 1 kHz. After the four passes, a single pulse is selected from the MHz-pulse train with two Pockel's cells. This pulse is sent through Fastlite's DAZZLER, an acousto-optic programmable filter that is used to pre-compensate third- and fourth-order dispersion (i.e. optimize the re-compressed pulse-width). The DAZZLER also spectrally shapes the optical pulse in order to reduce the effect of gain-narrowing in the amplifier. Further amplification of this pulse to 4 mJ is achieved by

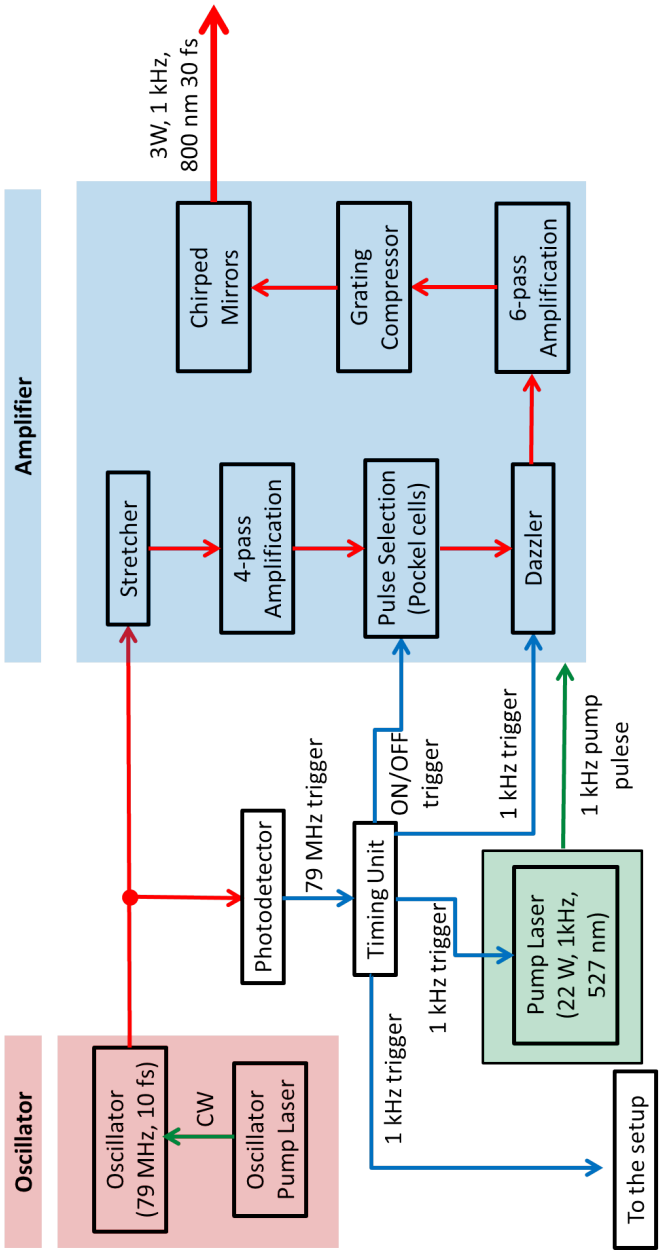

Figure 3.1: Functional block diagram of the laser system.

six further passes through the Ti:Sapphire crystal. After the 10^{th} pass, the pulse is picked off and sent to a grating compressor followed by a set of chirped mirrors for pulse compression. Finally, the average output power from the amplifier is 3 W at 1 kHz repetition rate, and pulses have a duration of 30 fs with a wavelength centered around 800 nm.

3.2 Pump-probe setup

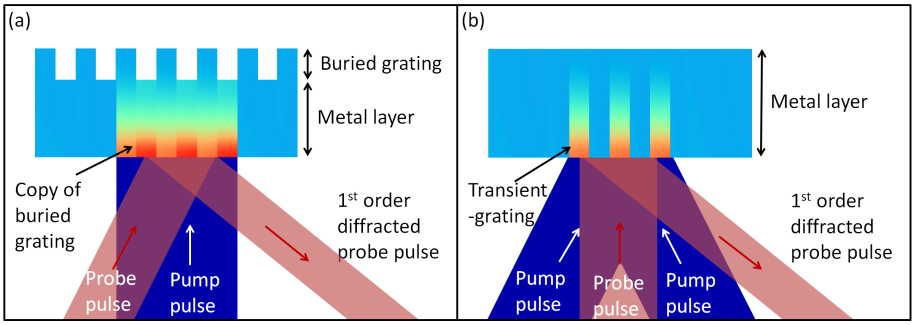

Figure 3.2: Two configurations of pump-probe setup: (a) single pump pulse excites the sample, and the probe pulse diffracted from the "copy" of the buried grating is measured as a function of pump-probe delay. (b) two pump pulses interfere to form a grating, and the diffracted probe pulse is measured as a function of time.

All of the experiments discussed in the thesis were performed using various configurations of a pump-probe setup. Pump-probe setups are usually employed to study extremely fast processes occurring in the physical, chemical, and biological research fields. In our pump-probe setups, a beamsplitter splits a laser pulse into a 'pump' pulse and a 'probe' pulse. Both of the two pulses arrive at the sample via different paths, and the optical path difference between the pulses is varied to create a temporal delay between the pump and the probe. This is done by reflecting light off two mirrors in a retro-reflecting geometry mounted on a mechanical delay line. The pump pulse excites the sample and can change the physical properties of the sample, while the delayed probe pulse detects these changes. In our experiments, we mainly use two schemes of a pump-probe setup. In the first scheme shown in Figure 3.2 (a), a single pump pulse excites a flat metal layer with an optically buried grating. The shape of the buried grating is transferred to the surface of the metal layer in the form of a spatially

periodic surface displacement or a spatially periodic change of the complex refractive index. The delayed probe pulse diffracts from this "copy" of the buried grating, and the first-order diffracted signal is recorded. Various physical mechanisms responsible for creating the "copy" of the buried grating are discussed in Chapter 3, 6 and 7. In the second scheme shown in Figure 3.2 (b), two pump pulses overlap spatially and temporally to form an interference pattern that excites the sample in a grating-like pattern. The probe pulse diffracts due to the change in the optical constants of the sample or by a spatially periodic displacement of the surface induced by the periodic excitation (details can be found in Chapter 4 and 5). In laser-induced ultrasonics experiments, the diffraction can also be due to the spatial periodic displacement of the surface. In both the schemes, we measured the intensity of the diffracted probe pulse with a silicon photodetector. The photodetector generates a voltage proportional to the intensity of the light recorded by the photodiode. Fluctuations in the output energy of the laser pulses are accounted for by dividing the measured diffracted signal by a reference signal obtained by a silicon photodetector that monitors pulse-to-pulse variations in the output energy. The signals are sent to a boxcar integrator, which integrates the electronic signals. The analog signals from the boxcar integrator are converted to a digital signals using an analog-to-digital converter. The data acquisition card triggered by the laser pulses reads out the voltages and also records the position of the mechanical delay line. The home-built software can vary the pump-probe delay in small steps (down to 1 fs) and simultaneously records the reference signal and the diffracted signal. The software can average the signal over a number of optical pulses for a given time delay.

3.3 Determining the pump-probe temporal overlap

3.3.1 Sum-frequency generation

Before using the transient-grating pump-probe setup for experiments, we have to determine the exact position of the mechanical delay stage, for which the pump and probe pulses overlap temporally on the sample. For this purpose, a type 1 beta barium borate (BBO) crystal was placed at the

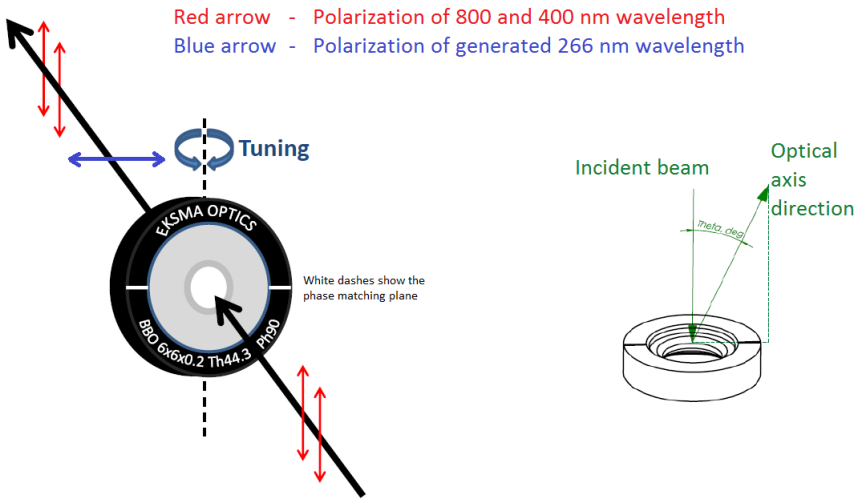

Figure 3.3: The crystal orientation and polarization of the 400 nm and 800 nm wavelength beams used to generate 266 nm wavelength beam.

location of the sample where we want the pump and probe pulses to overlap. When the 400 nm wavelength pump pulse and the 800 nm wavelength probe pulse overlap both spatially and temporally inside the BBO, we expect 266 nm light to be created as a result of sum-frequency generation inside the BBO crystal. The BBO used here was 200 µm thick and 6 mm × 6 mm in area and the crystal orientation was $\theta = 44.3^0$ and $\phi = 90^0$ so that, the crystal can generate a 266 nm wavelength beam when a 400 nm and 800 nm wavelength beams are incident perpendicular to the surface of the BBO crystal. The crystal orientation and polarization of the 400 nm and 800 nm wavelength beams with respect to the BBO crystal, are shown in Figure 3.3. We focus the 400 nm wavelength pump beam and the 800 nm wavelength probe beam into the BBO in a non-collinear geometry such that both beams overlap spatially inside the crystal. The angle between the beams was 2.5^0. The 400 nm and 800 nm wavelength light and the generated 266 nm wavelength light is transmitted through the crystal. We placed a SiC detector that measures the intensity of the 266 nm beam at the location where we expect the 266 nm beam. Spatially, the 266 nm wavelength beam is expected to be generated in between the 400 nm and

800 nm wavelength beams but not exactly in the middle. In the detection plane, if the distance between the 400 nm beam and the 800 nm beam is x, then the 266 nm wavelength beam will be positioned at roughly x/3 from the 400 nm beam. This is a direct consequence of the momentum conservation between the 800 nm, 400 nm and 266 nm photons.

To determine the temporal overlap, the delay between the 400 nm pump pulse and the 800 nm probe pulse is varied while observing the presence and intensity variation of the generated 266 nm light. When the pulses are not overlapping, we don't expect any 266 nm wavelength light to be generated. As the pump and probe pulse begin to overlap in time, the intensity of the 266 nm wavelength light increases. The pump-probe delay time for which the highest intensity is recorded is when the pump and probe perfectly overlap in time. Although the 266 nm wavelength is invisible to the human eye, we can detect the generation of this UV light by placing a white paper where we expect the beam. When the 266 nm wavelength light falls on a white paper, we can see a violet-colored spot due to the fluorescence of the white paper. For experiments that use two pump pulses, the same procedure described above is repeated with the second 400 nm pulse and the 800 nm pulse. The delay between the two 400 nm pulses is adjusted until all three pulses overlap spatially and temporally.

3.3.2 Transient grating in BBO

Now that we know the spatial and temporal position where the two pump pulses and the probe pulse overlaps, we can perform transient-grating pump-probe experiments. To align the location of the detector such that it measures the first-order diffracted probe pulse, we performed the first set of transient-grating experiments on the BBO crystal that was used to find the temporal overlap of the pulses. When two pump pulses overlap on the BBO crystal, a spatially periodic intensity pattern with a grating pitch of 6 µm is created. The intensity of the 400 nm wavelength pump pulses was increased in order to induce spatially periodic changes in the refractive index of the BBO, which arise from nonlinear optical effects in the crystal. The 800 nm wavelength probe pulse then diffracts from the refractive index grating, and the first-order diffracted beam can be recorded by the detector. This experiment can be performed either in transmission or in

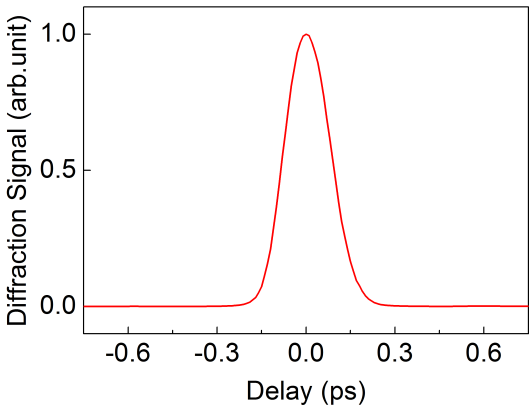

Figure 3.4: Diffracted signal from the BBO crystal as a function of pump-probe delay.

reflection. As our experiments on metal layers are done in reflection, we positioned the detector to capture the diffracted light in reflection geometry. In Figure 3.4, we plot the measured diffraction signal from the BBO crystal as a function of the pump-probe delay. We observe a symmetric curve centered around a delay time of 0 fs, with a full width at half maximum (FWHM) of approximately 160 fs. The probe pulse diffracts only when the pump pulses overlap spatially and temporally inside the sample. This is because the formation of a refractive index grating in the BBO is due to non-resonant nonlinear optical effects, which are practically instantaneous. The FWHM is larger than the original pulse duration most likely because of dispersion inside the BBO crystal and other transmissive optics.

3.4 Sample preparation

The metal layers of the samples used in the measurements were fabricated by various physical vapor deposition (PVD) techniques, such as thermal evaporation, electron beam evaporation, and sputter deposition. All of the samples were fabricated at the Amsterdam Nanocenter at AMOLF.

The Au layers were mostly deposited using a thermal evaporator called “Nanoontje”. The evaporator uses a resistive heat source to evaporate the metal in a vacuum environment. The evaporated metal forms a thin film

on the substrate placed above the heat source. The Au and Cu layers in the samples with buried gratings, discussed in Chapter 4, were fabricated using the same evaporator. The SiO_x layer in samples discussed in Chapter 5 were also fabricated using this evaporator.

The W and Ni layers on the samples discussed in Chapter 5 were deposited using an electron beam evaporator called "Kameleon". Instead of using a resistive heat source, in electron beam deposition, the target metal is bombarded with an electron beam from a charged tungsten filament to melt and evaporate the metal. The evaporated metal forms a thin film on the substrate placed above the metal target. This evaporation technique is better suited for metals having a high melting point. The bilayer metal samples discussed in Chapter 4, which contain both Au and Pt layers, were deposited using this evaporator. The Ni layers in samples discussed in Chapter 7 were deposited using another electron beam evaporator called "E-flex".

The SiO_2 and Si_3N_4 layers in the samples discussed in Chapter 6 were deposited using reactive sputter deposition. In sputter deposition, the material 'target' is subjected to an argon (Ar) gas plasma in a relatively low vacuum (10^{-2} mbar). The energetic Ar ions from the Ar plasma bombard the target material and remove (sputter) atoms from the material. The removed atoms are then deposited onto the substrate to form a uniform thin film. In reactive sputtering deposition, the ejected material undergoes a chemical reaction before reaching the substrate. This is done by introducing a reactive gas in the deposition chamber. For the deposition of SiO_2, a Si target is sputtered in the presence of oxygen gas (O_2) and for deposition of Si_3N_4, a Si target is sputtered in the presence of nitrogen gas (N_2). The composition of the material can be adjusted by varying the ratio between the Ar gas and the reactive gas (O_2 or N_2).The parameters used during the deposition of 18 nm SiO_2 and 18 nm Si_3N_4 are shown in Table 3.1.

The gratings on the metal layer of the samples discussed in Chapter 6 and 7 were fabricated by UV lithography. The resist, S1805, was spin-coated on the metal layer for approximately 45 seconds at 2000 rpm. The resist-coated sample was then exposed with UV light through the mask containing the grating pattern for 2-3 seconds using a commercial UV mask aligner,

	SiO_2	Si_3N_4
Base pressure (mbar)	7.6×10^{-3}	1×10^{-2}
Argon flow rate (sccm)	7.16	3.5
Oxygen flow rate (sccm)	7.16	0
Nitrogen flow rate (sccm)	0	20
RF Power (W)	150	143
Time (s)	700	1700

Table 3.1: Parameters for the deposition of 18 nm SiO_2 and Si_3N_4 using reactive sputter deposition.

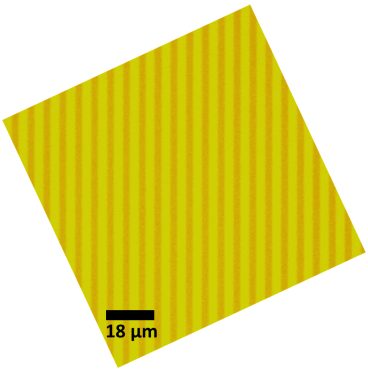

Figure 3.5: Optical microscope image of a 6 µm pitch, 50% duty cycle grating fabricated on a flat gold layer.

"Suss MA6". The exposure wavelength is 385 nm, and the system operated at 25 mW of optical power. The resist is then developed in the developer solution, Ma-D 533-S, for approximately 30 seconds. Another layer of metal is deposited on top of the patterned resist layer, and the remaining resist layer is removed by immersing the whole sample in a "lift-of" solution. The optical microscope image of a grating on a Au layer fabricated with this recipe is shown in Figure 3.5. The grating shown here has a pitch of 6 µm, and a duty cycle of approximately 50%.

4

Detection of gratings through opaque metal layers by optical measurements of ultrafast electron dynamics

The first step in the generation of extremely-high frequency acoustic waves is the absorption of the light by the free-electron gas. The subsequent thermalization and cooling of the electron gas together with the electron energy diffusion, are essential ingredients to determine where the absorbed energy is transformed into lattice heat. This determines the extent and shape of the generated acoustic wave. In this chapter, we show measurements and calculations of electron dynamics in single metallic layers and in metallic bilayers upon excitation with a femtosecond laser pulse. We show that the electron dynamics is strongly influenced by the thickness of the metal and by the strength of the electron-phonon coupling constant. These effects can be used to determine the presence and nature of a metal layer (grating) buried below another metal layer.

This chapter has been published as Opt. Express **26**, 23380–23396 (2018) [46].

4.1 Introduction

When a femtosecond pulse is absorbed by the metal within the optical skin depth, a non-thermal distribution of excited electrons is created. These electrons undergo ballistic and diffusive motion and thermalize to a Fermi-Dirac distribution, due to electron-electron scattering, on a time scale of up to hundreds of femtoseconds [40, 47–50]. An acoustic wave is generated as the thermalized electron gas cools by heating up the lattice, a process that typically takes a few picoseconds. Therefore it is essential to study the electron-lattice dynamics just after the optical excitation for a better understanding of the acoustic wave generation in metals.

The interaction of femtosecond laser pulses with metals has been an area of active research in photochemistry [51, 52], laser ablation [53], and in the generation of coherent terahertz pulses from the surface of metals [54–57]. Numerous studies have led to an improved understanding of the fundamental processes involved when a femtosecond laser pulse irradiates metal layers of nanometer-scale thickness [21, 22, 24, 58–73].

Surprisingly, although electron dynamics following ultrafast optical excitation in single metal layers of nanometer-scale thickness is fairly well understood, only a few experimental studies of metallic *bilayers* have been published. The presence of one type of metal below a layer made of a different metal is not only expected to affect the electron dynamics in the top layer [67–69, 74–76], but also the location inside the bilayer system where lattice heating occurs [77, 78]. This is obviously highly relevant for ablation experiments, but, interestingly enough, they also hint at the possibility to use these effects to detect and, possibly, image buried metal layers and buried micro-and nano-structures [79].

In this chapter, we show that gold and copper gratings, buried below an optically opaque, flat gold layer, can be detected at the surface of the gold by observing transient optical diffraction. The transient diffraction is the result of an electron temperature grating that forms after exciting the flat gold layer with a single femtosecond laser pulse. This temperature grating is the result of the different electron dynamics above the valleys and the trenches of the real, buried grating and leads to a grating in the optical

constants near the surface of the gold from which a probe pulse can be diffracted. Time resolved diffraction measurements on *flat* metallic bilayers, in which two overlapping and interfering pump pulses form a spatially periodic, grating-like excitation pattern, confirm that electron dynamics is a sensitive probe of the type and thickness of the buried metal underneath the opaque gold layer. They hint at the possibility to use these effects for optical detection and alignment applications.

4.2 Experimental setup

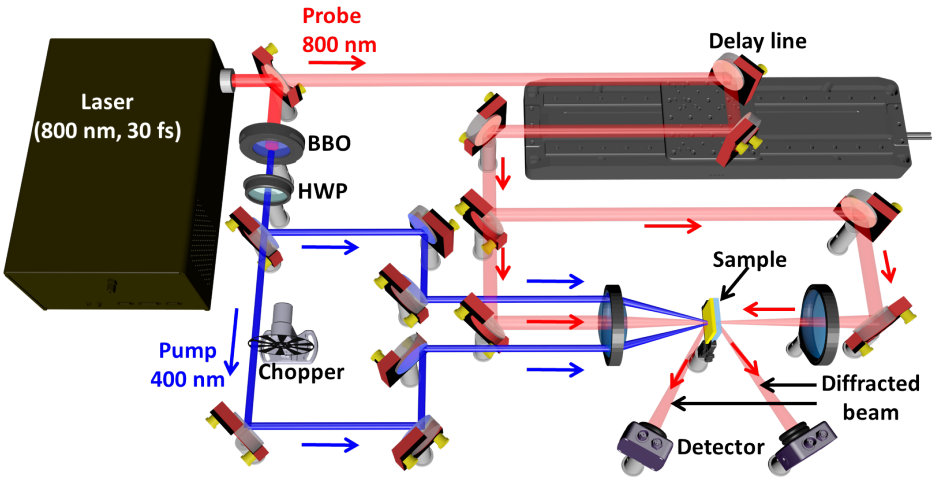

Figure 4.1: Schematic of the experimental setup: components include a non-linear optical crystal (BBO), Half Wave Plate (HWP) and photodiodes. The two frequency-doubled 400 nm pump pulses are focused onto the sample at the same position, but under different angles to form a spatially periodic intensity pattern. The 800 nm probe pulse that diffracts off the resulting grating in the optical constants of the sample, is recorded by the detectors while the delay line is used to change the pump-probe delay.

A schematic of the experimental setup used for our experiments is shown in Figure 4.1. The laser system used is a Ti:Sapphire multi-pass amplifier (Femtopower, Spectra Physics) generating 30 fs pulses, with a wavelength centered at 800 nm and with a repetition rate of 1 kHz. The output from the laser is split into two using a 1% beam splitter. The stronger part is frequency doubled with a 100 µm BBO crystal to generate 400 nm pump pulses. A half wave plate (HWP) rotates the polarization of the 400 nm

pump pulse by 90^o so that both the pump and the probe are p-polarized. For experiments on flat samples, the pump pulses are split into two by a 50% beamsplitter. One part passes through a 500 Hz mechanical chopper. Both beams are then weakly focused onto the sample at a different angle. On the sample, the two pump pulses overlap in space and time to create a spatially periodic interference pattern with a period determined by the angle between the beams. In our experiments, we have a grating period of about 6 µm. The spatially periodic excitation of the metal leads to spatially periodic changes in the optical constants of the metal, that can be observed by diffracting a delayed probe pulse off the transient grating. By measuring the diffracted signal as a function of the pump-probe delay, we can measure the decay of this transient grating, giving information on the electron dynamics. Using different, fixed wavelengths for pump and probe allows us to use optical filters to block scattered pump light from entering the probe detector. The diffracted pulse energy is recorded by a silicon photodiode placed at the position where we expect the first-order diffracted beam. The analog signal recorded from the photodiode is converted to a digital signal and averaged over 100 pulses. The diffracted probe signal recorded by the detector when the chopper blocks the pump beam is subtracted from the diffracted probe signal when the pump beam is transmitted by the chopper and plotted as a function of the pump-probe delay. The signal recorded by the detector in the absence of the pump pulse is from probe light scattered by the surface roughness of the sample. Depending on the experiment, we probe from the front surface or from the back surface. In the latter case, the probe pulse passes through the glass substrate and probes the metal near the glass-metal interface. The pump beam has a spot size of 1.5 mm on the sample and the pump pulse energy ranges from 3 µJ to 15 µJ depending on the experiment. The probe pulse energy was kept constant at 1 µJ . This is a significant fraction of the pump-pulse energy to maximize the possibility of detecting signals on samples demonstrating a low diffraction efficiency. However, in our experiments we mostly pump and probe Au in which about 60% of the 400 nm wavelength pump-pulse energy is absorbed and only about 2% of the 800 nm wavelength probe-pulse energy. The typical diffraction efficiencies, recorded when the pump and probe overlap, range from 10^{-5} to 10^{-4}, depending on the pump pulse energy and the sample thickness. For the

experiments on the physically buried metal grating, only *one* pump beam is used.

All samples used in the experiments are prepared by physical vapor deposition at a pressure below 10^{-6} mbar on a chemically cleaned glass substrate. The film thickness was determined using a quartz crystal thickness monitor with a $\pm$ 5% uncertainty. For experiments on bilayer thin films, the materials were evaporated one after the other without disturbing the vacuum of the evaporator. The metal gratings on the flat layer of gold were fabricated by UV lithography.

4.3 Numerical calculations

4.3.1 Laser pulse absorption calculation

For a proper understanding of our experiments on flat bilayer samples and buried grating samples, it is important to calculate where the optical energy is deposited inside the material. To calculate the absorption of the light inside the metal layers, we solve Maxwell's equations with the appropriate boundary conditions. This calculation is important in the case of bilayer samples, because the incident laser pulse can directly excite the electrons in the second metal layer. To include the absorption of light in the second layer, we solve Maxwell's equations for a system of four materials as illustrated in Figure 4.2. This resembles the experiment in which, air, the first metal, the second metal and the substrate are the four different materials through which the laser pulse propagates. Material 1 and 4 are infinitely thick while materials 2 and 3 have a finite thickness. The first material represents air and material 4 represents glass. Material 2 and material 3 are the Au and Pt metal (or other metals used in the experiment) layers respectively. From the basic electromagnetic equations, we can understand that a wave incident on the interface between material 1 and material 2 will undergo partial reflection into the first material and partial transmission into the second material. The partially transmitted wave undergoes further partial reflection and transmission at the interface between material 2 and 3 and, material 3 and 4 . To calculate the spatial distribution of absorption in material 2 and material 3, we need to obtain the complete electric and

magnetic field expressions describing the magnitude and direction of the fields. We assume that all fields propagate perpendicular to the interfaces.

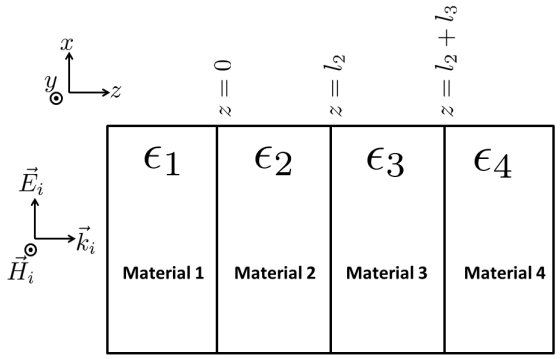

Figure 4.2: Geometry used for the calculation: Material 1 and 4 have an infinite extent to the left and right side respectively. Material 2 and 3 have a finite thickness of l_2 and l_3 respectively. The electromagnetic wave originating from material 1 propagates through all four materials after undergoing partial reflection and transmission at each interface.

Due to the non-magnetic nature of gold and platinum we can safely assume $\mu = \mu_0$ for all materials. In absence of any charged particles or currents, we can write the electric and magnetic fields inside each material as

$$\vec{E}(z,t) = E_0(t) \begin{cases} (e^{ik_1 z} + re^{-ik_1 z})\hat{x}, & z < 0 \\ (ae^{ik_2 z} + be^{-ik_2 z})\hat{x}, & 0 < z < l_2 \\ (ce^{ik_3(z-l_2)} + de^{-ik_3(z-l_2)})\hat{x}, & l_2 < z < (l_2 + l_3) \\ t(e^{ik_4(z-(l_2+l_3))})\hat{x}, & z > (l_2 + l_3) \end{cases} \tag{4.1}$$

$$\vec{H}(z,t) = \frac{E_0(t)}{\omega\mu} \begin{cases} k_1(e^{ik_1 z} - re^{-ik_1 z})\hat{y}, & z < 0 \\ k_2(ae^{ik_2 z} - be^{-ik_2 z})\hat{y}, & 0 < z < l_2 \\ k_3(ce^{ik_3(z-l_2)} - de^{-ik_3(z-l_2)})\hat{y}, & l_2 < z < (l_2 + l_3) \\ k_4(te^{ik_4(z-(l_2+l_3))})\hat{y}, & z > (l_2 + l_3) \end{cases} \tag{4.2}$$

where *a, b, c, d, t, r,* k_1 and k_4 are assumed to be real and $k_2 =$ and k_3 are

complex. Here $k_2 = \omega\widetilde{n}_2/c$ and $k_3 = \omega\widetilde{n}_3/c$ with $\widetilde{n}_{2,3} = n_{2,3} + i\kappa_{2,3}$ being the complex refractive index of material 2 and 3 respectively. The pulsed excitation is incorporated by our choice of electric field,

$$E_0(t) = Ae^{-4ln2(t/\tau_p)^2)} \times e^{(-i\omega t)},$$

where τ_p is the full width at half maximum pulse duration of the electric field envelope and A is the amplitude of the electric field.

We use the boundary condition that both the electric and magnetic field components parallel to the interface are continuous across each interface and solve the resulting set of equations to obtain expressions for *a, b, c, d, t* and *r*. This allows us to write the expression for the space and time-dependent fields in all four materials. From these we calculate the single oscillation time average of the Poynting vector, $\langle\vec{S}\rangle$. From $\langle\vec{S}\rangle$, the optical power absorbed per unit volume is expressed as,

$$\frac{\partial u}{\partial t} = -\vec{\nabla} \cdot \langle\vec{S}\rangle, \tag{4.3}$$

where u is the electromagnetic energy density. We use the refractive index n and extinction coefficient κ values of Au and Pt to calculate the optical intensity distribution and absorption inside the Au-Pt bilayer [77]. The result is the source term in the two-temperature model.

4.3.2 Two temperature model

To gain some insight into the physical processes taking place during and after optical excitation, we also performed calculations of the electron and lattice temperatures using the two-temperature model (TTM). For the calculations shown in this chapter, we numerically solve the TTM in 1 D. In the model, the electron gas is assumed to be thermalized at all times during and after excitation with, and is described by a time-dependent temperature T_e, while the lattice is assumed to have a time-dependent temperature T_l. The time evolution of the temperature is modeled by two coupled differential equations, originally proposed by Anisimov et al. [19] and can, assuming a one-dimensional geometry, be written as [21],

$$C_e(T_e)\frac{\partial T_e}{\partial t} = \frac{\partial}{\partial z}\left(K_e\frac{\partial}{\partial z}T_e\right) - g(T_e - T_l) + \frac{\partial u}{\partial t} \tag{4.4}$$

$$C_l\frac{\partial T_l}{\partial t} = g(T_e - T_l). \tag{4.5}$$

Here, C_e and C_l are the respective heat capacities of the electron gas and the lattice, K_e is the thermal conductivity of the electron gas, g is the electron-phonon coupling constant and $\partial u/\partial t$ is the source term. The source term describes when and where energy is deposited in the system by the laser pulse. Note that in Eq. 4.5, we left out a term for lattice heat diffusion since this is typically slow on the time scales of our experiment. We use the relations $C_e = A_e T_e$ and $K_e = K_0 \times T_e/T_l$ [21] and solve the TTM numerically to calculate the time evolution of T_e and T_l, using the actual experimental parameters and using material properties obtained from literature and shown in Table 4.1. By assuming instantaneous local thermalization of the electron gas we ignore ballistic transport of the electrons which is known to occur in gold in the first $\approx$ 100 fs [61].

As we will show in the following sections, we find a remarkable correspondence between the measured, time-dependent, diffracted signal, and the calculated time-dependent electron temperature. There is no a priori reason to assume that the diffraction efficiency η should linearly depend on the change in the electron temperature ΔT_e. It can be shown that the diffraction efficiency η scales as $\eta \propto (\Delta\epsilon)^2$, with $\Delta\epsilon$ being the change in the complex dielectric function [45]. If we assuming that changes in the dielectric function are dominated by changes in the electron gas temperature ΔT_e, we conclude that this linear relation must imply $\Delta\epsilon \propto \sqrt{\Delta T_e}$. This is different from the often made assumption that $\Delta\epsilon \propto \Delta T_e$ [50, 69, 73] or $\Delta\epsilon \propto \Delta(T_e)^2$ [70, 80]. We currently do not know what the origin is of the different temperature dependencies of the dielectric function extracted from the experiments. A full theoretical analysis of the time-dependent complex dielectric function after optical excitation requires detailed calculations of the contribution of inter- and intraband transitions to the changes in the complex dielectric function. Hohlfeld et. al. [62] showed that this can give satisfactory results, but such an effort is beyond the scope of this chapter. Here, we focus on the ability to use electron dynamics to detect gratings,

buried below an opaque metal. It is interesting, though, that our calculations of the electron temperature use only material parameters known from the literature. Only the electron-phonon coupling constant of gold that we use is on the low side of the range of values found in the literature. There are no adjustable parameters in our model as excitation parameters are taken from the experimental values. We have placed calculations of the time-dependent electron temperature alongside some of the measurements as they provide important physical insight into the electron and lattice dynamics occurring after excitation.

Table 4.1: Material constants used in our two temperature model calculations. Listed are the electron-phonon coupling constant g, electron specific heat constant A_e, thermal conductivity K_0 at $T = 273$ K and lattice heat capacity C_l. [21,64,81–85]. We have used the relations $C_e = A_e T_e$ and $K_e = K_0 \times T_e/T_l$ [21].

Metals	g (10^{16} $\mathrm{Wm^{-3}K^{-1}}$)	A_e ($\mathrm{Jm^{-3}K^{-2}}$)	K_0 ($\mathrm{Wm^{-1}K^{-1}}$)	C_l (10^5 $\mathrm{Jm^{-3}K^{-1}}$)
Gold	1.6-2.6	71	318	24.3
Platinum	100	740	73	27.0
Copper	8.0	98	401	35.0
Silver	1.9	63	428	25.0

4.4 Results and Discussion

Prior to our experiments on buried gratings, we performed pump-probe experiments with interfering pump pulses forming a spatially periodic, grating-like excitation pattern, on single layers of gold and gold-metal bilayers. These co-called transient-grating experiments were performed to obtain a better understanding of the electron dynamics and, in a few cases, to compare with results known from literature.

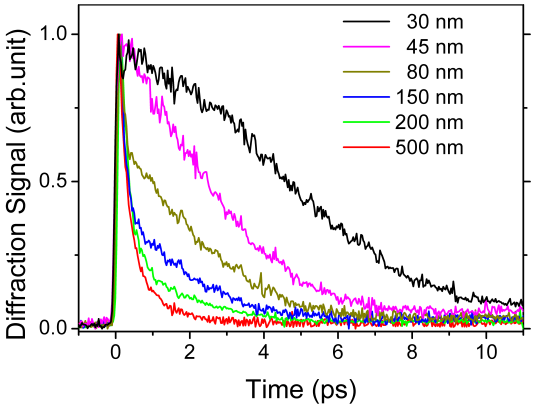

Figure 4.3: Diffracted front-probe signal vs. pump-probe delay for different gold thicknesses at a pump fluence of 0.8 mJ/cm^2.

4.4.1 Dependence of electron dynamics on Au layer thickness

To study how the electron dynamics is affected by the thickness of a metal layer, we performed transient-grating pump-probe measurement on Au layers having different thicknesses. In Figure 4.3, the normalized first-order diffracted signal is plotted as a function of pump-probe delay for 30, 45, 80, 150, 200 and 500 nm thick gold layers. At delay zero, when pump and probe pulses overlap in time, the diffraction efficiency rises to its maximum value within less than 100 fs. For gold layers thicker than about 100 nm, this is followed by a rapid decrease of the diffraction efficiency to zero within a few ps. In contrast, for thin gold layers, the decrease of the diffraction efficiency proceeds at a much slower pace taking up to 10 ps for the 30 nm sample. For thin layers, after 0.5 ps, the diffraction efficiency appears to decay linearly with delay for a few picoseconds. The results are similar to those obtained by Hohlfeld et al. who measured the transient reflectivity of gold layers [61] after illumination with 400 nm pulses, although there are some subtle differences between their results and ours. Most notably, the fast and sharp peak around delay zero with a width of about 0.5 ps, visible in our measurements in all but the 30 and 45 nm thick samples, is absent in the Hohlfeld paper. We think that this is due to the relatively

long pulses of 200 fs used in their experiments, as this would partially smear out rapidly changing signals. The initial fast decay observed for the thicker gold layers is caused by rapid electron energy diffusion out of the tens of nanometers thick surface layer probed by the 800 nm probe pulse. For thin layers, the electron energy becomes relatively homogeneously distributed over the entire thickness of the metal layer almost immediately, such that net spatial diffusion of energy out of the probe optical interaction region near the surface becomes negligible. The diffraction signal decay is then dominated by cooling of the electron gas by transfer of electron energy to the lattice, a process that is relatively slow for Au [61].

In Figure 4.4, we plot the probe signal diffracted from both the air-Au interface (front probe) and the glass-Au interface (back probe), for two different thicknesses of Au, 45 nm in Figure 4.4 (c) and 100 nm in Figure 4.4 (d), for various pump powers. Additional measurements of the front probe diffraction efficiency as a function of time, for various thicknesses of gold are similar to those shown by others [61]. In all cases, the 400 nm pump beams illuminate the Au from the front-side. As it is difficult to compare the absolute diffraction efficiencies for the front and back-probe cases, we applied a scaling factor to the back-probe signal such, that for a single pump intensity, both the front-probe signal and the back-probe signal overlap as much as possible for time delays larger than 0.5 ps. We then use the *same* scaling factor for the curves at different intensities. Different scaling factors were used for the 45 nm Au and 100 nm Au back probe signals and the signal strengths shown in Figure 4.4 (c) cannot be compared with those in Figure 4.4 (d). In both figures, the front probe diffraction efficiency is seen to rise on a rapid time scale of $\approx$ 100 fs. For the 45 nm sample in Figure 4.4 (c), this then gradually decays towards zero for increasing time delays. For the 100 nm sample in Figure 4.4 (d), the decay is initially rapid, and then slows down. In both measurements, excitation with two spatially and temporally overlapping pump pulses results in a spatially periodic electron gas temperature $T_e(x,t)$ along the surface, in a direction perpendicular to the grating lines. This temperature grating is formed when in the bright fringes of the interference pattern the electron gas is rapidly heated whereas in the dark fringes, where the electron gas is not excited, the temperature remains 297 K. The amplitude of this electron-gas temperature grating,

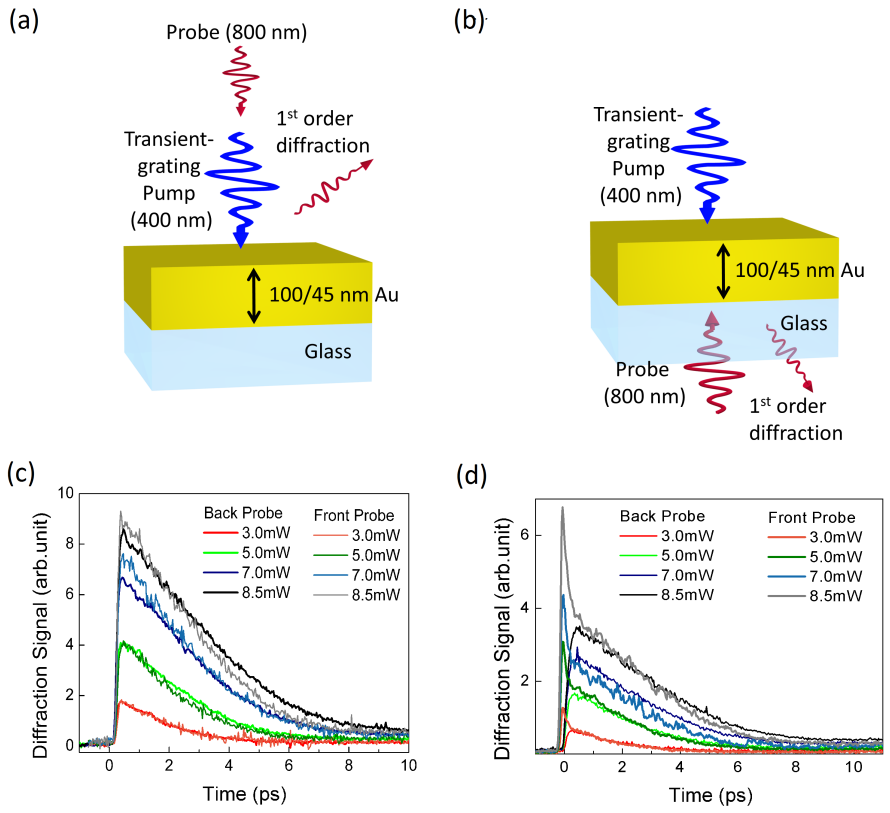

Figure 4.4: (a) Schematic showing the pump and front-probe: the samples were pumped from the air-Au side and probed from the air-Au side. (b) Schematic showing the pump and back-probe: the samples were pumped from the air-Au side and probed the glass-Au side. (c) Diffracted front-probe and back-probe signal as a function of pump-probe delay at various pump fluences for 45 nm gold layer and (d) 100 nm gold layer.

$\Delta T_e(t)$, is thus determined by the difference between the temperatures in the bright and the dark fringes. The heating of the electron gas leads to changes in the complex dielectric function of the metal. A grating in the electron-gas temperature thus leads to a grating in the dielectric function. From this grating, a probe pulse can be diffracted. As such, the diffracted signals observed in Figure 4.4 (c) and (d) are correlated with the dynamics of $\Delta T_e(t)$.

The rapid decay, observed during the first 0.5 ps for the 100 nm thick

sample, was not observed by Hohlfeld et. al. [61], presumably because they used longer pulses in their experiments which may have given rise to a smearing out of the sharp peak. Interestingly, the results show that for the 45 nm gold film the signal shapes for the front and back-probe signals are very similar. This observation agrees with the assumption that for thin layers, after optical excitation, the electron energy is quickly redistributed relatively homogeneously throughout the layer [61]. This redistribution causes the measured dynamics, now dominated by electron cooling through lattice heating, to be the same everywhere. However, for the 100 nm gold layer, the front- and back-probe signals are different. There, we find that the front probe signal shows a rapid rise and decay, but that the back-probe signal rises more slowly. For pump-probe time delays larger than about 0.5 ps, the signals look similar and, again only one vertical scaling factor is applied to the back-probe signals to overlap all the front- and back-probe signals for this sample. The sharp rise/fall time of the front-probe signal and the slower rise of the back-probe signal are the result of ballistic transport and diffusion of electron energy out of the front-surface front-probe interaction region towards and into the back-probe interaction region near the Au-glass interface [61]. For 100 nm Au this process takes a few hundred femtoseconds which explains the slower rise of the back-probe diffracted signal. This also means that after this time the electron energy distribution should be relatively homogeneous again, explaining why for delays larger than about 0.5 ps the front-and back-probe signals look similar.

4.4.2 Electron dynamics in Gold-Platinum bilayers

To better understand the measurements on buried gratings discussed later in this chapter, we also studied the effect that a buried metal layer has on the electron dynamics observed at the gold surface. Initially, we chose platinum as the buried metal layer due to its very high electron-phonon coupling strength when compared to gold. In Figure 4.5 (a) we plot the measured diffracted front-probe diffraction efficiency versus pump-probe time delay for a bilayer consisting of 30 nm of Au deposited on 30 nm of Pt. In the same figure, we also plot the time-dependent front-probe diffraction efficiency for a single 30 nm thick layer of Au. The figure shows that the

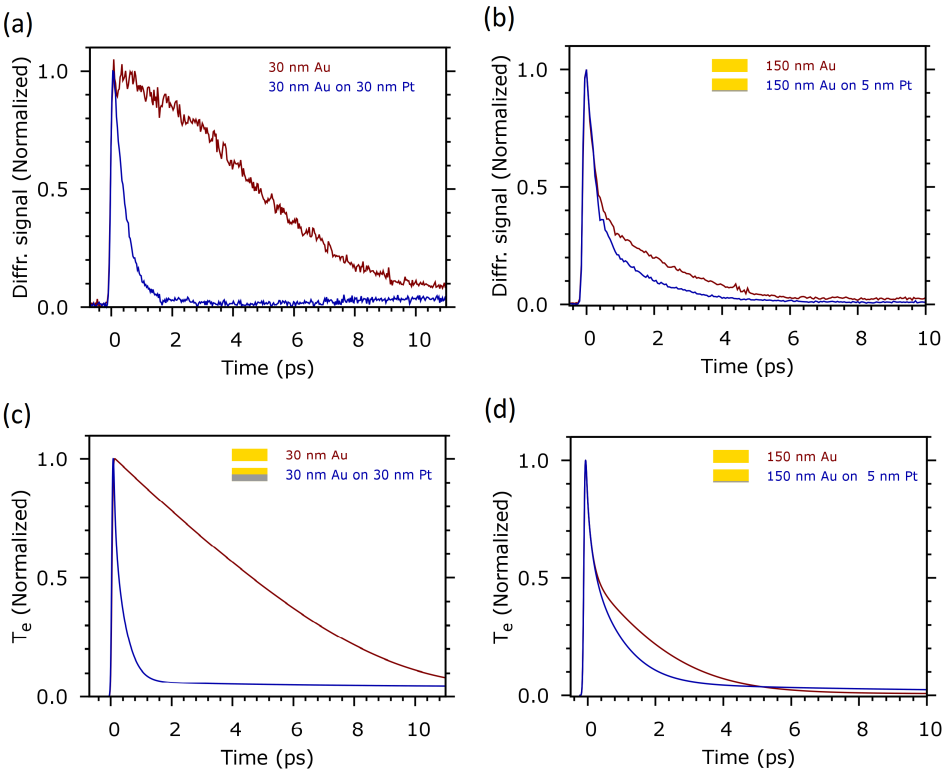

Figure 4.5: (a) The measured front-probe diffracted signal vs. pump-probe delay for a pump fluence of 0.80 mJ/cm^2 on a sample with 30 nm Pt under 30 nm Au. (b) The experimentally measured front-probe diffracted signal vs. pump-probe delay on a sample with 5 nm Pt under 150 nm Au. (c) The numerically calculated electron temperature T_e vs. time for the sample with 30 nm Pt under 30 nm Au. (d) The numerically calculated T_e vs. time for the sample with 5 nm Pt under 150 nm Au.

presence of the Pt layer underneath the gold dramatically accelerates the decay of the diffracted probe signal. Note that, although no signal for a Au thickness of 60 nm was measured, the results shown in Figure 4.4 for 45 and 100 nm thick single Au layers suggest that for 60 nm of gold, the decay would be in between these two cases and would still be significantly slower than for 30 nm of Au on Pt. To determine the limits of the effect that Pt has on the decay of the measured diffracted signal, we plot in Figure 4.5 (b) the front-probe diffraction efficiency versus pump-probe delay for a sample consisting of 150 nm of Au on 5 nm of Pt and for a sample consisting of 150 nm Au only. This gold layer thickness was chosen to eliminate the

possibility of the 400 nm pump beam directly exciting the Pt since the 400 nm light has a penetration depth of about 16 nm in Au. Remarkably, the results show that for this particular bilayer, even the effect of a buried Pt layer as thin as 5 nm on the shape of the diffracted signal versus pump-probe delay, is still measurable. The tell-tale sign of the effect of the buried Pt layer is that the transition from an initial fast decay to a slower decay, as observed in the gold-only sample, is absent. This means that the difference between the single Au layer and the bilayer manifests itself most strongly for longer time delays, as shown in Figure 4.5 (b).

This difference in decay due to the presence of a platinum layer can be simulated using TTM calculations. In Figure 4.5 (c) and Figure 4.5 (d), we plot the calculated electron temperature at a depth of 8 nm from the top surface of the gold layer as a function of time, using the same parameters as in the experiments. For the sample with 30 nm Au on top of 30 nm Pt, the electron temperature decreases rapidly due to the presence of the platinum layer. For the sample with 5 nm Pt under 150 nm Au, the electron temperature decreases at a slightly slower rate than in 150 nm Au. We note that the calculation of the time-dependent electron temperature closely resembles the measurements of the diffraction efficiency versus pump-probe time delay.

We can explain this behavior by looking at the electron-lattice dynamics occurring in the buried platinum layer. After optical excitation, the electron energy diffuses deeper into the gold layer and beyond into the platinum layer. The electron-phonon coupling constant of platinum, however, is about two orders of magnitude higher than that of gold. This means that thermalized electrons that diffuse into the platinum, immediately lose energy to the Pt lattice and quickly cool. Thus, a strong electron-temperature gradient between the gold and platinum layer is maintained, which in turn drives the rate of electron gas energy diffusion out of the probe interaction region near the surface of gold into the deeper regions of the gold and into the platinum layer. These results are interesting, because they show that even a Pt layer as thin as 5 nm has a measurable effect on the decay observed near the surface of a 150 nm thick Au layer. This suggests that a pump-probe technique may be used for sub-surface metrology, in particular the localization and inspection of buried structures underneath optically

opaque metal layers.

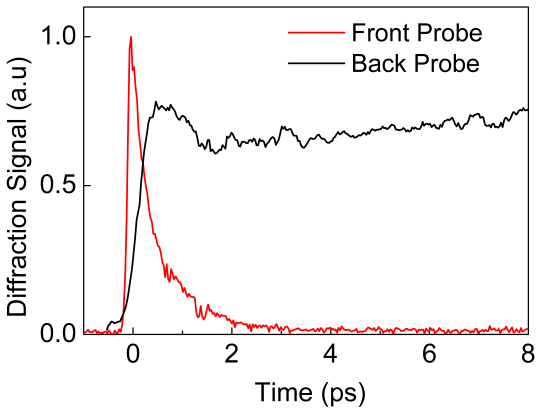

Figure 4.6: The measured diffracted signal from the front-probe (red) and back-probe (black) for a pump fluence of 0.80 mJ/cm^2 on a sample with 30 nm Pt under 30 nm Au.

To confirm that the energy is deposited in the Pt layer, we performed experiments on a sample with 30 nm platinum on 30 nm gold in which we pump from the gold side and probe from the platinum side (back probe) as well as the gold side (front probe). In Figure 4.6, we plot the diffracted front-probe and back-probe signal as a function of the pump-probe delay. As it is difficult to compare the absolute diffraction efficiencies for the front and back-probe cases, we instead applied a scaling factor to the back-probe signal so that both the front-probe signal and the back-probe signal can be plotted in the same graph. The back probe signal was smoothed by nearest neighbor averaging. For the front probe, the signal rises rapidly and then decays in 1-2 ps, indicating a rapid drop in electron temperature. This plot is similar to Figure 4.6 (a) and the physics has been discussed earlier in this section. In contrast, the signal from the back probe shows a gradual increase for about 0.7 ps followed by a small decrease to a lower value and then continues to increase very slightly.

This different behavior of the back probe signal vs. pump-probe time delay can be explained by including the lattice dynamics of the Pt-Au layer. The initial rise of the back-probe signal seen in Figure 4.6 is interpreted as resulting from the diffusion of electron energy into the Pt layer and

simultaneous heating of the Pt lattice by the electron gas. The small decay is the result of the cooling of the electron gas, but it is superimposed on the growing signal caused by the heating of the lattice. The slow and weak increase of the signal after 2 ps is real. The TTM calculations (not shown here) indicate that, at a time delay of about 1 ps, the Pt lattice temperature has a strong gradient, being higher near the Pt/Au interface and lower near the back of the Pt, where the probe pulse interacts with the Pt. Equilibration of the difference occurs through electron energy diffusion, where electrons pick up the lattice energy from the hotter regions, and deposit this in the cooler regions. The latter gives rise to a slowly increasing lattice temperature in the regions where the probe pulse interacts with the Pt and thus an increasing diffraction signal. Our measurements are consistent with observations made in the context of ultra-high frequency sound-wave generation by indirect heating of Ti underneath Cu on a Cu-Ti bilayer, where indirect heating of a Ti layer underneath a Cu layer was shown to generate ultra-high frequency sound-wave packets [86].

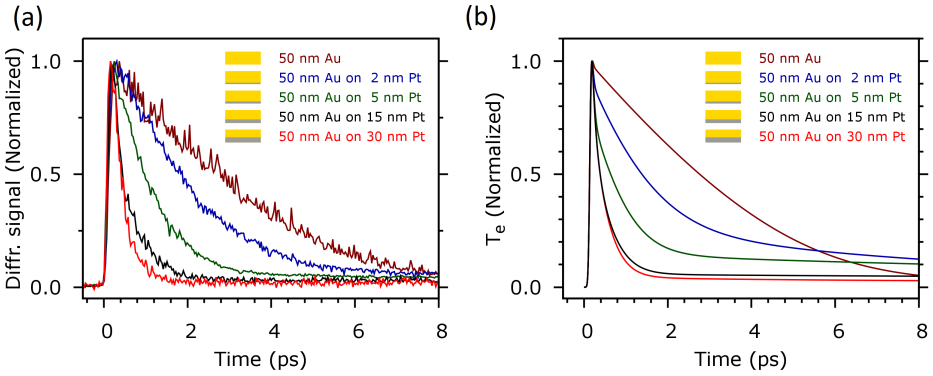

Figure 4.7: (a) The measured front-probe diffracted signal vs. pump-probe delay for a pump fluence of 0.96 mJ/cm^2 on bilayer samples with different thicknesses of platinum (0, 2, 5, 15, 30 nm) buried under 50 nm gold, (b) The numerically calculated electron temperature T_e vs. time for these samples using the same pump fluence as used in the experiment.

To more systematically study the effect of the thickness of the Pt layer on the probe-diffraction decay curves, we fabricated samples in which we kept the Au layer thickness fixed while varying the Pt layer thickness. In Figure 4.7 (a), we plot the measured front-probe diffraction signal as a function of

pump-probe delay from bilayer samples having a buried Pt layer thickness of 0, 2, 5, 15, and 30 nm underneath a 50 nm layer of Au. The pump fluence in these experiments is 0.96 mJ/cm^2. The results clearly show that thicker Pt layers lead to a more rapid decay of the probe diffraction efficiency versus pump-probe time delay. Remarkably, even a Pt layer as thin as 2 nm is capable of speeding up the measured decay significantly.

In Figure 4.7 (b), we plot the calculated electron temperature at a depth of 8 nm from the top surface of gold as a function of time for these samples. In the simulation, the same parameters were used as in the experiment. The calculations show that the electron temperature decays faster for samples with a thicker layer of platinum buried underneath and are in good agreement with the experimental results. However, the constant level to which the curves decay, seen in the calculation, is somewhat higher compared to what is observed in the experiments.

We can intuitively understand this behavior as a thicker layer of platinum acts as a more effective electron energy heat sink. This results in a higher rate of diffusion of electron energy out of the optical probe interaction region near the Au surface, and a subsequently more rapid drop in electron temperature. This measurement thus shows that some measure of control of the rate of diffusion of electron gas energy between the two metal layers is possible by varying the buried metal thickness. In fact, changing the thickness of the buried platinum also affects the maximum Pt lattice temperature reached, after optical excitation. This study might also help to better understand the ablation mechanism and threshold in metallic bilayers [78].

4.4.3 Electron dynamics in bilayers with other metals

To confirm that it is the strength of the electron-phonon coupling constant that is responsible for the increase in the observed probe diffraction decay rate, we also fabricated bilayers in which we varied the type of metal underneath the gold layer. In Figure 4.8 (a) we plot the front-probe diffracted signal as a function of pump-probe time-delay, for bilayers consisting of 50 nm of Au on top of 30 nm of four different metals, being: Pt, Cu, Ag and Au, (the last case thus consisting of 80 nm of Au in total). For complete-

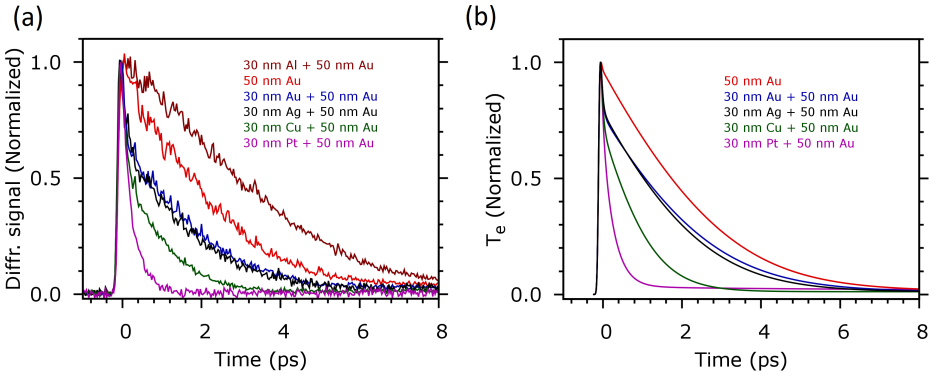

Figure 4.8: (a) The measured front-probe diffracted signal vs. time for a pump fluence 0.80 mJ/cm^2 for bilayer samples with different materials buried under 50 nm Au. (b) The numerically calculated electron temperature T_e vs. time for the same pump fluence as used in the experiments.

ness, we also show the results for a 50 nm single layer of gold. The pump fluence in these measurements was 0.80 mJ/cm^2.

The Figure 4.8 (a) shows that the decay of the diffraction efficiency versus time for 50 nm of Au on Pt, also shown in Figure 4.7 (a), is the fastest, followed by Au on Cu, which is also faster than 50 nm + 30 nm of Au only, but slower than the signal for Au on Pt. The decay for 50 nm Au on 30 nm Ag is about as fast as that for 50 nm Au + 30 nm Au. In agreement with the results shown in section 4.4.1, the signal for 80 nm of Au decays faster than the signal for 50 nm of gold.

In Figure 4.8 (b), we plot the calculated electron temperature at a depth of 8 nm from the surface of Au as a function of time for these samples. The decay of the electron temperature is fastest for the sample with a buried layer of platinum. The decay gets slower as the buried layer is changed from platinum to copper to silver and finally to gold. This is in good agreement with the experimental results. The decay of the measured diffracted signal correlates with the strength of the electron-phonon coupling in the various metals listed in Table 4.1 , with materials having a stronger electron-phonon coupling showing a faster decay. The electron-phonon coupling constants of Ag and Au are more or less the same and so are the measured decay rates.

4.4.4 Detection of a buried grating

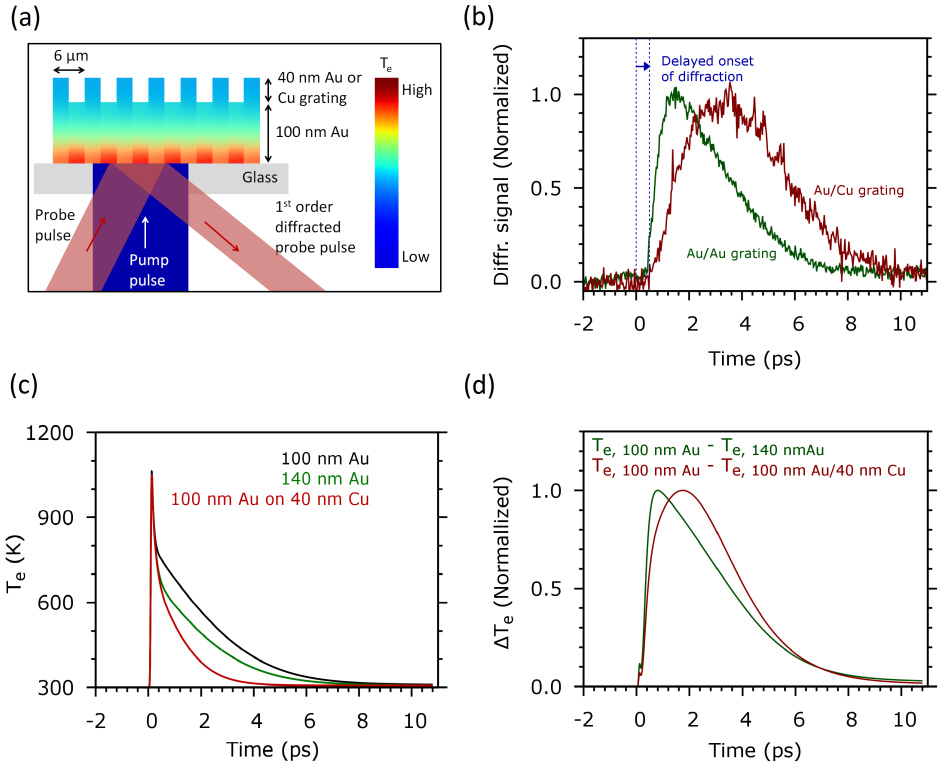

Figure 4.9: (a) The schematic of the experimental setup. The single 400 nm pump pulse illuminates the flat 100 nm Au from the glass side. The probe pulse diffracts off the spatially periodic electron temperature that is created due to the difference in the electron diffusion behavior caused by the 40 nm Au/Cu. Schematic of the electron temperature after 1 ps is shown using the colour scheme. (b) The measured diffracted signal vs. time from the glass-Au interface. (c) Numerically calculated electron temperature T_e vs. time for 100 nm Au (black), 140 nm Au (green) and 100 nm Au (red) on 40 nm Cu (d) The difference between the calculated T_e for 100 nm Au and 140 nm gives the green curve. This is similar to the measured green curve from a 100 nm Au with 40 nm Au grating underneath. The difference between the calculated T_e for 100 nm Au and 140 nm Au/40 nm Cu gives the red curve. This is similar to the measured red curve from a 100 nm Au with 40 nm Cu grating underneath.

To demonstrate that thermalized electron gas dynamics can be used to detect buried structures, we evaporated 100 nm Au on a glass substrate and fabricated a 40 nm thick Au grating with a 6 µm pitch and 50% duty cycle with UV lithography on top of this layer, as schematically shown in Fig-

ure 4.9 (a). A similar sample was also made with a 40 nm Cu grating on top of a 100 nm Au layer. We performed a pump-probe experiment with a single pump pulse on these samples by pumping and probing from the *substrate* side. Thus, both the pump and the probe beam see a nominally flat surface and the grating is optically hidden. Since we pump from the glass side, where the gold is flat, we will henceforth refer to the gratings on top as "buried" gratings. We chose to fabricate gratings on top of the flat layer, to ensure that there is no residual topography of the grating at the flat top surface (which, in this case, is at the glass-Au interface). The other way around, evaporating Au onto a metal grating, leaves a residual grating topography at the top surface which gives rise to a significant diffraction, even after polishing. In the experiments described in the previous sections we used two pump pulses, forming a spatially periodic interference pattern, to excite the sample. This gives rise to a spatially periodic electron gas temperature leading to a spatially periodic complex dielectric function. In contrast, here, we use a single pump pulse to homogeneously illuminate the sample. In what follows, we argue that the observation of first-order diffraction in this case is proof that a spatially periodic electron gas temperature pattern is nonetheless also formed. Such an electron gas temperature grating, following homogeneous excitation, can be formed due to the different rates of electron gas energy diffusion above the valleys and above the ridges of the grating. As we have shown in the previous sections, differences in the electron-energy diffusion rate can be caused both by differences in the thickness of a metal and also by the type of metal buried underneath. The former is illustrated by the gold grating behind a flat gold layer, the latter by a copper grating behind a flat gold layer. In Figure 4.9 (b), we plot the first-order diffracted signal for both the Au on Au grating and the Cu on Au grating. We find that the onset of diffraction is delayed, in comparison to the measured time-dependent diffraction using two interfering pump-pulses on a flat region on the same sample, by about 0.4 ps. After this time, diffraction is observed but surprisingly, the diffracted signal increases slower than for a single Au layer. For the Au-Au grating the rise time is about 1 ps, whereas for the Cu-Au grating we observe a rise time of about 3 ps. We emphasize that with a single pump, and thus without pump interference grating, the observation of diffraction in itself implies a grating in the optical constants of Au near the glass-Au interface, caused

by the buried gratings. Indeed, when we pump the samples in a region where no grating is present and where, for the Au-Au sample, the sample consists of a 100 + 40 nm single layer of Au, no diffraction was observed. The observation of diffraction also implies that lateral, in-plane diffusion of the electron energy is not strong enough to destroy the grating contrast. This is to be expected considering the large value of 6 µm of the grating period with respect to the typical distance of 200 nm over which electron energy can diffuse in gold [87]. We note that in the measurements on flat bilayer samples, shown in Figure 4.8, the diffracted signal decays faster for Au on Cu than for Au on Au. The reason for this is that Cu has a larger electron-phonon coupling constant which results in a faster diffusion of electron energy out of the probe interaction region near the gold surface. The diffracted signal dynamics for the Cu-Au grating is slower than for the Au-Au grating. This is in sharp contrast to the faster decay we observe for the Au on Cu flat samples in the diffraction experiments described in section 4.4.3. To understand this, it is important to realize that here, the grating is also the result of a spatially periodic electron gas temperature $T_e(t)$ giving rise to a spatially periodic dielectric function. In the case of the two-pump-pulse experiments described in sections 3.4.1 to 3.4.4, the spatially periodic electron gas temperature is the result of excitation of the metal with two spatially and temporally overlapping pump pulses. In contrast, here, using a *single* pump pulse, immediately after optical excitation before energy diffusion has a significant impact on the electron gas temperature, there is no temperature grating. The electron gas temperature is high, but more or less homogeneous along the glass-Au interface. After a short while, electron gas energy diffusion lowers the electron gas temperature at the glass-Au interface, but at a faster rate above the ridges than above the valleys of the buried grating. The resulting temperature contrast (difference) $\Delta T_e(t)$, leads to a grating in the dielectric constant, in a manner similar to the case where two interfering pump pulses were used. There, however, the lowest temperature in the dark fringes always remains at 297 K and the maximum temperature is reached in the bright fringes immediately after optical excitation. Here, for the buried grating, using calculations based on the two-temperature model as shown in Figure 4.9 (c) and Figure 4.9 (d), we find that the *difference* temperature shown in Figure 4.9 (d) reaches its maximum at a time when the absolute electron

temperature in the different regions has already dropped significantly as shown in Figure 4.9 (c). The calculated ΔT_e reaches its maximum value at ≈ 0.8 ps for Au-Au grating whereas the measured diffracted signal reaches its maximum at 1.3 ps. Similarly, for the Cu-Au grating, the calculated ΔT_e reaches a maximum value at 1.8 ps whereas the measured diffracted signal reaches a maximum at 3.6 ps. These calculations contain the essential features of the measurement, in particular the slow rise of the difference temperature, which is more pronounced for the 40 nm Au + 100 nm Au sample than for the 40 nm Cu + 00 nm Au sample. We note that the decay curves for the electron temperatures, calculated for 100 nm Au, 140 nm Au, and 40 nm Cu on 100 nm Au, are quasi-parallel as shown in Figure 4.9 (c). This means that small changes in the shape of these signals will have a dramatic effect on the exact time where the difference temperature reaches its maximum.

4.5 Conclusion

We have shown pump-probe diffraction measurements of the thermalized electron gas dynamics in single metal layers and in metallic bilayers. Our measurements on Pt/Au samples show a rapid decay in the measured diffracted probe signal, after optical excitation with a pump pulse, indicating a rapid cooling of the electron gas at the gold surface due to the presence of the buried platinum layer. We find that this decay increases with increasing Pt layer thickness. Even for a sample with 5 nm Pt under 150 nm Au, we observe a measurable effect on the shape of the time-dependent diffracted signal as compared to 150 nm Au only, illustrating the sensitivity of electron diffusion near the gold surface on the presence of a buried layer such as Pt. The decay of the diffracted signal is also found to be dependent on the type of buried metal layer and is correlated with the electron-phonon coupling strength of the buried metal. In experiments with a single pump beam, we demonstrate that thermalized electron dynamics can be used for the detection of buried gratings underneath an optically opaque layer of Au. We show that the shape of the time-dependent diffracted signal is different for a Cu grating on Au compared to a Au grating on Au. The peak in the diffracted signal occurs a few picoseconds later compared to what is observed for experiments on non-structured metal layers and bilay-

ers. The TTM numerical calculation of the electron temperatures shows good agreement with our measurements. The experiments demonstrate that thermalized electron gas dynamics can be used to detect optically hidden structures underneath metals like gold and hint at the possibility to image periodic and non-periodic, micro- and nano structures buried below opaque metal layers.

5

Acoustic waves in flat metal and dielectric layers

Prior to experiments on samples with buried gratings, we performed a set of experiments to obtain a basic understanding of the acoustic wave generation, propagation, and detection in metals. In this chapter, the measurements and calculations of transient-grating pump-probe experiments on flat metal layers are discussed. We show that grating-shaped acoustic waves can be generated in Au, Ni and W layers, and also that the presence of the acoustic echo can be detected by diffracted light from the grating-shaped acoustic wave.

Parts of this chapter has been published as Phys. Rev. Appl. **13**, 014010 (2020) [18].

5.1 Introduction

We performed femtosecond transient-grating pump-probe experiments on flat metal layers deposited on a glass substrate. The aim of these experiments is to see if it is possible to launch and detect acoustic echoes in the metal layers using our transient-grating pump-probe setup. Although in the past, various groups have shown the generation and detection of acoustic waves in metal layers, most of these experiments were performed using a pump-probe setup in reflection or transmission geometries [29,30,38,40,42,86,88–121]. In a typical pump-probe setup, the pump pulse launches an acoustic wave, and the change in reflectivity of the metal due to the acoustic wave is measured using the probe pulse. However, in our experiments, we launch a *grating-shaped* acoustic wave using two interfering pump pulses and detect diffraction from the acoustic echoes using a time-delayed probe pulse.

In this chapter, we show the results of the transient-grating pump-probe experiments on flat metal layers. The first set of measurements on flat Au layers having different thicknesses shows that our transient-grating pump-probe setup is capable of generating and detecting acoustic waves. The measurements on a 500 nm thick Au layer, where we pump from the air-metal side and probe from the air-metal side and from the glass-metal side, provide information on the various effects that determine the temporal shape of the diffraction signal, such as electron energy diffusion and the thermo-optic effects. We also perform measurements on flat Ni and W layers that show that the frequency of the acoustic waves generated in Ni and W is much higher than the one generated in the Au layer. We demonstrate that a thin layer of Ni can be used as an acoustic transducer to launch a *high*-frequency acoustic wave in Au. To understand how the acoustic waves propagate through a sample consisting of a metal and a dielectric, we also performed measurements on a sample that has a thin layer of SiO_x sandwiched between two Au layers.

5.2 Experimental setup

We use the same transient-grating setup as the one described in Chapter 4. In the experiments shown here, we have a transient-grating period of approximately 6 µm. The spatially-periodic interference pattern excites the metal layer resulting in spatially periodic heating of the sample surface, thus launching a grating-shaped acoustic wave. The grating-shaped acoustic wave propagates through the metal layer, reflects from the metal-substrate interface, and returns to the top surface. The weaker 800 nm pulse is used as the probe and is delayed with respect to the 400 pump pulses by a mechanical delay line, which increases the optical path length. The probe pulse diffracts from the grating-shaped displacement of the metal atoms or from the spatially periodic change in the refractive index of the metal surface induced by the acoustic waves. The diffracted probe pulse is recorded by a silicon photodiode placed at the position where we expect the first-order diffracted beam. The diffracted probe signal recorded by the detector when the chopper blocks the pump beam, is subtracted from the diffracted probe signal when the pump beam is transmitted by the chopper, and plotted as a function of the pump-probe delay. The signal recorded by the detector in the absence of the pump pulse is from the probe light scattered by the surface roughness of the sample. Depending on the experiment, we probe from the air-metal side or from the glass substrate side. In the latter case, the probe pulse passes through the glass substrate and probes the metal near the glass-metal interface. The pump beam has a spot size of 1.5 mm on the sample, and the pump pulse energy ranges from 15 µJ to 20 µJ depending on the experiment. The probe pulse energy was kept constant at 1 µJ.

5.3 Results and discussion

5.3.1 Acoustic waves in Au

Our first experiment was to launch and detect grating-shaped acoustic waves in a flat metal layer (schematic in Figure 5.1 (a)). We chose Au for the initial experiments because Au is one of the most well-studied metals. In Figure 5.1 (b), we plot the measured diffraction signal as a function

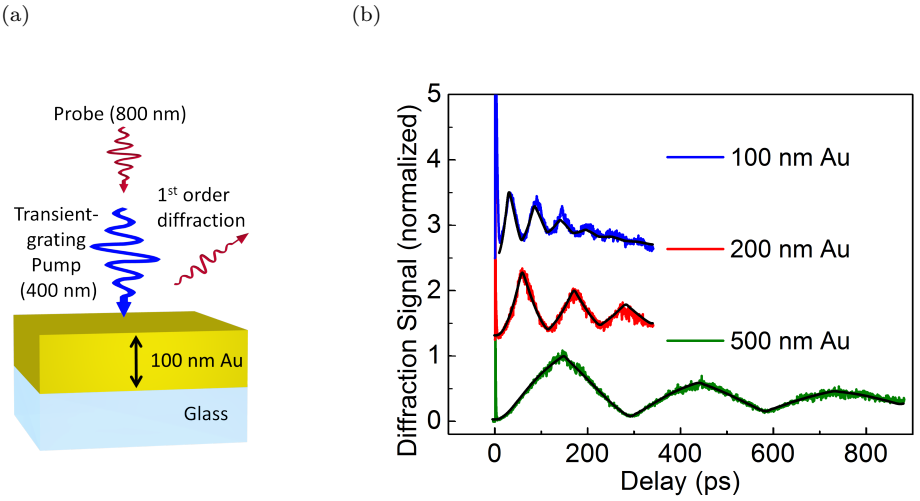

Figure 5.1: (a) Schematic of the experiment. (b) Measured diffracted signal as a function of pump-probe delay for a 100 nm, 200 nm and 500 nm Au layer on a glass substrate. The plots are vertically offset for clarity. The black curves are the simulated diffracted signals.

of pump-probe delay for 100 nm, 200 nm, and 500 nm thick flat Au layers on a glass substrate. In all the measurements, the diffraction signal increases just after the optical excitation with the pump pulses and decreases again within the first 10 ps. This signal is due to the absorption of the optical energy by the electron gas, which then cools on a time-scale of < 10 ps by heating the lattice (see Chapter 4), until the electron gas temperature and lattice temperature are the same.

For the 100 nm Au sample, we see an oscillatory signal with peaks at 33 ± 3 ps, 89 ± 3 ps, and 145 ± 3 ps. The time separation between the peaks is approximately 56 ps, which is close to the expected round trip time of an acoustic wave inside a 100 nm thick Au layer, assuming an acoustic velocity of 3200 m/s in Au [30]. When the thickness of the Au layer is doubled to 200 nm, the time separation between the peaks also doubles to about 111-112 ps. Similarly, for the 500 nm thick layer, the observed round trip time is close to 280 ps. Interestingly, for measurements on all three samples, the first peak is at a time that corresponds to half the round trip time of the

acoustic wave in Au.

To better understand the experimental results, we first have to explain how acoustic waves are generated in Au layers. The hot electron gas created due to the absorption of the pump pulses cools by rapidly heating the lattice. The rapid heating launches the acoustic wave. We know that the hot electron gas diffuses deeper into the Au layer due to the low electron-phonon coupling strength in gold. As a result, the spatial extent of the acoustic wave generated is much larger than the optical penetration depth (approximately 16 nm for 400 nm light) [83, 85]. For 100 nm and 200 nm thick Au layers, we expect the Au layer to more or less homogeneously heat up along the thickness of the layer. The resulting rapid expansion of the layer launches acoustic waves that causes an expansion and contraction of the lattice in a direction perpendicular to the surface.

The acoustic wave inside these Au layers can be seen as a standing wave formed by the addition of two counter-propagating acoustic waves, each having a wavelength corresponding to twice the thickness of the Au layer. In the 500 nm Au sample, the Au layer is not homogeneously heated due to the finite penetration depth of the electron gas energy. As a result, the spatial extent of the acoustic wave is approximately 300 nm. In all the measurements, the acoustic wave inside the Au layer remains grating-shaped because the lateral diffusion of heat can be ignored on the time scale of our experiments (< 1 ns) as the grating pitch is much larger than the thickness of the Au layer. Hence, in all of the samples, we have a grating-shaped acoustic wave bouncing back and forth in the Au layer.

The spatially periodic optical excitation of the Au layer gives rise to two effects: a thermal expansion of the layer and the launch of a grating-like acoustic wave. The thermal expansion leads to a quasi-static grating-shaped surface displacement, while the transient-grating acoustic echo results in a strongly time-dependent grating-shaped surface displacement. Both effects act as a phase grating as seen by the probe pulse. In the Au samples, the thermal expansion grating is formed about 10 ps after the optical excitation and is present for hundreds of picoseconds. In all of the measurements on Au samples, the displacement grating due to the acoustic echoes interferes with the thermal expansion grating present at the sur-

face. If *only* the thermal expansion grating gave rise to the diffraction of the probe pulse, then we would expect a quasi-constant diffraction signal from 10 ps to 700 ps. However, when the grating-shaped acoustic echo arrives at the air-Au interface, it destructively interferes with the quasi-constant thermal expansion grating. As a result, we observe a trough in the time-dependent diffraction signal. In short, in all of the measurements in Figure 5.1 (b), the *troughs* in the diffraction signal corresponds to the arrival of the acoustic echoes. The position of the first trough after 10 ps in all measurements matches the acoustic round trip time inside the Au layer.

The best-fit model calculations for the measured data for all three Au layer thicknesses are shown by the black curves in Figure 5.1. The calculation is based on the model discussed in reference [18]. We obtain an excellent agreement between the measured and the calculated diffraction signal. It was observed in the calculation that the contribution from surface displacement (due to thermal expansion and acoustic wave) alone can explain the shape of the measured data very well. Note that the electron gas response is not included in the model but it is used as an input in the calculation. Therefore, only the data points for t>10 ps, when the electron gas has thermalized with the lattice, are used in the calculation.

To confirm that the arrival of acoustic echoes corresponds to the troughs in the diffraction signal, we performed experiments on the 500 nm thick Au sample, where we also measure the diffraction signal from the substrate side, as schematically shown in Figure 5.2 (a). Due to the finite penetration depth of the electron gas energy, heating of the lattice is expected to be absent near the substrate side, and the diffraction signal should be dominated only by the acoustic wave. The measured diffraction signals as a function of time are shown in Figure 5.2 (b). The red curve shows the diffraction signal when probed from the metal side (front probe), and the green curve shows the diffraction signal when probed from the substrate side (rear probe). The red curve in Figure 5.2 (b) is the same as the green curve in Figure 5.1 (b) but normalized to the peak at 145 ps. When measuring the diffraction signal from the glass side (green curve), we observe that the signal increases and reaches a maximum at 147 $\pm$ 3 ps, which coincides with the position of the peak in the red curve. Unlike the red curve, the green curve does not have a peak between 0-10 ps, associated with a grating in the electron

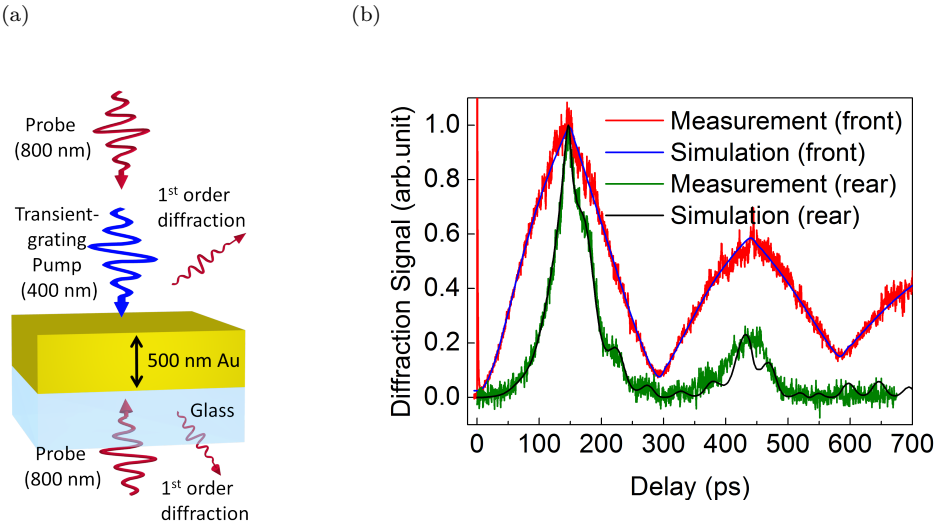

Figure 5.2: (a) Schematic of the experiment. (b) Transient-grating pump-probe measurements on a 500 nm thick Au layer on a glass substrate. The red curve shows the diffraction signal when probed from the air-metal side (front probe) and the green curve shows the diffraction signal when probed from the substrate side (rear probe). The blue and black curves are the simulated diffracted signals.

temperature, showing that the electron gas energy does not diffuse to the rear of the sample.

When we probe from the glass side, we do not have any contribution to the diffraction signal from the thermal expansion grating. This is because the lattice temperature grating is very weak at the Au-glass interface. The hot electron gas energy created at the top surface of the Au layer does not diffuse deep enough into the 500 nm Au layer to give rise to a significant lattice temperature increase. Due to the absence of these effects, the peaks in the green curve correspond to the arrival of the acoustic wave at the Au-glass interface. As the troughs in the red curve correspond to the arrival of the acoustic wave at the air-metal side, the peak in the red curve is observed when the acoustic wave is farthest from the air-metal side, which is when the acoustic wave is near the Au-glass interface. Therefore, the peaks of the red and the green curve should coincide as we observe in the measurements.

The time separation between the peaks of the green curve is close to the acoustic round trip time inside 500 nm Au. The rise-time of the diffraction signal can be understood from the spatial extent of the acoustic wave generated inside the Au layer. As the rise-time of the first peak in the green curve is about 100 ps, we can estimate that the acoustic wave generated inside gold has a spatial extent of approximately 320 nm. These measurements supports our argument that the trough in the diffraction signal, when probed from the air-metal side, corresponds to the arrival of the acoustic echoes at the surface. This is also confirmed by the numerical simulation shown by the blue curve and the black curve for front and rear probing, respectively (Figure 5.2 (b)). These simulations also confirm that the main contribution to the diffraction signal is the grating-shaped displacement of the metal atoms. The diffraction of the 800 nm probe pulse due to the strain-optic and thermo-optic effect in Au is negligible. When probed from the glass side, we also expect a diffraction signal due to the grating-shaped acoustic wave propagating in the glass substrate. The grating-shaped acoustic wave can cause a change in the refractive index of the glass due to the strain-optic effect. Such a grating, propagating away from the metal-glass, can lead to oscillating diffraction signals as a function of time delay. This is commonly referred to as Brillouin scattering and is explained in detail in the next chapter. In this measurement shown in Figure 5.2 (green curve), we see hints of the oscillatory signal in the diffraction caused by Brillouin scattering in the glass. The effect is not very prominent because the diffraction due to the grating-shaped displacement of the interface dominates the total measured diffraction signal.

5.3.2 Acoustic waves in Ni and W

Now that we can launch and detect acoustic waves in Au layers, we performed experiments on metals which have higher electron-phonon coupling strengths than Au. As a result, we expect that the spatial extent of the generated acoustic wave to be smaller than that in Au. In this section, we show the results of transient-grating pump-probe measurements on flat nickel (Ni) and tungsten (W) layers on a glass substrate, when pumped and probed from the air-metal side (schematically shown in Figure 5.3 (a)). In Figure 5.3 (b), we plot the measured first-order diffraction signal

(a) (b)

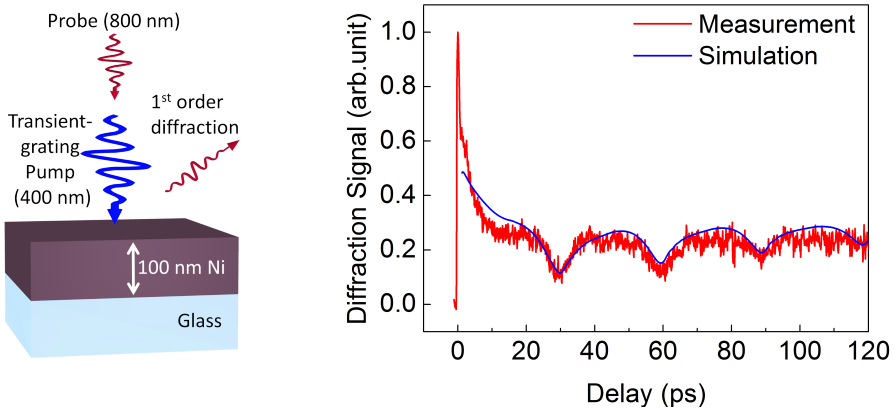

Figure 5.3: (a) Schematic of the experiment. (b) Transient-grating pump-probe measurement on a 100 nm thick Ni layer. The red curve shows the measured diffracted signal and the blue curve shows the calculated diffracted signal.

as a function of the pump-probe delay for a 100 nm thick Ni layer on a glass substrate (red curve). We observe that the measured diffraction signal increases rapidly within 100 fs after optical excitation, and then drops to a lower value within 2 ps and drops further in 10 ps. The diffraction remains quasi-constant after 10 ps except for sharp periodic troughs at 29 $\pm$ 2 ps, 59 $\pm$ 2 ps, and 89 $\pm$ 2 ps. The rapid increase in diffraction signal around 0 ps and the decay within 2 ps, is due to the generation of a hot electron gas followed by the cooling of the electron gas by heating of the Ni lattice. The cooling of a hot electron gas in Ni is faster than for Au because the electron-phonon coupling strength in Ni is 12 times larger than that in Au [21].

Similar to the measurements on Au layers, in Ni the troughs in the diffraction signal correspond to the return of the longitudinal acoustic wave to the surface following reflection from the Ni-substrate interface. The multiple troughs in the diffraction signal show that the longitudinal acoustic wave bounces back and forth inside the Ni layer a few times. The position of the first trough (at 29 ps) and the time separation between the troughs (29-30

ps) match the calculated acoustic round trip time in a 100 nm thick Ni layer, using an acoustic velocity of 5800 m/s [40]. The overall background diffraction signal seen between 2-120 ps, is due to the thermal expansion and the thermo-optic effect in Ni. The transient-grating pump pulses heat the Ni layer in a spatially periodic pattern, which results in a grating-like thermal expansion and a lattice temperature grating. This lattice temperature grating changes the refractive index of the Ni layer due to the thermo-optic effect. The delayed probe pulse can also diffract from this refractive index grating. The total diffracted signal is a coherent sum of the electric fields of the individual contributions, rather than a direct sum of diffraction efficiencies.

In Ni, the troughs in the diffraction signal caused by the acoustic echoes are sharper than in the case of Au. This can be explained by the stronger electron-phonon coupling strength and higher acoustic velocity in Ni. The hot electron gas generated within the optical penetration depth of 13 nm in Ni [122], rapidly cools to heat the lattice before the energy can diffuse deeper into the Ni. The generated acoustic wave is more localized in the propagation direction than in the case of Au. Hence the acoustic wave has a much higher frequency, and gives rise to sharper troughs in the diffraction signals. Our interpretation of the measured data is confirmed by the numerical simulation shown by the blue curve in Figure 5.3 (b), which is in good agreement with the measurements.

We also performed transient-grating pump-probe experiments on a 100 nm layer of tungsten (W) on glass, as schematically shown in Figure 5.4 (a). In Figure 5.4 (b), we plot the measured diffraction signal as a function of time delay for this sample (red curve). Similar to the measurement on the 100 nm Ni sample, we observe a sudden increase in the diffraction signal between 0-100 fs followed by a decrease within 2 ps. We see troughs in the diffraction signal at 32 $\pm$2 ps and 64 $\pm$2 ps. The troughs we observe are on top of a slowly decaying background diffraction signal. The troughs are caused by the return of the acoustic wave to the W surface after reflecting off the W-glass interface. The slowly decreasing background is due to the diffraction of the probe pulse from the grating-like thermal expansion of the layer and a lattice temperature grating (thermo-optic effect). The decrease in the background is due to the diffusion of lattice heat away from the

probing depth in W. The decay of the background is faster than in case of Ni most likely because W has higher thermal conductivity than Ni which leads to faster heat diffusion from the probing region. The fast decay of the electron dynamics signal between 0 ps and 2 ps, and the sharpness of the troughs at 32 ± 2 ps and 64 ± 2 ps, suggest that the acoustic wave in W has a high frequency. Note that the diffraction signal is normalized such that the maximum value is 1. The maximum diffraction signal is observed at t=0 ps due to the electron dynamics. However, this peak is not visible in this graph as the graph has been re-scaled such that the diffraction signals due to the acoustic echoes are visible.

(a) (b)

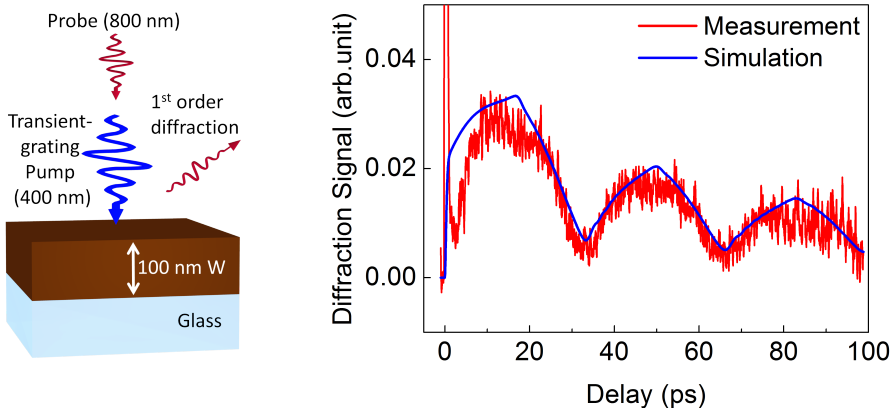

Figure 5.4: (a) Schematic of the experiment. (b) Transient-grating pump-probe measurement on a 100 nm thick tungsten (W) layer. The red curve shows the measured diffracted signal and the blue curve shows the calculated diffracted signal.

Using the literature value for the acoustic velocity in poly-crystalline tungsten, v=5.19 nm/ps (=5190 m/s) [38], and measuring the time interval between the acoustic echoes (32 ps), we calculate the thickness of the W layer to be 84 nm, which is reasonably close to the thickness we aimed to deposit (100 nm). The discrepancy could be due to the error in the thickness measurement of the W layer during the physical vapor deposition. The numerical simulation also predicts the shape of the diffracted signal, and the shape of the measured diffraction signal due to the acoustic echoes in W

is consistent with the observations made by A. Devos and C. Lerounge [38].

5.3.3 Acoustic waves in Au-SiO_x-Au samples

Anticipating later measurements on more complex layer stacks, we gradually increased the complexity of our samples. In this section, we show the results from the transient-grating measurements on multi-layer samples with a layer of SiO_x sandwiched between two Au layers, when pumped and probed from the air-Au side. In these experiments, we expect the SiO_x layer to act as a barrier for the diffusion of the hot electron gas energy from the top layer to the bottom layer. This, in turn, would confine the initial lattice heating only to the top layer, and hence the acoustic wave will be generated only in the top Au layer. The acoustic wave then propagates through the SiO_x to the bottom Au layer and returns to the top layer. The acoustic wave also undergoes partial reflection and transmission at the SiO_x-Au interface and Au-SiO_x interface, which results in multiple acoustic echoes.

In Figure 5.5 , we plot the measured diffraction signal from the two different samples. The first sample has a 60 nm Au layer on top of 7 nm SiO_x, on top of a 40 nm Au layer on a glass substrate (Figure 5.5 (a)). The second sample has a 60 nm Au layer on top of 7 nm SiO_x, on top of a 60 nm Au layer on a glass substrate (Figure 5.5 (b)). Both samples have the same thickness for the top Au layer. The measured diffracted signal of the first and the second sample are shown by the red and blue curve in Figure 5.5 (c). The red curve and blue curve have the same shape and strength until about 37 ps, after which they deviate. The rapid increase and the decrease of the diffraction signal during the first 10 ps is due to the electron dynamics in the 60 nm thick Au layer. The fact that both the curves have a very similar decay after the optical excitation means that hot electrons created in the top 60 nm layer of Au remain confined within that layer. The thin SiO_x layer acts as a barrier for electron energy diffusion. The acoustic wave generated in both the samples will have the same frequency and strength because they are generated in the top Au layer, which in both samples is 60 nm thick. The diffraction due to grating-shaped thermal expansion of the Au layer will also be the same for both samples. The acoustic wave generated in the homogeneously heated 60 nm thick Au layer partially reflects from the

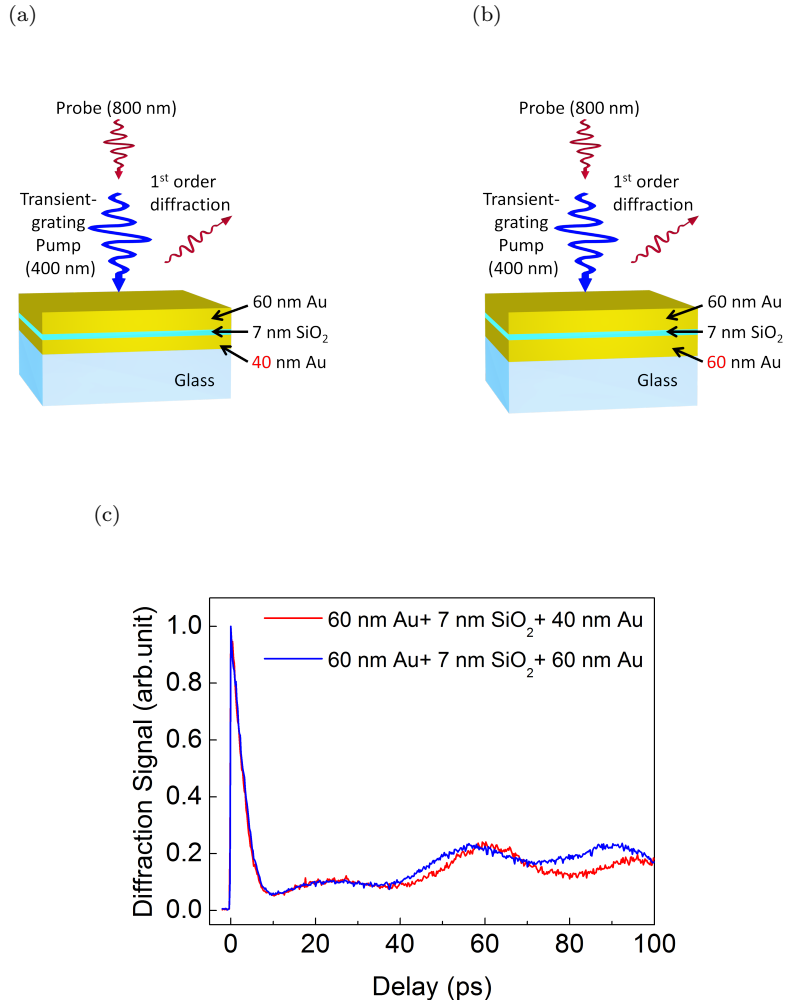

Figure 5.5: (a) and (b) Schematics of the transient-grating pump-probe experiments on samples with 7 nm SiO_x sandwiched between two Au layers. The top Au layer has the same thickness in both samples. (c) Measured diffracted signal as a function of pump-probe delay for the two samples.

Au-SiO_x interface and returns to the air-Au interface. This results in the trough in the recorded diffraction signal at 37 $\pm$1 ps. The large acoustic impedance mismatch between Au and SiO_x, results in significant reflection of the acoustic wave at the interface. The acoustic impedance of Au and SiO_x are 63.8 Ns/m^3 and 13.5 Ns/m^3, respectively. The position of the first

trough closely matches the calculated acoustic round trip time inside the 60 nm Au layer which is 37.5 ps. The acoustic wave partially transmitted at the Au-SiO_x interface, propagates through the SiO_x to the bottom Au layer, reflects from the Au-substrate interface and returns to the top surface. Since the thicknesses of the bottom layers are different, the shape of the measured diffraction signals after 37 ps is different. The difference is the shape of diffracted signals after 37 ps confirm that the acoustic wave has propagated beyond the SiO_x, and the acoustic wave had reflected from the Au-glass interface. The shape of the signals is complicated due to acoustic waves bouncing back and forth in the top Au layer, bottom Au layer, and the whole stack.

Next, we performed transient-grating pump-probe measurements on two different samples with a thin layer of SiO_x sandwiched between the Au layer. Here, the first sample has an 80 nm Au layer on top of 7 nm SiO_x, which is on top of a 40 nm Au layer on a glass substrate (schematically shown in Figure 5.6 (a)). The second sample has a 60 nm Au layer on top of 7 nm SiO_x, which is on top of a 60 nm Au layer on a glass substrate (schematically shown in Figure 5.6 (b)). In this case, the total thickness of the Au layer in both samples is the same. In Figure 5.6 (c), the red curve shows the diffraction signal from the first sample, and the blue curve shows the diffraction signal from the second sample.

The measured diffraction signal increases rapidly upon optical excitation and decays towards zero within the first 10 ps. We observe that the blue curve decays slower than the red curve. This observation is in agreement with the measurements shown in the previous chapter, where we observe a faster decay of the transient-grating signal for thicker Au layers. If the SiO_x did not act as an electron energy barrier, then we would have observed a very similar decay of the signal for both samples, as both samples have the same total thickness of Au. The fact that we see a different decay rate when the top layer thicknesses are different, and the same decay rate when the top layer thicknesses are the same, implies that the 7 nm thick SiO_x is an effective hot electron gas diffusion barrier.

The red and blue curves have different shapes after 10 ps. This difference arises from the fact that the arrival time of the first echo reflected from

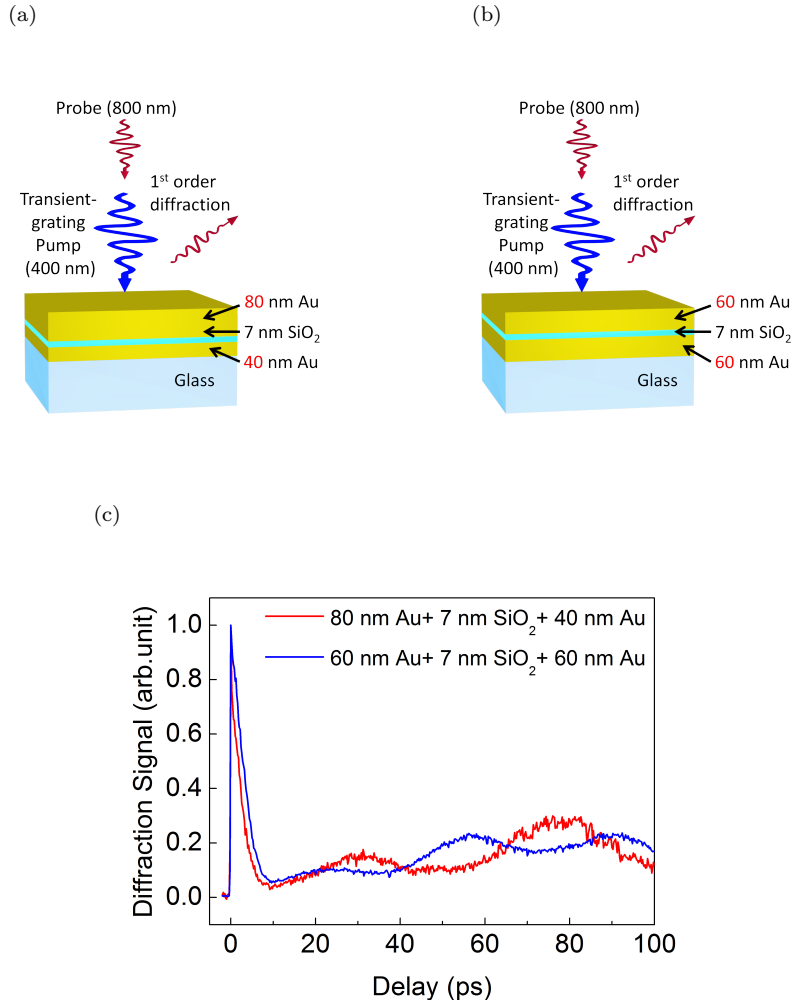

Figure 5.6: (a) and (b) Schematics of the transient-grating pump-probe experiments on samples with SiO_x sandwiched between two Au layers. The total thickness of Au in both samples is the same.(c) Measured diffracted signal as a function of pump-probe delay for the two samples.

the SiO_x layer is different. Also, the strength and spatial extent of the generated acoustic waves are different for both the samples. This can be explained by the difference in the thickness of the layer where the acoustic wave is generated. The two sets of measurements prove that we can launch an acoustic wave in a confined volume of Au, and the acoustic wave

can propagate through a multi-layer sample containing a dielectric layer. Complete numerical simulation of the diffraction signal for these Au-SiO_x-Au samples were not performed as the primary goal of these experiments were to understand electron energy diffusion and to check whether acoustic waves can propagate across a metal-dielectric interface.

5.4 Conclusion

We have shown that the transient-grating pump-probe setup can be used to launch and detect acoustic waves in flat Au, Ni, and W layers. We observe a background thermal grating, either due to thermal expansion of the layer or thermo-optic effect, on which the generated acoustic wave becomes visible as troughs when they arrive at the surface. Further support for this is found in experiments, where we pump from the air-metal side but probe from the substrate side. We also show that Ni can be used as an acoustic transducer to launch high-frequency acoustic waves in Au. Our experiments on samples that have a 7 nm thick layer of SiO_x sandwiched between two Au layers demonstrate that a thin layer SiO_x can be an effective electron energy diffusion barrier.

6

Detection of gratings buried underneath multi-layer dielectrics and metallic layers

In this chapter we report on the detection of gratings buried below a stack of tens of 18 nm thick SiO_2 and Si_3N_4 layers and an optically opaque metal layer, using laser-induced, extremely-high frequency ultrasound. In our experiments, the shape and amplitude of a buried metal grating is encoded on the spatial phase of the reflected acoustic wave. This grating-shaped acoustic echo from the buried grating is detected by diffraction of a delayed probe pulse. The shape and strength of the time-dependent diffraction signal can be accurately predicted using a 2D numerical model. Surprisingly, our numerical calculations show that the diffracted signal strength is not strongly influenced by the number of dielectric layers through which the acoustic wave has to propagate.

Parts of this chapter are contained in a manuscript accept for publication in Phys. Rev. Appl. (2020). Preprint at arXiv:1911.08337 [123].

6.1 Introduction

Wafer alignment in a nanolithography machine is dependent on the ability to detect specific grating targets that have been placed at multiple sites on a wafer. These gratings targets, also called alignment gratings, are etched into Si wafers in scribe lanes between the various dies on the wafer. As modern chip architectures are becoming increasingly three-dimensional, these alignment gratings can become hidden under opaque layers. For example, in a 3D NAND memory chip, the alignment gratings etched on the Si wafer can become buried below a large number of dielectric and/or metallic layers deposited during chip fabrication. There, typically the dielectric layers are oxides and nitrides, and the opaque layer can be dielectric or metallic. This poses a huge challenge for the detection of alignment gratings, in particular because some of these layers are entirely opaque to light. Fortunately, layers that are opaque to light are often transparent to sound and, therefore, using laser-induced ultrasound could be a novel and appealing way to detect gratings buried underneath these layers. The challenge, however, is not only to detect gratings underneath opaque layers with these extremely-high-frequency sound waves. The challenge is also to do this through complex multi-layered systems that can be found in state-of-the-art semiconductor devices [17].

In this chapter, we show how we can detect buried gratings underneath optically opaque layers, by measuring transient optical diffraction from ultrafast, laser-induced, extremely high-frequency acoustic copies of the grating. In our proof-of-principle experiment we first fabricate metal gratings on top of a single metal layer deposited on a glass substrate. When viewed from the glass side, the gratings are essentially invisible and can be considered "buried". We performed femtosecond pump-probe experiments with 400 nm wavelength pump and 800 nm wavelength probe from a Ti:Sapphire amplifier. As illustrated in Figure 6.1, an optical pump-pulse excites the metal through the substrate and launches an acoustic wave which propagates through the opaque layer, then reflects off the peaks and valleys of the grating and thus acquires a spatially periodic phase. This wave returns to the glass-metal interface where it deforms the interface in a spatially periodic manner. This interface grating can be detected by diffraction of a

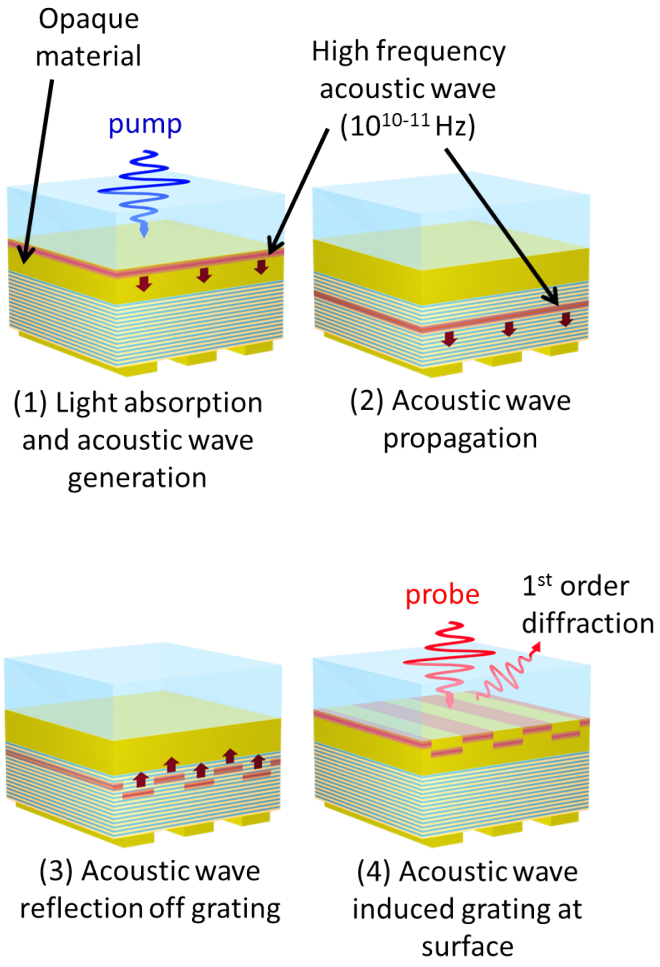

Figure 6.1: Schematic explaining the technique. The femtosecond laser pulse is absorbed by the material at the substrate-material interface (1), launches an acoustic wave that propagates through different layers (2). The acoustic wave reflects off the buried grating and returns to the substrate-material interface as a grating-shaped acoustic wave (3). The time-delayed femtosecond probe pulse diffracts off this interface grating, and the first-order diffraction signal is recorded (4).

time-delayed probe-pulse. Our measurements show that on simple systems consisting of 10 nm amplitude buried gratings underneath thick gold (Au) or nickel (Ni) layers, diffraction is easily detected. A comparison with calculations shows that grating-like deformation at the glass-metal interface

induced by the acoustic echo, has an amplitude of several tens of picometers. Remarkably, we also observe diffraction at the glass-metal interface on more complex systems consisting of 10 nm amplitude gratings fabricated on top of 5 or 10 bilayers of thin silicon dioxide (SiO_2) and silicon nitride (Si_3N_4) layers on top of a Au or Ni layer on glass. For the sample with 10 bilayers of SiO_2 and Si_3N_4 layers, after being generated, the acoustic wave has to travel through 42 layers in total before the acoustic echo reaches the glass-metal interface again where it is detected by diffraction of the optical probe pulse. Surprisingly, we find that the diffraction signal strength is not strongly influenced by the number of layers in the stack. This is confirmed by numerical calculations showing that replacing the SiO_2/Si_3N_4 stack with a single layer having an equivalent time-averaged sound velocity and average density, has only a small effect on the shape and amplitude of the diffracted signal as a function of time. The calculations demonstrate that the complex shape of the time-dependent diffracted signal is predominantly influenced by reflections of the acoustic wave at the glass-metal and the metal-stack interfaces. Our results show that buried gratings can be detected through optically opaque layers on complex, multi-layered samples, using laser-induced, extremely high-frequency ultrasound. This technique shows promise as a new, non-contact, all-optical grating detection- and imaging-modality for wafer alignment applications by using ultrasound to make an acoustic copy of the buried grating, while using conventional optical diffraction to read-out the copy when it reaches the surface.

6.2 Experimental setup

A schematic of the pump-probe setup used for the experiments is shown in Figure 7.2. A Ti:Sapphire multi-pass amplifier generates 30 fs pulses with a repetition rate of 1 kHz and with a wavelength centered at 800 nm. The output from the laser is split into two by a 95/5 beamsplitter. A 100 µm BBO crystal frequency-doubles the stronger beam to generate 400 nm pump pulses. The weaker part off the 800 nm beam is used as a probe. A half-wave plate (HWP) rotates the polarization of the 400 nm pump pulse by 90° so that both the pump and the probe are p-polarized. Both the pump and probe are weakly focused onto the sample such that the pump beam diameter is about 500 µm and pump pulse energy ranges from 6 µJ to 8 µJ

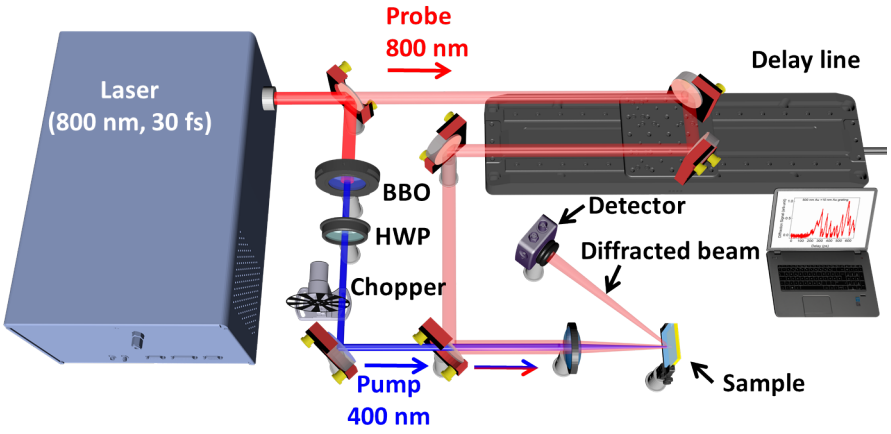

Figure 6.2: Schematic of the experimental setup. 30 fs pulses with a wavelength of 800 nm are split into pump and probe beams. The pump is frequency-doubled in a BBO crystal, passes through a half-wave plate (HWP) and is focused onto the sample with a lens. The 800 nm probe beam passes through a variable optical delay line and is focused onto the sample on the same spot as the pump beam. An optical detector measures the first-order diffracted probe beam.

depending on the sample. The probe beam diameter is 250 µm and the probe pulse energy was kept constant at 2 µJ. A silicon photo-detector is placed at the position where the first-order diffracted probe beam from the buried grating is expected. The signal recorded by the detector when the chopper blocks the pump beam is subtracted from the diffracted probe signal when the pump beam is transmitted by the chopper, and plotted as a function of the pump-probe delay.

6.2.1 Sample fabrication

In principle, buried gratings can be made by chemically etching gratings in Si, followed by the deposition of dielectric and/or metallic layers. The resulting sample, however, then shows a strong surface topography which follows the topography of the buried grating even though it is not a true copy of it. When real semiconductor devices are manufactured, repeated steps involving deposition of layers followed by polishing are carried out, ultimately reducing or eliminating the residual surface topography. Making samples with zero surface topography turned out to be impossible using our

clean-room facilities. To test whether laser induced ultrasonics is capable of detecting buried gratings, we therefore opted to make samples by first depositing nominally flat dielectric/metallic layers on glass followed by the fabrication of a grating on top of this. By now performing pump-probe diffraction measurements from the glass side, the grating is invisible to both pump and probe and can be viewed as a buried grating. All the samples were prepared on 175 µm thick, chemically cleaned glass substrates. The Au and Ni layers were fabricated by physical vapor deposition, and the thickness was determined by a quartz crystal thickness monitor. The gratings on top of the metal/dielectric layers were fabricated by UV lithography. All gratings discussed in this chapter have a pitch of 6 µm. The SiO_2 and Si_3N_4 layers were deposited by sputtering, using a silicon target in the presence of oxygen and nitrogen, respectively. To calibrate the thickness of the SiO_2 and Si_3N_4 layers, we performed linear spectroscopy measurements on single layers of SiO_2, and Si_3N_4 deposited on Si, under the same conditions.

6.3 Results and discussion

6.3.1 Grating under flat metal layer

To get an estimate of the nature and strength of the diffracted signal from the acoustic echo of the buried grating, we first perform femtosecond, time-resolved experiments on relatively simple systems, consisting of (i) a 10 nm amplitude 50 % duty cycle Au grating on a 522 nm flat Au layer deposited on glass (Figure 6.3 (a)) and, (ii) a 10 nm amplitude, 50 % duty cycle Ni grating on a 315 nm flat Ni layer deposited on glass (Figure 6.3 (b)). Au is rarely used in the semiconductor manufacturing industry, and our choice for Au as the grating/layer material is exclusively motivated by the fact that Au is one of the most well-studied materials. However, it has a relatively small electron-phonon coupling constant compared to that of Ni, and we expect this to have a significant impact on the shape of the resulting acoustic signals [21, 84]. All pump-probe measurements discussed in this paper were performed from the substrate side. As the gratings are fabricated at the metal-air side and are thus optically hidden from the pump and probe pulses (see Figure 6.3 (a) and (b)), the gratings can be

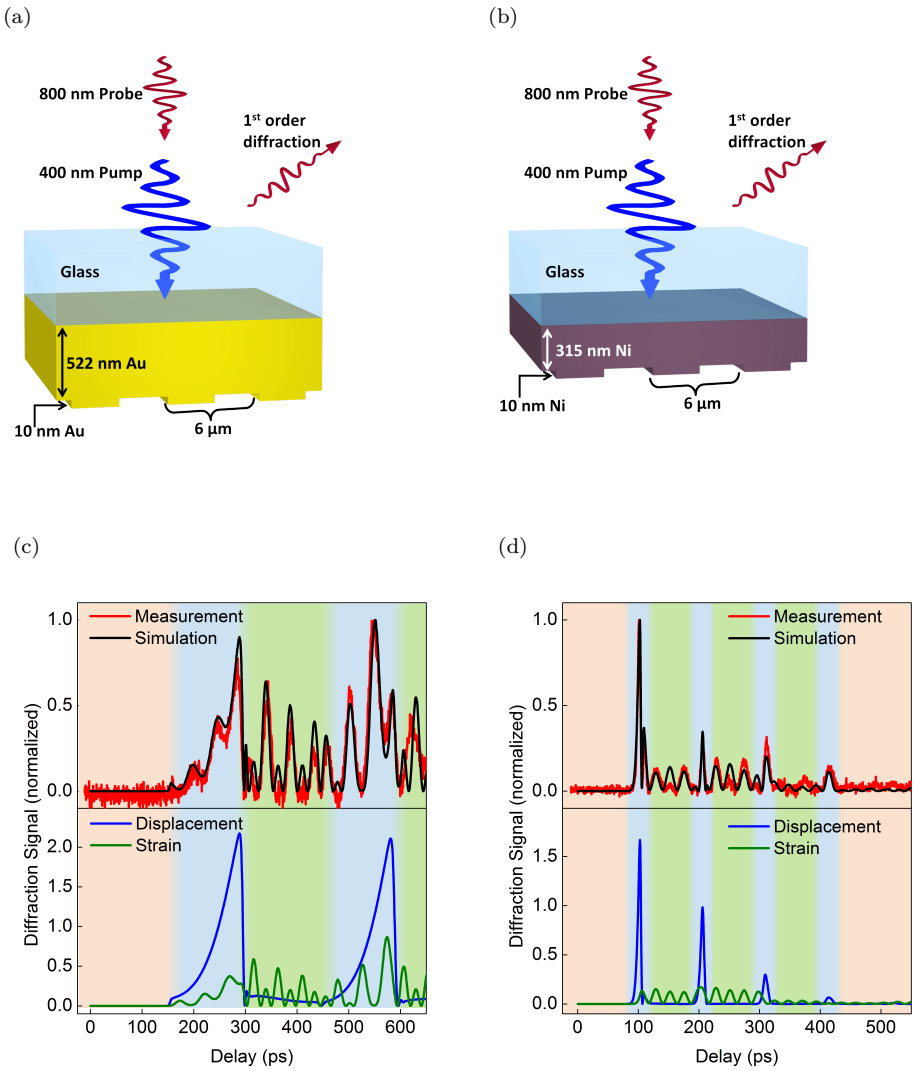

Figure 6.3: (Caption on the following page)

Figure 6.3: Schematics of the beam/sample geometry for: (a) the 10 nm amplitude Au grating on a 522 nm Au layer on glass and (b) 10 nm amplitude Ni grating on a 315 nm Ni on glass. Both gratings have a 50 % duty-cycle. The pump pulse has a wavelength of 400 nm and the probe pulse has a wavelength of 800 nm. (c) Upper panel: The experimentally measured (red) and numerically simulated (black) diffracted probe signal vs. pump-probe delay for the Au on Au grating sample. Bottom panel: Calculated probe diffraction signal vs. pump-probe delay taking only the displacement of the glass-Au interface into account (blue line), or taking only the propagating strain pulse in the glass substrate into account (green line). (d) Upper panel: The experimentally measured (red) and numerically simulated (black) diffracted probe signal vs. pump-probe delay for the Ni on Ni grating sample. Bottom panel: Calculated probe diffraction signal vs. pump-probe delay taking only the displacement of the glass-Ni interface into account (blue line), and taking only the propagating strain pulse in the glass substrate into account (green line).

considered "buried".

In Figure 6.3 (c), we plot the measured first-order diffracted signal (red curve) as a function of the pump-probe delay for the sample consisting of a 10 nm amplitude Au grating on a 522 nm flat Au layer on glass. The graph shows that for the first 150±2 ps after optical excitation, there is no diffracted signal. After this, a diffraction signal emerges that slowly rises to a maximum at a delay of around 280±2 ps. A second maximum can be seen around delay values of about 560 ps. Superimposed on these is a more rapidly oscillating signal with a period of 47±2 ps. Note that the signature of this more rapid oscillation is already present on the rising edge of the first main diffraction peak but also on the falling edge of the second main diffraction peak.

We want to point out that the very observation of diffraction after 150 ps implies the presence of a grating at the glass-Au interface. This grating is caused by the returning acoustic wave whose wavefront has the topography of the buried grating imprinted on it through a spatially periodic delay in the acoustic arrival time, or phase. In principle, the nature of this grating is a displacement of the atoms at the glass-Au interface. For other materials, spatially periodic changes in the optical constants of the materials, caused by changes in material density induced by the sound wave, can also contribute. As we will show later, for Au, our calculations indi-

cate that displacement of the atoms at the glass-Au interface leading to a grating with an amplitude of up to 110 pm at the glass-Au interface is the dominant cause of diffraction. Regardless, our measurements show that we can observe the presence of an optically hidden, 10 nm amplitude, grating through diffraction from an acoustic "copy" of the grating.

To properly understand these measurements we first focus on the acoustic wave generation mechanism in Au. The 400 nm pump pulse is absorbed within the optical penetration depth of about 16 nm in Au, creating a hot electron gas [21, 46, 85]. The electron-gas energy rapidly diffuses deeper into the thick Au layer to a maximum depth of several hundred nanometers. Such a large diffusion depth is possible because Au has a relatively small electron-phonon coupling strength [64, 84]. On a time scale of a few picoseconds, the electron gas cools by heating the lattice. The highest lattice temperatures are found near the glass-Au interface, where the light is absorbed. The rapid heating of the lattice leads to a rapid expansion of the lattice which launches a longitudinal acoustic pulse with a spatial extent corresponding to the electron energy diffusion depth. The slow, early rise of the diffraction signal versus time is due to the arrival of part of the acoustic wave that has been generated deep inside the Au layer and thus is the earliest to reflect off the buried grating. The diffraction signal continues to slowly increase up to 280±2 ps at which time the part of the acoustic wave that was generated near the glass-Au interface returns to the interface again after reflecting off the buried grating. A second, broad diffraction signal is seen around 550-580 ps which is the arrival of the same acoustic wave after the second round trip.

The rapid, lower amplitude oscillation superimposed on the signal is surprising, considering that its period doesn't match the round trip propagation time in 522 nm Au. We attribute this oscillation to Brillouin scattering from the part of the acoustic wave that has entered the glass and continues to propagate [124–128]. The wavefront of this acoustic wave is still spatially periodic, modifies the refractive index of the glass, and gives rise to probe pulse diffraction (see Figure 6.4). Normally, the presence of such a quasi-static grating in glass would give rise to a constant (in time) diffracted signal. Here, however, the same probe pulse that diffracts off this grating also reflects from the glass-Au interface and then diffracts off

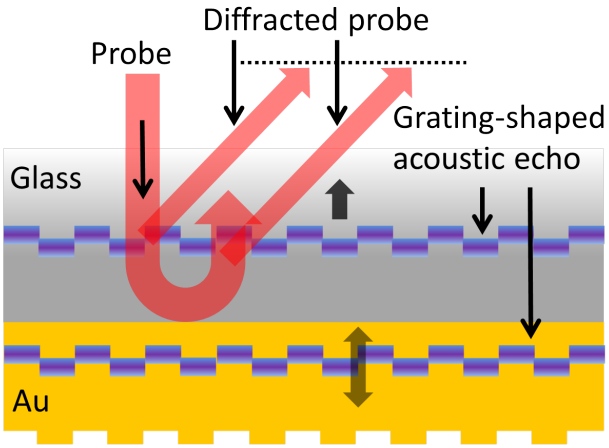

Figure 6.4: Schematic showing the interference of the two diffracted probe pulses leading to Brillouin scattering in the glass.

the grating in the same direction again [126]. The extra optical phase acquired by the propagation of the optical pulse before it diffracts a second time leads to interference between the electric fields of the diffracted beams. Whether the interference is constructive or destructive depends on the distance that the optical pulse has propagated before diffracting again. This in turn depends on the distance that the acoustic wave in the glass has travelled from the glass-Au interface and is thus a periodic function of time. It can be shown [124–128] that the period of this oscillation is given by $T = \lambda/(2nv\cos(\theta))$. Here λ is the probe wavelength, n is the refractive index of glass, v is the sound velocity in glass, and θ is the angle of incidence. In our experiments we have λ= 800 nm, n=1.5, v= 5,700 m/s and $\cos(\theta) \approx 1$, giving an oscillation period of 46.7 ps which matches the period observed in the measurements. The Brillouin scattering in glass dominates the time-dependent diffraction signal we observe between 300 ps and 450 ps. The diffraction peak at 283±2 ps is from the first round trip of the acoustic wave, and the peak at 580±2 is from the second round trip of the acoustic wave in 522 nm Au. As the acoustic wave travels back and forth in the Au layer, every time it reaches the glass-Au interface, part of the wave will be transmitted into the glass. The diffraction signal we observe after 450 ps therefore is a coherent sum of diffracted signals from multiple contributions, namely (i) light diffracting from the grating-shaped acoustic

echo in Au when it is close to the glass-Au interface after the second round trip, (ii) light diffracting due to Brillouin scattering in glass from the acoustic wave grating that entered the glass after the first round trip and, (iii) light diffracting due to Brillouin scattering in glass from the acoustic wave that entered the glass after the second round trip. Interference between the light beams diffracted off these gratings makes it difficult to predict what the temporal shape of the diffracted signal will look like. As we will show below, we therefore resorted to 2D numerical calculations of the generation, propagation, diffraction, and optical detection of the acoustic waves, which take into account all the aforementioned contributions.

Finally, we note that shortly after optical excitation with a pump beam, the abrupt surface expansion of the metal layer also generates an acoustic wave which propagates into the glass. However, this acoustic wave does not result in the diffraction of the probe pulse, as its wavefront has not reflected off the grating and is, thus, "flat".

Now that we understand the factors that contribute to the diffraction signal, we performed numerical simulations to show how these factors affect the shape and time evolution of the diffraction signal. The simulations are based on a numerical model we developed which solves a set of equations by the 2D finite-difference time-domain method. Those equations describe the generation, propagation and optical detection of the acoustic waves. The model includes diffraction caused by the displacement of the surface at the glass-Au interface, diffraction by possible changes in the complex refractive index in the metal, and diffraction of light by the refractive index grating formed by the acoustic waves in the glass. The model is briefly explained in the earlier section and details of the model can be found elsewhere [18]. In Figure 6.3 (c) (upper panel), we plot the numerically simulated diffraction signal as a function of the pump-probe delay for the 10 nm amplitude grating on 522 nm Au on glass (black curve). The simulation is in good agreement with the experimentally measured diffraction signal, as it predicts both the position and the relative intensities of the diffraction peaks. The bottom panel in the same figure shows the contributions to the calculated diffraction signal due to the (i) displacement of the atoms near the glass-metal interface caused by the acoustic wave propagating in the Au layer (blue curve), (ii) changes in the optical constants of the glass due to

the strain-optic effect, or Brillouin scattering, in the glass substrate (green curve). Note that the full calculations (black curve) cannot simply be obtained by adding the curves calculated for the strain contribution (green curve), to that for the curve calculated for surface atom displacement only (blue curve). The reason for this is that the phases of the diffracted light scattered by the two types of gratings have to be taken into account as well. This can give rise to destructive interference and thus a net diffracted signal that is smaller than the simple sum of the intensities of the diffracted beams obtained for each grating separately. The model calculates the diffracted optical field, thus those coherent additions are fully taken into account.

To study the effect that the electron-phonon coupling strength has on the shape of the acoustic signal reflected off the buried grating, we also performed measurement on a 10 nm amplitude Ni grating fabricated on a flat 315 nm thick Ni layer on glass (Figure 6.3 (b)). The electron-phonon coupling constant in Ni is about 12 times larger than that of Au (see Table 6.1). In Figure 6.3 (d) we plot the measured first-order diffracted signal as a function of the pump-probe delay for this sample (red curve). The diffraction signal stays zero for the first 100 ps after optical excitation, after which it rises sharply within 5 ps and quickly drops to zero, in contrast to the results shown for Au where the signal increases more slowly. In Ni, the hot electron gas formed after optical excitation cools much more rapidly and heats the lattice before the hot electron gas energy can diffuse much deeper into the layer. This rapid heating within a limited depth of ≈ 75 nm results in the generation of a much higher frequency longitudinal acoustic wave. This acoustic wave is much more localized in the propagation direction than in the case of Au and thus gives rise to more narrow peaks in the diffraction signals. The diffraction peaks we observe at 102 ± 2 ps, 205 ± 2 ps, 310 ± 2 ps, and 415 ± 2 ps are due to diffraction of the probe pulse after the 1^{st}, the 2^{nd}, the 3^{rd} and the 4^{th} round trip of the acoustic echo that originated at the glass-Ni interface, respectively.

One noticeable feature in these measurements is the very sharp decrease of the diffraction signal at 102 ps, immediately after the first main diffraction peak. The sharp dip can be understood from the shape of the wavefront of the acoustic wave after it reflects off the buried grating. The part of the wave that reflects off the valleys of the grating takes ≈ 3.5 ps longer

to return to the glass-Ni interface than the part that reflects off the peaks of the grating. In fact, we can view the two parts as two separate time-delayed gratings, shifted by half-a-grating-period, equivalent to a π phase shift, in the direction parallel to the grating vector. When both gratings are close to the interface, within the region that corresponds to the optical penetration depth of the probe pulse, the probe can diffract off both gratings simultaneously. However, a π phase difference between the two gratings implies a π phase difference between the electric fields diffracted off the two gratings. Therefore, soon after the arrival of the first acoustic grating, the second acoustic grating arrives, and the field diffracted off this grating destructively interferes with that diffracted off the first. This leads to a very sharp dip in the diffracted intensity immediately after the first diffraction peak.

Between 110 ps and 190 ps, we observe diffraction peaks caused by Brillouin scattering in the glass substrate. In contrast to the measurement on the Au sample described above, Brillouin scattering oscillation is not observed on the rising edge of the diffracted signal from the first acoustic echo in the Ni layer. This is because the rise time of the acoustic wave amplitude is simply too short. By the time the acoustic wave arrives near the glass-Ni interface and is partially transmitted by it, the acoustic wave in the glass has not propagated far enough to observe the oscillation. This is different for the Au case where the acoustic wave is much longer. After about 115 ps, the acoustic echo is no longer present at the glass-Ni interface, and the small diffraction peaks at 130 ps and 176 ps are only due to Brillouin scattering in the glass. The separation between these peaks is 46$\pm$1 ps which is the Brillouin oscillation period in glass for the probe wavelength. Similarly, after the second round trip of the acoustic wave in Ni at 205 ps, we observe small diffraction peaks separated by 46 ps at 230$\pm$2 ps and 276$\pm$2 ps which are also due to the Brillouin scattering. The short duration of the acoustic wave in Ni enables us to more easily separate the Brillouin scattering effect in the glass from that of the acoustic wave in the metal. We observe that the width (FWHM) of the diffraction peaks due to the acoustic wave in Ni at 102 ps, 205 ps, 310 ps, and 415 ps, is 5$\pm$1 ps, 7$\pm$1 ps, 9$\pm$1 ps, and 13$\pm$1 ps respectively. This gradual increase in the FWHM of the diffraction signal after each round trip is suggestive of dispersion of the acoustic wave.

However, the presence of the oscillations caused by Brillouin scattering makes it difficult to ascertain whether this is the only factor contributing to the increase in the FWHM. No measurable diffraction by the acoustic wave propagating in Ni is observed after 450 ps. The main reason for this is that the acoustic wave undergoes damping as it propagates inside the Ni layer and because of partial transmission of the acoustic wave into the glass at the glass-Ni interface upon every round trip.

In Figure 6.3 (d) (upper panel), we plot the numerically calculated diffraction signal (black curve) along with the measured diffraction signal for the Ni sample. In Figure 6.3 (d) (lower panel), we plot the diffraction signals due to (i) the displacement of the atoms near the glass-Ni interface (blue curve) and (ii) Brillouin scattering in the glass substrate (green curve). Here too, the calculated diffraction signal that takes both surface displacement and Brillouin scattering into account (black curve), is very similar to the measured one. These calculations allow us to unambiguously attribute the largest diffraction peaks at 102 ps, 205 ps, 310 ps and 415 ps to scattering off the spatially periodic displacement of the atoms at the glass-Ni interface after each round trip of the acoustic wave inside the Ni layer. The lower amplitude diffraction peaks observed in between are clearly caused by Brillouin scattering in the glass. Note that the calculations also show hints of broadening of the diffracted peaks when only the interface displacement is taken into account. This again is suggestive of peak broadening by acoustic wave dispersion.

6.3.2 Complex multilayer samples

Now that we understand the experiments performed on buried gratings deposited on single Au and Ni layers, we next performed measurements on more realistic and, thus, more complex samples. In real-life semiconductor device manufacturing, alignment gratings are often etched in narrow scribe lanes between individual chips on a wafer. No devices are fabricated in these lanes, but the gratings get covered by the deposited opaque materials nonetheless. For example, manufacturing 3D NAND memory chips requires detection of alignment grating through thick opaque metal/dielectric layer and many alternating layers of silicon oxide and silicon nitride [17]. The samples we fabricated consist of layers of materials that partially mimic the

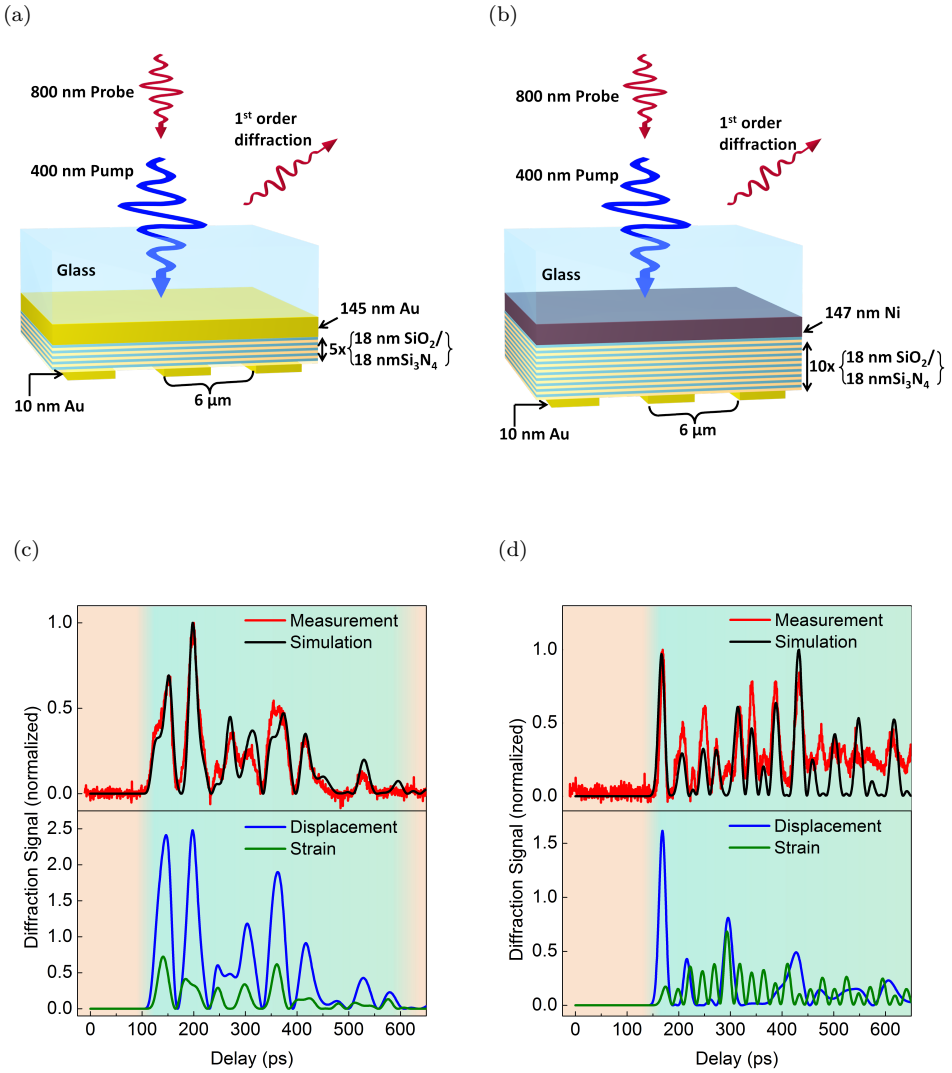

Figure 6.5: (Caption on the following page)

Figure 6.5: Schematics of the beam/sample geometry for: (a) the 10 nm amplitude Au grating on 5 pairs of alternating layers of 18 nm SiO_2 and 18 nm Si_3N_4 fabricated on a 145 nm thick Au layer on glass ("Au-multilayer"), (b) the 10 nm amplitude Au grating on 10 pairs of alternating layers of 18 nm SiO_2 and 18 nm Si_3N_4 , fabricated on top of a 147 nm thick Ni layer on glass ("Ni-multilayer"). (c) Upper panel: The experimentally measured (red) and numerically simulated (black) diffracted probe signal vs. pump-probe delay for the "Au-multilayer" sample. Bottom panel: Calculated probe diffraction signal vs. pump-probe delay taking only the displacement of the glass-Au interface into account (blue line), and taking only the propagating strain pulse in the glass substrate into account (green line). (d) Upper panel: The experimentally measured (red) and numerically simulated (black) diffracted probe signal vs. pump-probe delay for the "Ni-multilayer" sample. Bottom panel: Calculated probe diffraction signal vs. pump-probe delay taking only the displacement of the glass-Ni interface into account (blue line), and taking only the propagating strain pulse in the glass substrate into account (green line).

materials/structure used in the fabrication of 3D NAND memory. However, for comparison with the results shown for single layers, we used Au and Ni as the grating material and as the layer in which the sound waves are generated.

For the first sample, which will henceforth be referred to as the "Au-multilayer" sample, we evaporated 145 nm of Au on glass, on top of which we deposited five alternating pairs of 18 nm thick SiO_2 and 18 nm thick Si_3N_4. On top of this stack we fabricated a 10 nm amplitude Au grating, as shown in Figure 6.5 (a). For the second sample, which will henceforth be referred to as the "Ni-multilayer" sample, we first deposited a 147 nm thick layer of Ni followed by the deposition of ten pairs of 18 nm thick SiO_2/18 nm thick Si_3N_4 layers. On top of this, a 10 nm amplitude Au grating was fabricated. In this case, the SiO_2/Si_3N_4 stack consists of 20 layers in total and is thus twice as thick as the stack in the first sample. This sample is schematically shown in 2(b). The thickness of the SiO_2 and Si_3N_4 layers was calibrated by linear spectroscopy measurements.

In Figure 6.5 (c) we show the measured diffraction signal as a function of the pump-probe delay (red curve), for the "Au-multilayer" sample. The diffraction signal remains zero for about 100 ps, after which the first diffraction peak is observed, followed by a quasi-periodic oscillating signal. We emphasize that the time-dependent diffraction signal we observe in our

measurements is proof that we detect the presence of a "buried" grating, by measuring optical diffraction off an acoustic copy of the grating near the glass-metal interface. This means that, in spite of the many interfaces encountered by the propagating acoustic wave, a well-defined acoustic copy of the buried grating can still be detected near the glass-Au interface. Remarkably, the energy of the acoustic wave has not completely dissipated as it propagates through these layers. Similar to the measurements on the grating fabricated on a single layer of Au, the individual peaks are fairly broad. Again, this is caused by the relative homogeneous heating of the Au layer by rapid diffusion of the electron gas energy into the metal layer. As in the previous measurements, the signal we measure is the coherent sum of the optical fields diffracted off the grating-shaped acoustic wave at the Au-glass interface and off the grating-shaped acoustic wave in the glass.

To better understand the measurement, we performed a numerical simulation of the diffracted signal versus time delay, which is shown in Figure 6.5 (c), upper panel (black curve). We see a remarkable agreement between the measured and the simulated curves for this complex multilayer sample, indicating that the model contains all the physics necessary to predict the salient features of our measurements. In the bottom panel we plot the calculated diffracted field taking only the displacement of the glass-Au interface by the acoustic wave into account (blue curve) and the diffracted field calculated taking only the changes in the optical constants of the glass due to the strain-optic effect, or Brillouin scattering, into account (green curve). For the "Au-multilayer" sample, the first peak for the displacement contribution (blue curve) is at 146 ps, which corresponds to the acoustic round trip time for the whole stack of dielectric layers.

In Figure 6.5 (d) we plot the measured diffraction signal as a function of the pump-probe delay (red curve), for the "Ni-multilayer" sample. The diffraction signal remains zero for about 155 ps, then begins to increase until a first maximum is observed at 169±2 ps. This diffraction signal is due to the acoustic wave returning to the glass-Ni interface after one round trip through the whole stack of layers. This arrival time matches the expected propagation time through all the layers (see Table 6.2). The diffraction signal then drops to zero and quasi-periodic oscillations are observed. Note that here too the diffraction peaks are "sharper" than for the

"Au-multilayer" sample, in a manner similar to what is observed for the single layer samples. Again, this can be explained by the larger electron-phonon coupling constant of Ni, which leads to shorter acoustic waves. The signal we observe after 169 ps has contributions from the interference of optical fields diffracted off acoustic waves near the glass-Ni interface, and off acoustic wave transmitted into the glass substrate. To better understand the measurement, we performed a numerical simulation of the diffracted signal, which is shown in Figure 6.5 (d), (black curve). The position of the peaks in the simulated curve agrees well with the position of the peaks in the measurement. The amplitudes are seen to match less well. The blue curve in the bottom panel in the figure shows the calculated diffracted field taking only the displacement of the glass-Ni interface into account, and the green curve shows the diffracted field calculated taking only the Brillouin scattering in glass into account. The first peak seen in the calculation of the diffracted signal caused by only the displacement, at 169 ps, is due to the return of the first acoustic wave reflected off the buried grating after propagating through all the layers. This grating-shaped acoustic wave, now at the glass-Ni interface, undergoes another reflection inside the 147 nm Ni layer before it returns to the glass-Ni interface again where it gives rise to the second peak at 215 ps. The periodic oscillations due to Brillouin scattering in the glass substrate can be seen more clearly in the "Ni-multilayer" sample as compared to the "Au-multilayer" sample, because of the shorter length of the acoustic wave. Our measurement on the "Ni-multilayer" sample demonstrates that we can detect the acoustic wave even after it has propagated back and forth through 20 dielectric, so through 40 layers in total.

6.3.3 Effective acoustic properties of the bilayer dielectric stack

To understand how the SiO_2 and Si_3N_4 bilayers affect the strength and shape of the diffraction signal, we performed numerical simulations where we replaced the dielectric bilayers with a single equivalent acoustic medium [129]. We replaced the dielectric layers with a single medium that has the same thickness as the SiO_2/Si_3N_4 stack and has a density which is the average density of SiO_2 and Si_3N_4. The acoustic velocity of the equivalent

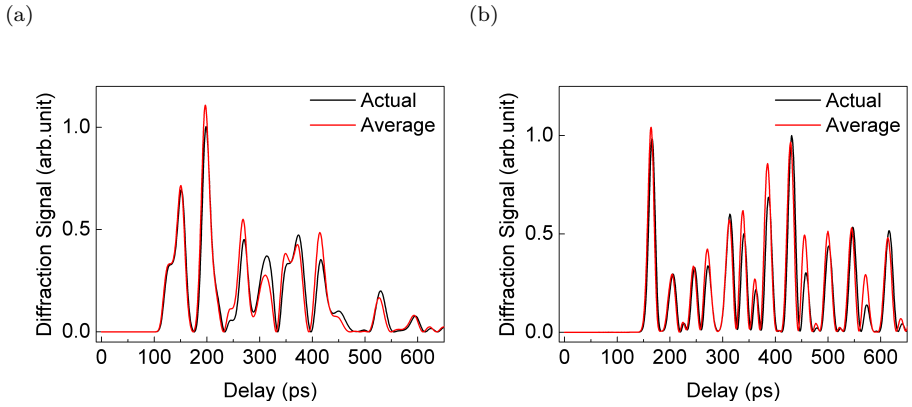

Figure 6.6: (a) Calculated diffraction signal vs. pump-probe delay for the "Au-multilayer" sample. The black curve is a calculation that takes all pairs of alternating layers of 18 nm SiO_2 and 18 nm Si_3N_4 into account. The red curve is a calculation in which the all pairs of alternating layers have been replaced with a single layer having the same total thickness but with average acoustic properties. (b) Similar to (a) but now for the "Ni-multilayer" sample.

medium is calculated such that the time for the acoustic wave to propagate through the single equivalent medium is the same as the time required to propagate through all the dielectric layers. Hence the velocity of the equivalent time-average medium (V_{ta}) is given by

$$\frac{1}{V_{ta}} = \frac{1}{d_1 + d_2}\left(\frac{d_1}{v_1} + \frac{d_2}{v_2}\right), \tag{6.1}$$

where v_1 and v_2 are the acoustic velocities in SiO_2 and Si_3N_4, respectively and d_1 and d_2 are the thickness of SiO_2 and Si_3N_4, respectively. In Figure 6.6 (a) we show the calculated time-dependent diffraction signal for the "Au-multilayer" sample (black curve), together with the diffraction signal calculated when the 10 dielectric layers are replaced with the single equivalent time-average medium of the same thickness (red curve). Similarly, in Figure 6.6 (b) we show the calculated time-dependent diffraction signal for the "Ni-multilayer" sample (black curve) and the calculated diffraction signal when the 20 dielectric layers are replaced with the single equivalent medium of the same thickness (red curve). For both samples, although there are some differences between the calculated curves, the signal shapes are remarkably similar, as are the amplitudes of the signals. Minor differ-

ences are mostly seen at long time delays. The *position* of the first acoustic diffraction peak is not expected to change when the bilayer is replaced with an equivalent acoustic medium because the time it takes for one round trip inside the whole layer remains the same. However, surprisingly, the partial reflections and transmission at the bilayer interfaces don't change the shape of the time-dependent diffraction signal significantly. This is partially explained by the length of the acoustic wave, which is much greater than the thickness of the individual dielectric layers. The acoustic wave only "sees" an equivalent medium rather than the individual layers. However, the modest acoustic impedance mismatch between the SiO_2 and Si_3N_4 also plays a role here (see Table 6.2), and both effects must be taken into account to understand these results. We note that similar effects have been predicted for the propagation of low-frequency sound waves in seismology [129]. This suggests that laser-induced ultrasonics can be used to detect buried gratings when the number of dielectric layers is further increased to values often encountered in the semiconductor manufacturing industry.

6.3.4 Optical excitation of Au and Ni layers

To gain some insight into the longitudinal spatial extent of the acoustic wave generated after optical excitation, we have used the TTM to calculate the lattice temperature as a function of depth inside the metal layer, 15 ps after optical excitation with the pump pulse. At this time the TTM shows that the hot electron gas has significantly cooled and is in local thermal equilibrium with the lattice. In Figure 6.7 (a), we show the resulting lattice temperature as a function of depth for the 522 nm Au sample. The figure shows the large penetration depth of energy into the metal, which can be explained by the relatively weak electron-phonon coupling strength of Au. It is the rapid heating of the lattice that launches the acoustic wave, which, in this case, has a relatively long wavelength. Note that a significant lattice temperature increase is observed even at a depth of 522 nm.

In Figure 6.7 (b), we show the calculated lattice temperature as a function of depth inside the 315 nm thick Ni layer. In contrast to that of Au, the lattice temperature is limited to a smaller depth of about 75 nm, resulting in a higher local temperature and an acoustic wave with a shorter wavelength. The short wavelength of the acoustic wave manifests itself in our measure-

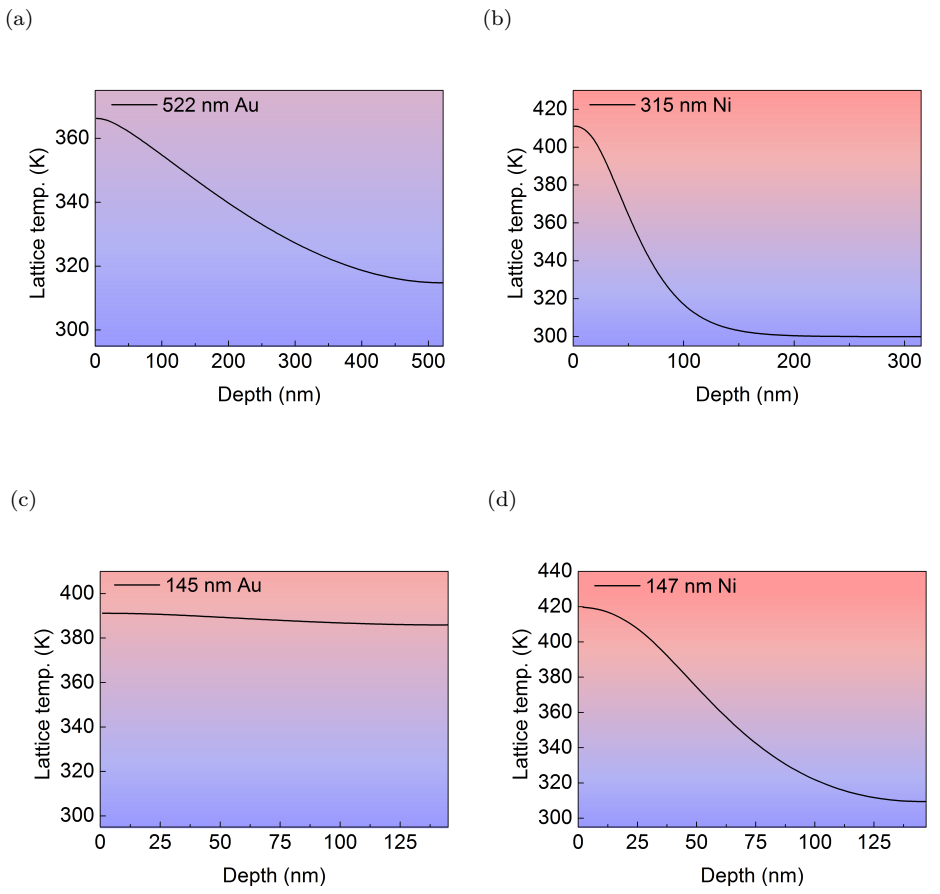

Figure 6.7: Lattice temperature inside the metal as a function of depth in the metal 15 ps after optical excitation with a 400 nm pump pulse for, (a) a 522 nm thick Au layer, (b) a 315 nm thick Ni layer, (c) a 145 nm Au layer, and (d) a 147 nm Ni layer.

ments as sharp rising and falling signals in the time-dependent diffraction signal. In Figure 6.7 (c), we show the calculated lattice temperature as a function of depth inside the 145 nm thick Au layer present in between the glass and 5 pairs of SiO_2/Si_3N_4. In this case, the Au layer is thin enough that after 15 ps, the lattice is heated almost homogeneously. There is practically no spatial gradient in the lattice temperature. In Figure 6.7 (d), we plot the calculated lattice temperature as a function of depth for the 147 nm thick Ni layer, on which the 10 pairs of SiO_2 and Si_3N_4 layers have been fabricated. In contrast to the calculations for 145 nm Au, here

the lattice temperature distribution still shows a significant temperature gradient. The acoustic wave launched by the heated lattice in this case is, therefore, shorter than that in the Au layer.

6.3.5 Displacement amplitude at the glass-metal interface

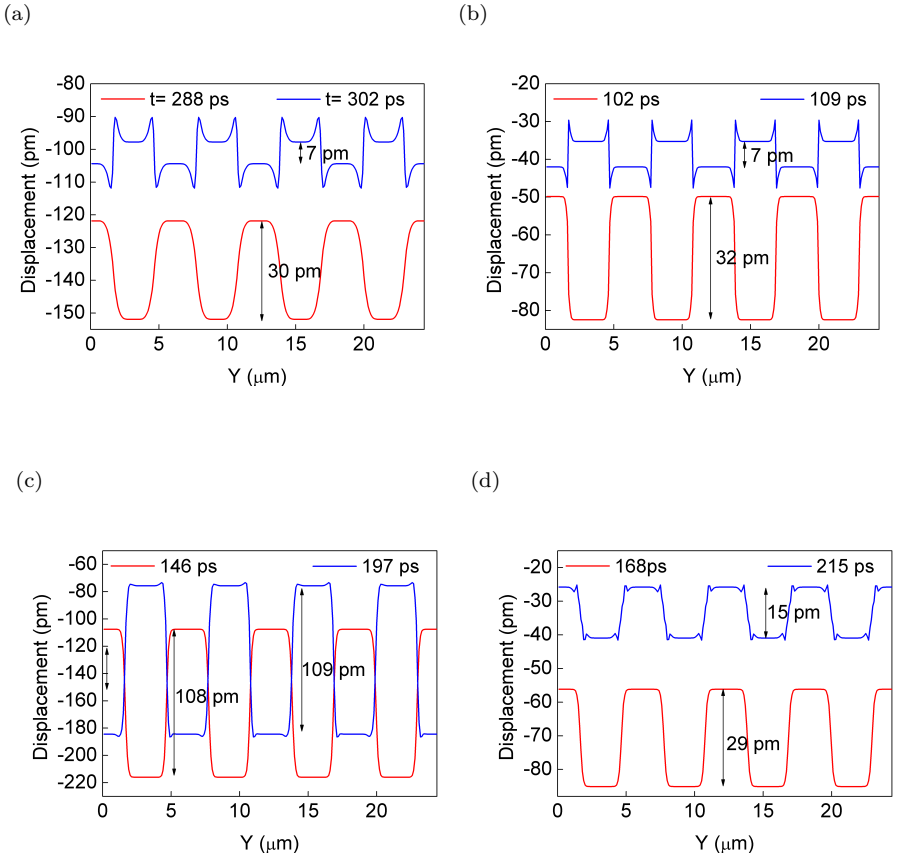

Figure 6.8: (a) Lattice displacement calculated at the glass-Au interface for the 522 nm Au sample with the 10 nm buried grating at time delays of 288 ps and 302 ps after optical excitation. (b) Lattice displacement calculated at the glass-Ni interface for the 315 nm Ni sample with 10 nm buried grating at time delays of 102 ps and 109 ps after optical excitation. (c) Lattice displacement calculated at the glass-Au interface for the "Au-multilayer" sample at time delays of 146 ps and 197 ps after optical excitation. (d) Lattice displacement calculated at the glass-Ni interface for the "Ni-multilayer" sample at time delays of 168 ps and 215 ps after optical excitation.

To get an estimate of the typical surface displacement amplitudes near the

glass-metal interface, we plot in Figure 6.8 the lattice displacement as a function of the position along the direction perpendicular to the grating lines for two different times after optical excitation, for the four different samples discussed in this paper. Here, four unit cells used in the simulations are shown for clarity, where one unit cell has a width of 6 µm. In the convention used here, the unperturbed glass-metal interface has zero amplitude displacement, and a negative displacement implies a movement of the interface in the direction of the glass substrate. In Figure 6.8 (a), we plot the displacement of the glass-Au interface for the 522 nm Au sample with the 10 nm buried grating, for pump-probe delays of 288 ps (red curve) and 302 ps (blue curve). At 288 ps, the acoustic wave has completed one round trip inside the 522 nm Au, and the maximum diffraction efficiency due to the displacement of the Au lattice is calculated. The grating-shaped displacement at the glass-Au interface has the same phase as the buried grating and has a peak-to-valley amplitude of 30 pm. The lattice displacement shows an offset of over 100 pm, which is partially caused by the acoustic wave and partially by the expansion of the lattice due to heating. However, only the grating-shaped displacement profile contributes to the diffraction efficiency. At 302 ps, we observe that the phase of the grating-shaped lattice displacement has changed by π and the peak-to-valley amplitude has decreased to 7 pm. The π phase change can be explained by the presence of two acoustic-wave gratings: one reflected off the valleys of the buried grating, the other off the peaks of the buried grating. The interference between the acoustic wave gratings, which have slightly different arrival times, leads to the occasional inversion of the interface displacement grating, which is equivalent to a spatial π phase change.

A similar effect can be seen in the lattice displacement plot for the 315 nm Ni sample shown in Figure 6.8 (b). The grating-shaped displacement at 102 ps (red curve) has the same phase as the buried grating and the π phase shift of the displacement grating occur at 109 ps (blue curve). Another interesting observation from these calculations is the difference in the shape of the lattice displacement grating for the Au and Ni samples shown by the red curves in Figure 6.8 (a) and Figure 6.8 (b), respectively. For the Ni sample, the grating-shaped displacement profile is 'sharper' than for the Au sample. This difference is due to acoustic diffraction from the

buried grating. Since the acoustic waves generated inside the Au layer have a much larger wavelength, acoustic wave diffraction is more prominent than inside the Ni layer. This leads to a more smeared out, smoother grating at the interface.

In Figure 6.8 (c), we show the displacement at the glass-Au interface for the "Au-multilayer" sample at pump-probe delays of 146 ps (red curve) and 197 ps (blue curve). The grating-shaped displacement at 146 ps has the same phase as the buried grating and has a peak-to-valley amplitude of 108 pm. The displacement amplitude is larger than in the case of the 522 nm Au sample because the lattice heating in the case of 145 nm Au is confined to a smaller volume which in turn gives rise to a stronger acoustic wave. This is also evident from the heating profile curves in Figure 6.7 (a) and Figure 6.7 (c). The grating-shaped displacement at 197 ps has a slightly higher peak-to-valley amplitude of 109 pm and, hence, a higher diffraction efficiency.

In Figure 6.8 (d) we show the displacement at the glass-Ni interface for the "Ni-multilayer" at a pump-probe delay of 168 ps, when the acoustic wave has completed one round trip (red curve). The grating-shaped displacement profile has a peak-to-valley amplitude of 29 pm and has the same phase as that of the buried grating. The grating-shaped acoustic wave, now at the glass-Ni interface, undergoes another reflection inside the 147 nm Ni layer. The acoustic wave returns to the glass-Ni interface and results in optical diffraction 215 ps after optical excitation. Hence, the grating-shaped displacement at 215 ps (blue curve in Figure 6.8 (d)), has the same phase as the one at 168 ps but a reduced peak-to-valley amplitude of 15 pm. This displacement grating has a lower amplitude because the acoustic wave is also transmitted into the stack of dielectric layers upon reflection at the Ni-SiO_2/Si_3N_4 interface, and also due to damping and dispersion of the acoustic wave during the propagation through the 147 nm Ni layer.

6.3.6 Linear reflectance measurements on multi-layer sample

To verify that the thicknesses of SiO_2 and Si_3N_4 layers in complex samples are as we expect, we performed white light reflectance measurements on

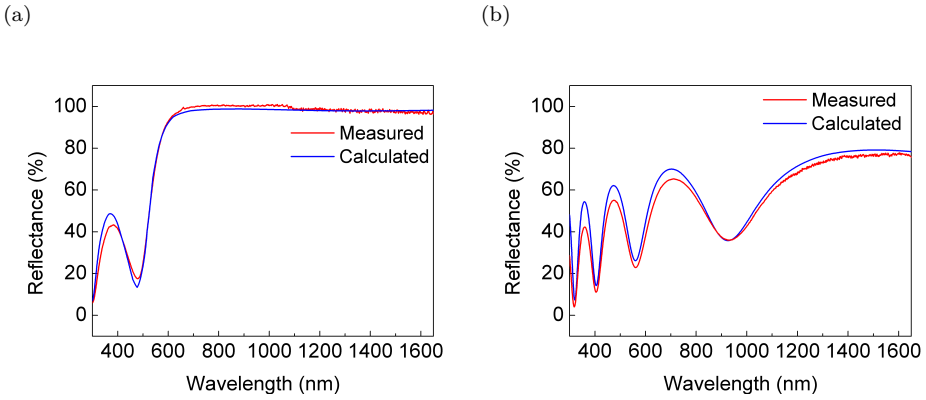

Figure 6.9: (a) The measured and calculated reflectance as a function of wavelength for the "Au-multilayer" sample when measured from the dielectric side. (b) The measured and calculated reflectance as a function of the wavelength for the "Ni-multilayer" sample when measured from the dielectric side.

these samples from the dielectric side. We used a commercial visible/IR "white" light reflectance measurement device (Filmetric, F-20) to measure the reflectance spectrum. The fiber-coupled white light is incident at normal incidence on a flat part of the sample (without the grating) and the reflected spectrum is recorded by the same fiber and plotted as a function of the wavelength. The measured spectrum is then fit with the calculated refection spectrum where the thickness of the SiO_2 layer and Si_3N_4 layer are varied until a fit best was obtained. The reflected spectrum is calculated using a model that solves the Fresnel's equation at each interface for every wavelength. The model uses the literature value of the dielectric constants of the Au, Ni, SiO_2 and Si_3N_4 [130, 131].

In Figure 6.9 (a) we plot the measured and the calculated reflectance as a function of the wavelength for the "Au-multilayer" sample. For this sample, the best fit was obtained when the thickness of SiO_2 layer was 18 nm, and the thickness of Si_3N_4 was 18 nm. Similar measurements were performed on the "Ni-multilayer" sample and is shown in Figure 6.9 (b). Here, the best fit was obtained when the thickness of SiO_2 layer was 18.5 nm, and the thickness of Si_3N_4 was 18.5 nm. The model used in the calculations always assumes flat interfaces and no surface roughness. However, in reality, we expect interfaces to be not perfectly flat and the surface to have a roughness

with an root mean square value of 1 nm. This could explain the slight deviation of the calculation from the measurements.

6.3.7 Visualization of strain propagating in "Au-multilayer" sample

The propagation of the strain wave inside the "Au-multilayer" sample calculated using the numerical simulations is plotted in Figure 6.10 (a)-(h). The y-axis is the position along the direction perpendicular to the grating lines. The color scheme shows the strain, and the time is displayed on top of the figure. Here, four unit cells used in the simulations are shown for clarity, where one unit cell has a width of 6 µm. The thickness of the glass substrate used in the measurements is 175 µm, but in the simulations we use 6 µm. This was done because a 6 µm thick layer is sufficient for modeling as the acoustic wave does not propagate more than 5 µm during the time duration of the measurements. However, for clarity only 0.85 µm of the glass is shown in the figures.

All the physical effects discussed in this chapter can be seen in these figures. At time delay zero, the strain inside the sample is zero (Figure 6.10 (a)). The uniform heating of the 145 nm thick Au layer launches an acoustic wave, which exerts strain at both ends of the 145 nm Au layer (Figure 6.10 (b)). The strain wave propagates through the Au layer and dielectric layers, reflects off the buried grating and acquires a grating-shape (Figure 6.10 (c)). Note that the strength of the strain wave appears different in Au, glass, SiO_2, and Si_3N_4 because strain depends on the mechanical properties of the material. The grating-shaped strain reaches the glass-Au interface and partially transmits into the glass substrate (Figure 6.10 (d)). We can also see the grating-shaped strain near the glass-Au interface which leads to the grating-shaped displacement of the interface at 146 ps and 197 ps (Figure 6.10 (d) and (e)). Here we can see that the strain gratings at 146 ps and 197 ps are inverted. Later in time, partial reflection and transmission of the strain wave at the glass-Au interface and Au-dielectric stack interface can be seen (Figure 6.10 (f) and (g)). At longer time delays the strength of the strain wave reduces due to damping, dispersion and losses upon partial reflection and transmission at the interfaces (Figure 6.10 (g) and (h)).

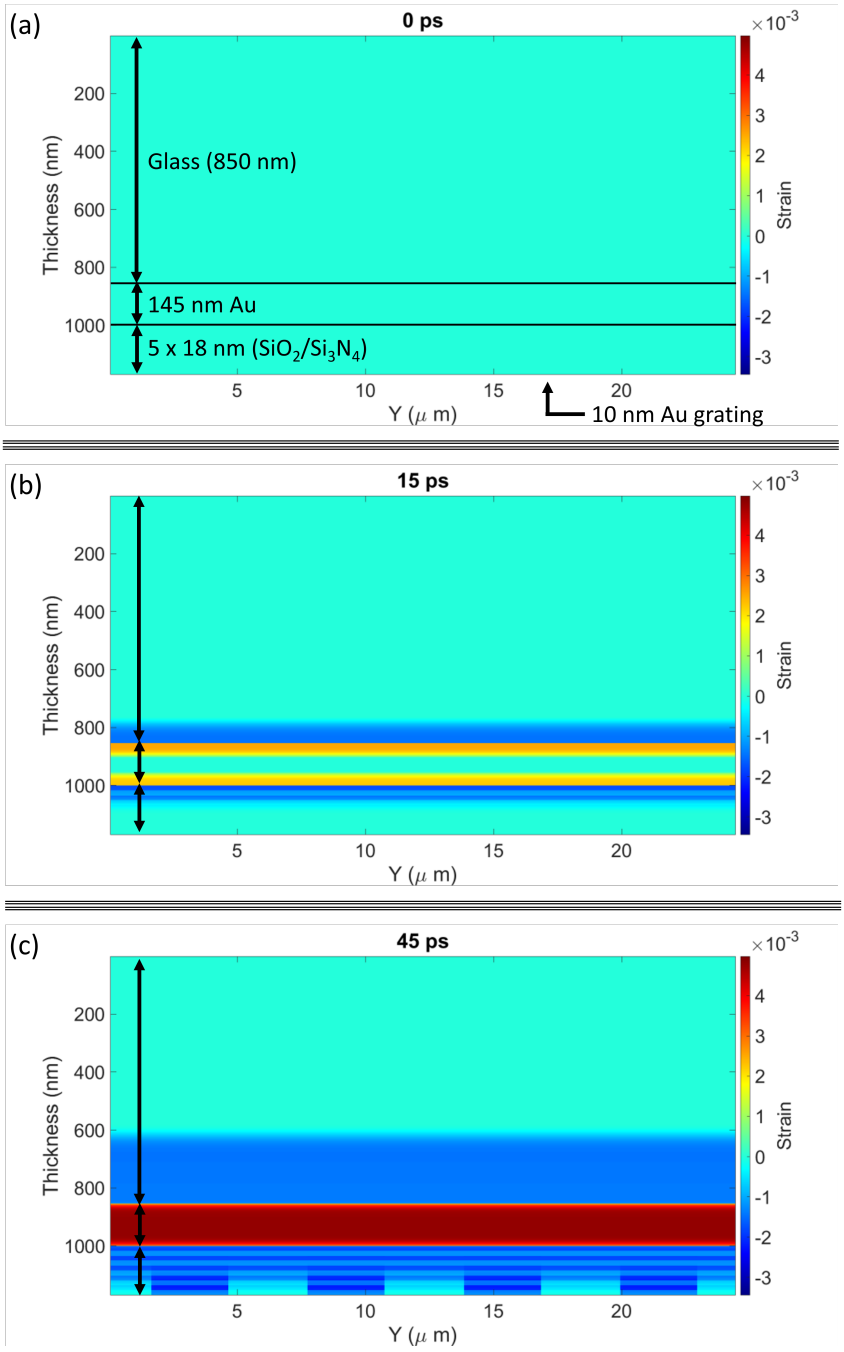
(a)
0 ps
Glass (850 nm)
145 nm Au
5 x 18 nm (SiO_2/Si_3N_4)
10 nm Au grating
(b)
15 ps
(c)
45 ps
Thickness (nm)
Y (μ m)
Strain
$\times 10^{-3}$

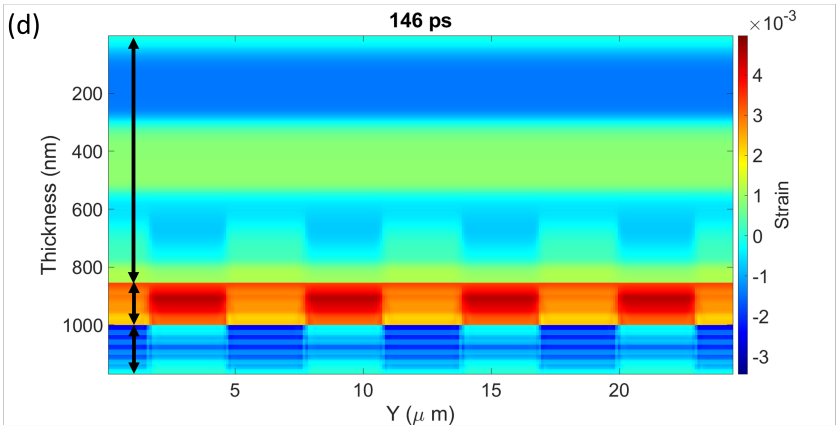
(d)
146 ps
×10^-3
4
3
2
1
0
-1
-2
-3
Strain
200
400
600
800
1000
Thickness (nm)
5
10
15
20
Y (μ m)

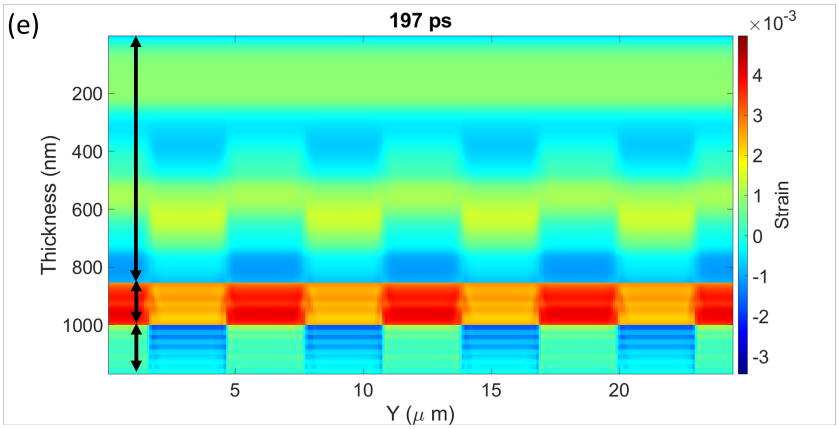
(e)
197 ps
×10^-3
4
3
2
1
0
-1
-2
-3
Strain
200
400
600
800
1000
Thickness (nm)
5
10
15
20
Y (μ m)

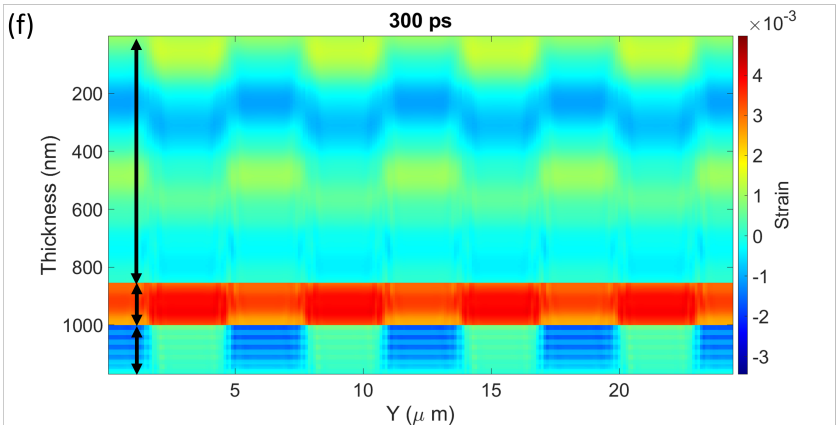
(f)
300 ps
×10^-3
4
3
2
1
0
-1
-2
-3
Strain
200
400
600
800
1000
Thickness (nm)
5
10
15
20
Y (μ m)

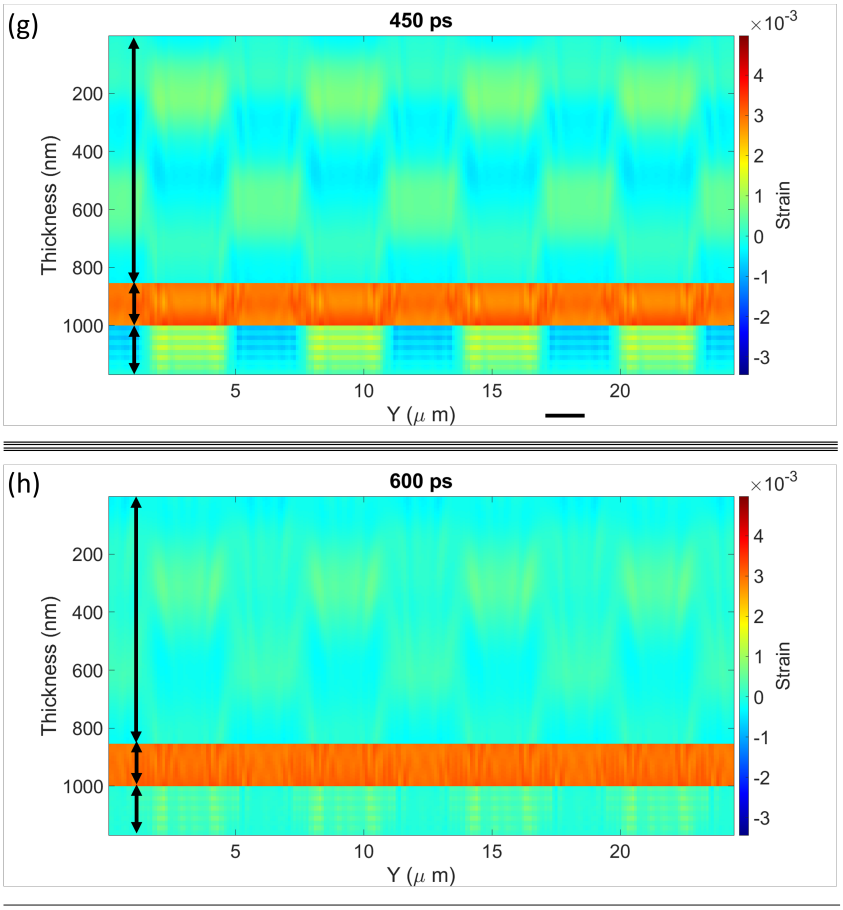

Figure 6.10: (a)-(h) Numerical calculations showing the propagation of strain inside the "Au-multilayer" sample.

6.3.8 Material properties

In Table 6.1 and 6.2 we list the material properties used in the numerical simulations.

	Au	Ni
Optical penetration depth at 400 nm (nm)	16	12
Optical penetration depth at 800 nm (nm)	13	13
Electron-phonon coupling constant (10^{16}Wm^{-3}K^{-1})	3.2	36

Table 6.1: Properties of the Au and Ni used in our TTM calculations [21, 64, 84, 85, 122].

	Sound velocity (m/s)	Acoustic Impedance (10^6Ns/m^3)
Au	3,200	63.8
Ni	5,800	51.5
Glass substrate	5,700	12.54
SiO_2	5,100	13.5
Si_3N_4	5,600	17.9

Table 6.2: Acoustic properties of different materials used in our calculations [30, 40].

6.4 Conclusion

We have shown that laser-induced ultrasonics can be used to detect the presence of gratings buried under optically opaque metal and dielectric layers. We observe optical diffraction from the acoustic wave reflected from a grating buried under thick Au and Ni layers. The diffraction is due to the grating-shaped displacement of atoms at the glass-metal interface and Brillouin scattering in the glass substrate. We attribute the difference in the shape of the time-dependent diffraction signal for Au and Ni to the difference in electron-phonon coupling strength of these two metals. Our measurements on complex multilayer samples show that the grating-shaped acoustic wave can be detected even after it has propagated through multiple SiO_2 and Si_3N_4 layers. The numerical calculations are in agreement

with the measurements and also show that the acoustic wave "sees" the SiO_2/Si_3N_4 stack as an equivalent time-averaged acoustic medium. The results of our experiments and simulations strongly suggest that this technique can be used for sub-surface metrology applications, especially in the semiconductor device manufacturing industry.

7

Detection of low amplitude buried gratings and the role of surface roughness

We report on the use of laser-induced ultrasonics for the detection of gratings with amplitudes as small as 0.5 nm, buried underneath an optically opaque nickel layer. In our experiments, we use gratings fabricated on top of the nickel layer on glass, and we optically pump and probe the sample from the glass side. The diffraction of the probe pulse from the acoustic echo from the buried grating is measured as a function of time. We use a numerical model to show how the various physical phenomena such as interface displacement, strain-optic effects, thermo-optic effects, and surface roughness influence the shape and strength of the time-dependent diffraction signal. More importantly, we use a Rayleigh-Rice scattering theory to quantify the amount of light scattering, which is then used as in input parameter in our numerical model to predict the time-dependent diffracted signal.

Parts of this chapter are contained in a manuscript currently under review.

7.1 Introduction

In the previous chapter, we demonstrated that it is possible to detect gratings buried underneath optically opaque metal and ten to twenty dielectric layers using laser-induced, extremely-high frequency acoustic waves. In those experiments, the presence of a buried grating is detected by optical diffraction off an acoustic copy of the buried grating. However, little is known about the limitations of this technique, in particular, the sensitivity of the technique to detect very small amplitude buried gratings.

In this chapter, we show that photoacoustics in an ultrafast pump-probe scheme can be used to detect the presence of very shallow gratings, down to 0.5 nm in amplitude, buried under optically opaque nickel (Ni) layers (Figure 7.1). In our experiments, a femtosecond pump-pulse launches an acoustic wave in a 130 nm thick Ni layer. The acoustic wave propagates through the Ni layer and reflects off a low amplitude buried Ni grating. Upon reflection, the wavefront of the acoustic wave acquires a spatially periodic phase, which can be viewed as an acoustic copy of the buried grating. The grating-shaped acoustic wave returns to the glass-metal interface, deforming the interface in a spatially periodic manner. The detector placed at a location where one would expect the first-order diffraction records a signal due to the diffraction of a delayed femtosecond probe-pulse from the grating-shaped acoustic wave. The fact that we observe a diffracting signal in itself is proof that the shape of the buried grating is encoded as a spatially periodic time delay on the acoustic wavefront. We use a complex 2D numerical model that includes the acoustic wave generation, propagation, and detection to predict the signal shapes in our measurements [18]. The numerically calculated diffraction signals are in excellent agreement with our measurements on all of the samples. We show that the strength and shape of the time-dependent diffraction signals are dependent on the amplitude of the buried grating. We also describe and quantify the different physical effects that cause the time-dependent diffraction signals and explain how each one affects the shape of the diffracted signal. From the measurements on the sample with smaller-amplitude buried gratings, we find that interface roughness plays a very significant role. Light scattered due to the interface roughness interferes with the light diffracted from the

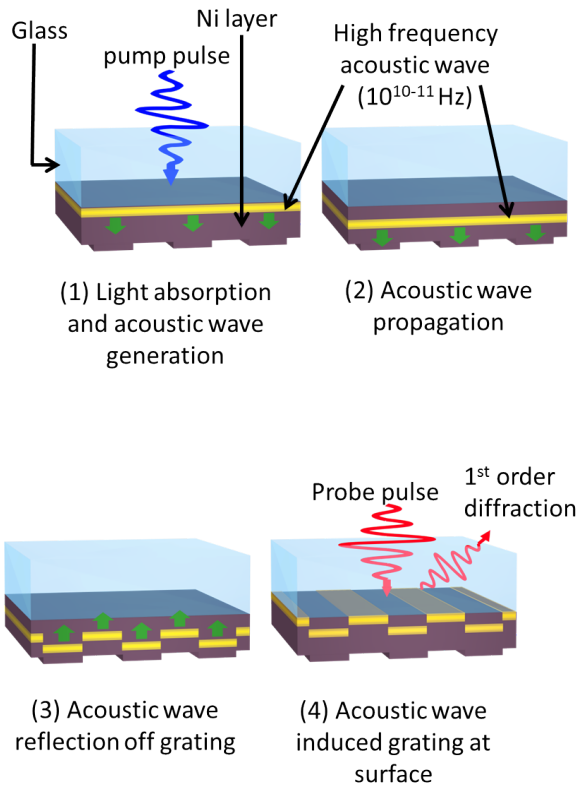

Figure 7.1: Schematic explaining the technique. A 400 nm wavelength femtosecond laser pulse is absorbed by the material at the substrate-material interface (1), which launches an acoustic wave that propagates through different layers (2). The acoustic wave reflects off the buried grating and returns to the substrate-material interface as a grating-shaped acoustic wave (3). The time-delayed femtosecond probe pulse diffracts off this interface grating, and the first-order diffraction signal is recorded (4).

acoustic wave-induced gratings and leads to constructive/destructive interference which changes the shape and amplitude of the measured diffracted signal.

7.2 Experimental setup

A schematic of the pump-probe setup used for the experiments is shown in Figure 7.2. A Ti:Sapphire multi-pass amplifier generates 30 fs pulses with a

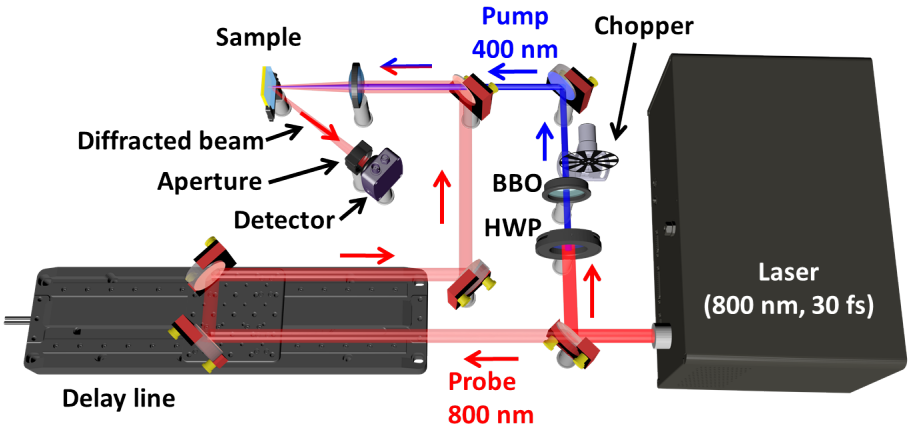

Figure 7.2: Schematic of the experimental setup. The frequency-doubled 400 nm pump pulse is focused onto the sample and the 800 nm probe pulse that diffracts off the "copy" of the buried grating is recorded by the detectors while the delay line is used to change the pump-probe delay

repetition rate of 1 kHz and with a wavelength centered at 800 nm. A 95/5 beam splitter splits the output in two. The stronger beam is frequency-doubled to generate 400 nm pump pulses, and the weaker 800 nm beam is used as a probe pulse. The pump pulse passes through a 500 Hz chopper, which blocks every alternate pump pulse. Both pump and probe are weakly focused onto the sample. The pump beam has a spot size of 500 µm, while the probe beam has a spot size of 250 µm on the sample.

Our samples consist of Ni gratings fabricated on top of a 130 nm thick flat Ni layer on a glass substrate. The samples are illuminated from the substrate side. This means that the pump and the probe illuminate the flat side of the Ni layer and thus, cannot "see" the grating as the penetration depth of both pump and probe are much smaller than the thickness of the grating. A delayed probe pulse diffracts from the acoustic wave-induced grating and is recorded by a Si-photodiode placed at an angle where the first-order diffracted pulse is expected. The delay between the pump and the probe is varied using a mechanical delay line. The measured signal is the diffracted probe signal recorded by the detector when the chopper blocks the pump beam subtracted from the diffracted probe signal when

the pump beam is transmitted by the chopper. This is done to select only the pump-induced changes to the diffracted signal.

All of the samples were fabricated with a pitch of 6 µm on a 130 nm thick flat Ni layer on a glass substrate. The Ni layer was deposited using electron beam evaporation, and the thickness was monitored using a calibrated quartz crystal monitor. On top of the flat Ni layer, Ni gratings were fabricated by UV lithography.

7.3 Results and discussion

7.3.1 Pump-probe experiments and simulation

We performed pump-probe experiments on four different samples with different Ni grating amplitudes of 12, 6, 2, and 0.5 nm. In Figure 7.3 (bottom four panels), we plot the measured diffracted signal of these samples as a function of pump-probe delay (red curves). In the top panel, we show the measurement on a 130 nm thick layer of Ni with out buried grating. All of the curves, except for the top one, are normalized to their maximum value and are vertically displaced for clarity. For the bottom four plots, we observe that the measured diffracted signal remains zero for approximately 35-40 ps, rising to a maximum at 46±1 ps. This peak is also the maximum of the time-dependent diffraction signal. After 65 ps, we observe a diffraction signal that is quasi-periodic and persists for more than 700 ps, where the shape and strength vary depending on the amplitude of the buried grating. In the measurements on the 2 and 0.5 nm amplitude buried grating samples, we observe a signal that periodically goes below the value observed at negative time delays. The signals from the measurements on 12 and 6 nm amplitude buried grating samples show a quasi-periodic oscillation that is superimposed on a gradually increasing signal.

The fact that we observe a diffracted signal implies that we are able to detect the presence of buried gratings by diffracting the probe pulse from an acoustic "copy" of the buried grating at the glass-Ni interface. Our measurements show that we can detect extremely shallow buried gratings with an amplitude as low as 0.5 nm underneath an optically opaque Ni layer using laser-induced ultrasonics. In all of the measurements on buried

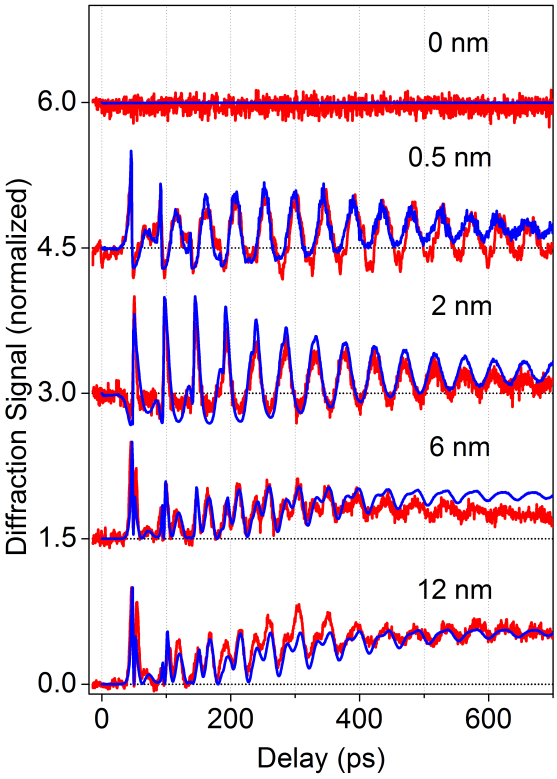

Figure 7.3: The red curves are the experimentally measured diffracted probe signals plotted as a function of pump-probe delay for five gratings fabricated on 130 nm thick Ni layer. Different panels show the measured signal from gratings with an amplitude of 12 nm, 6 nm, 2 nm, 0.5 nm, and 0 nm. The pitch of all gratings is 6 µm. The blue curves are the numerically calculated diffraction signals as a function of pump-probe delay for each sample.

gratings, we would expect the first reflection from the buried grating to arrive at the glass-Ni interface at 46±1 ps. For a 130 nm thick Ni layer, the round trip time of the acoustic wave can be calculated as $T = 2l/v$, where l is the layer thickness and v is the speed of sound in the metal. Assuming a longitudinal velocity of 5.8 km/s [40], the round trip time is expected to be 45 ps, which is close to the position of the first diffracted signal peak we

observe in our measurements.

To better understand the measured time-dependent diffracted signals, we performed numerical simulations using an advanced 2D model developed by Hao Zhang et al. [18]. The model consists of a set of equations that describes the generation, propagation, and optical detection of high-frequency acoustic waves. The numerically calculated diffraction signal is shown by the blue curves in the same graph (Figure 7.3) for all five samples. The optical and material parameters were mostly taken from the literature and unknown parameters, such as the strain-optic coefficient and the thermo-optic coefficient, are manually adjusted until the best fit between the measurements and the calculations was obtained. Once the optical and material parameters were fixed, calculations were performed for the samples with different buried grating amplitude. We find that our simulations are in excellent agreement with the measurements.

To identify the various physical mechanisms contributing to the measured diffracted signals, we show in Figure 7.4 the various factors contributing to the calculated diffraction signal for (i) the 2 nm amplitude buried grating on 130 nm thick Ni (Figure 7.4 (a)) and, (ii) the 12 nm amplitude buried grating on 130 nm thick Ni (Figure 7.4 (b)). Although we can show the contributing factors for all of the buried grating samples, we have selected the 2, and 12 nm amplitude buried grating samples to highlight the difference in the relative contribution of different factors for these two samples. In Figure 7.4 (a) and (b), we plot the calculated diffraction signal from this sample from *only* the (i) displacement of the glass-Ni interface by the grating-shaped acoustic echo in Ni (green panels), (ii) changes in the optical constants of the glass due to the strain-optic effect (blue panels), (iii) changes in the optical constants of Ni due to the strain-optic effect (magenta panels), (iv) changes in the optical constants of the Ni due to the thermo-optic effect (yellow panels), (v) scattering from random surface roughness at the Ni-glass interface (orange panels). All of these plots are divided by the maximum value calculated for the black curve in the green panel of Figure 7.4 (a). For the ease of comparison, in the top panel, we show the measured diffracted signals (red curves) and the calculated diffracted signal, including all contributions (blue curves) for the same sample. The top panel in Figure 7.4 (a) and (b) are same as the 3rd and 1st panel from

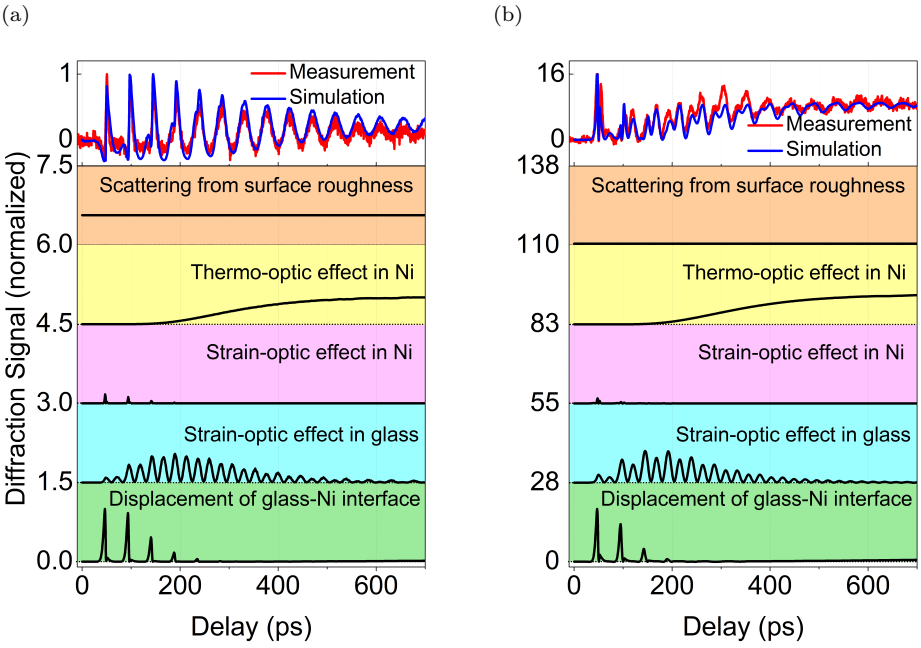

Figure 7.4: (a) The bottom 5 panels show the numerically calculated diffraction signal if only one factor contributing to the diffraction signal is taken into account for the sample with a 2 nm amplitude grating fabricated on 130 nm Ni. The top panel shows the measured and numerical calculated diffraction signal for the same sample when all factors are taken into account. (b) Same as (a) but for the sample with a 12 nm amplitude grating fabricated on 130 nm Ni.

the bottom in Figure 7.3, respectively. We now discuss the different factors that influence the strength and shape of the time dependent diffraction signal.

7.3.2 Displacement of glass-Ni interface

The acoustic wave generated in Ni at the glass-Ni interface propagates through the thick Ni layer, reflects off the buried grating, and returns to the glass-Ni interface as a grating-shaped echo. The acoustic echo displaces the atoms at the glass-Ni interface leading to an extremely shallow physical grating with an amplitude of few picometers only, having the same pitch as the buried grating. The peak-to-valley amplitudes of the displacement grating at the time delay where we observe the maximum diffraction effi-

ciency, are 8 and 34 pm for the sample with 2 and 12 nm buried grating amplitudes, respectively. The acoustic wave undergoes multiple round trips inside the Ni layer, and a grating is formed each time the acoustic wave reaches the glass-Ni interface. The probe pulse diffracts from this grating and results in peaks in the diffraction signal that are separated by 46 ps, which is the acoustic round trip time inside the 130 nm Ni layer using the sound velocity in Ni of 5.8 km/s [40]. This can be seen in the bottom panel of Figure 7.4 (a) and (b), where we observe peaks in the diffracted signal from multiple acoustic echoes, all separated by about 46 ps. Also, the diffracted signal gets weaker upon every round trip, as the acoustic wave in Ni loses its energy due to the partial reflection at the glass-Ni interface by an amount determined by the acoustic impedance mismatch between the glass and Ni.

7.3.3 Strain-optic effect in glass substrate

When the grating-shaped acoustic echo is at the glass-Ni interface, part of the acoustic wave is transmitted into the glass substrate, where it continues to propagate away from the interface. The acoustic grating modifies the refractive index in glass due to the strain-optic effect and results in a grating in the optical constants of the glass. Usually, such a quasi-static grating in the glass would give rise to a constant (in time) diffracted signal. However, the same probe pulse that is diffracted from the acoustic grating also reflects from the glass-Ni interface before diffracting again from the acoustic grating in the same direction. This leads to interference between the electric fields of the diffracted pulses. Whether the interference is constructive or destructive depends on the phase accumulated by the optical pulse before it diffracts a second time. As the acoustic grating travels away from the glass-Ni interface, this optical phase difference changes periodically as a function of time. This causes alternate constructive or destructive interference leading to an oscillation of the diffracted signal as shown by the blue panel of Figure 7.4 (a) and (b). Due to multiple round trip of the acoustic wave in Ni, more than one grating-shaped acoustic waves are propagating in the glass substrate after about 100 ps. The probe light can diffract from all these grating-shaped acoustic echoes in the glass. Gradually, the diffraction signal gets weaker due to dispersion and damping of

the acoustic wave in the glass.

7.3.4 Strain-optic effect in Ni

When the grating-shaped acoustic echo arrives at the glass-Ni interface, it also modifies the complex refractive index of Ni near the glass-Ni interface due to the strain-optic effect. This results in a grating in the optical constants. The probe pulse diffracts from this grating, giving rise to a diffracted signal peak each time the grating-shaped acoustic echo arrives at the glass-Ni interface, as shown in the magenta panel of Figure 7.4 (a) and (b). Since this grating is the result of an acoustic wave bouncing back and forth inside the Ni layer, the peaks of the diffracted signal are separated by 45 ps, which is the acoustic round trip time inside the 130 nm thick Ni layer. The transient, periodic (in time) grating at the glass-Ni interface due to strain-optic effect and due to the displacement of the atoms at the glass-Ni interface (shown in the green panel in Figure 7.4 (a) and (b)), always occur simultaneously. However, as the strain-optic coefficient of Ni is small, diffraction due to the strain-optic effect is weak in comparison to the diffraction due to the interface displacement.

7.3.5 Thermal grating in Ni

The optical pump pulse is absorbed by the Ni layer within the optical penetration depth (13 nm for 400 nm wavelength light), creating a hot electron gas [122]. The hot electron gas cools by heating up the Ni lattice. As Ni has a very high electron-phonon coupling strength, the hot electron gas cools to lattice before the energy can diffuse much deeper into the Ni layer [20–23]. As a result, the top layer of Ni heats up with an exponentially decaying temperature gradient in a direction perpendicular to the surface of the Ni layer. Later in time, the heat diffuses even deeper into the metal layer and reaches the buried grating. Due to the difference in diffusion volume above the valleys and the peaks of the buried grating, a spatially periodic temperature pattern is formed, which is also present near the glass-Ni interface. The change in the temperature modifies the complex refractive index of Ni due to the thermo-optic effect and results in a grating in the optical constants of Ni. The calculated diffraction signals resulting from this thermal grating are shown in Figure 7.4 (a) and (b) (yellow panels).

In both plots, the signal remains zero for approximately 125 ps, and later gradually increases to a quasi-constant value. This is because lattice heat slowly diffuses deeper into the Ni layer, and it takes a finite amount of time before temperature contrast is achieved between areas above the valleys and peaks of the grating. The diffracted signal reaches a constant value when the temperature gradient along the vertical direction vanishes, and a quasi-constant temperature is attained above the valleys and above the peaks of the grating, each at different temperature value. The lateral diffusion of heat does not wash away the thermal grating on the time scale of our experiments (<1 ns) because the thickness of the layer (130 nm) is much smaller than the pitch of the grating (6000 nm). The effects due to lateral lattice heat diffusion are nonetheless taken into account in our numerical model.

7.3.6 Surface roughness

The most surprising factor that affects the shape and strength of the diffracted signal is the surface roughness of the glass-Ni interface. The random surface roughness of the glass-Ni interface results in the scattering of probe light in all directions. The Si-photodiode placed at the location where we expect the first-order diffracted light from the acoustic gratings, also detects the light scattering in that particular direction. The intensity of the scattered light is more or less constant. The random surface scattering needs to be taken into consideration when the intensity of the probe pulse diffracted from the acoustic gratings is comparable to or weaker than the intensity of the randomly scattered light. The intensity of the background scattered light is experimentally measured when the chopper blocks alternating pump pulses and is numerically subtracted from the measured diffracted signal. However, the electric field of the scattered light interferes with the electric field of the diffracted light, and the measured diffracted intensity is the coherent sum of these electric fields. Hence a numerical subtraction of measured signals does not correctly remove the contribution of the scattered light. In our numerical simulations, we add an electric field with a constant amplitude which coherently adds up to the diffracted electric field. In Figure 7.4 (a) and (b) (orange panel) we show the calculated contribution to the diffraction signals for the 2 and 12 nm amplitude

buried grating samples, assuming that only the constant electric field we have added is present. The "scattered signals" are constant in time. Although the strength of the constant diffracted field is the same for both samples, their strength with respect to the diffraction signals due to other effects varies. Therefore, in Figure 7.4 (a), the constant line has a value comparable to that due to other effects and hence has a significant contribution to the total diffracted signal. In Figure 7.4 (b), we see that the "scattered signal" has a value very close to zero and therefore has an almost negligible contribution to the diffraction signals caused by the other effects. The amplitude of the added electric field is estimated with the help of an analytical scattering model and the details are discussed below.

Surface scattering model: Rayleigh-Rice theory

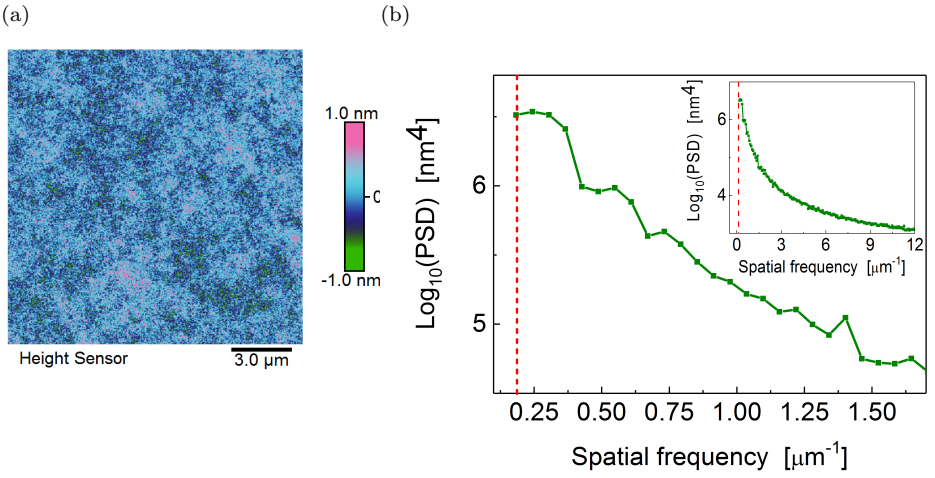

Figure 7.5: (a) AFM measurement showing the height profile of the glass surface. (b) PSD vs. spatial frequency calculated from the AFM measurement. The vertical red line marks the spatial frequency of the buried grating.

We use the Rayleigh-Rice scattering theory, to estimate the intensity of the scattered light recorded by the detector [132–135]. The Rayleigh-Rice approach can be used in cases where the Root Mean Square (RMS) roughness of the surface, σ, is much less than the incident optical wavelength λ, that is $\sigma/\lambda < 0.01$ [132, 135]. To obtain the amount of light scattered towards the detector using Rayleigh-Rice theory, we need to obtain the topography of the surface from which the light scatters. Measuring the roughness pro-

file of the glass-Ni interface directly is not possible with an AFM, hence we measured the roughness profile of the glass substrate and assume that the roughness profile of the glass-Ni interface will follow the glass surface topography. This is a reasonable assumption given that Ni was evaporated at a very slow rate and that Ni atoms have a good affinity for the glass which ensures that the deposited Ni layer will follow the topography of the glass substrate. We measure the topography of the glass substrate for an area of about $17\,\mu m^2$ using an AFM. The measured topography is shown in Figure 7.5 (a). The RMS roughness of the measured surface was calculated to be 307±5 pm. Using the Rayleigh-Rice scattering theory we can obtain the Angle Resolved Scattering (ARS) by calculating the Power Spectral Density (PSD) function from the measured AFM data. The ARS is defined as the ratio between the power of the scattered light, $P_s(\alpha_s)$, and the power of the incident light, P_i, normalized to a finite solid angle, $\Delta\Omega$ and α_s is the scattering angle with respect to the normal to the scattering surface. Mathematically ARS can be expressed as [132, 135, 136],

$$ARS(\alpha_s) = \frac{P_s(\alpha_s)}{\Delta\Omega_s P_i}, \tag{7.1}$$

The PSD is a measure of surface roughness which provides information about the different spatial frequency components present in the surface roughness. Mathematically a 2D PSD is the modulus squared of the surface profile's 2D Fourier transform and can be written as,

$$PSD(f_x, f_x) = \lim_{L\to+\infty} \frac{1}{L^2} \left| \int_0^L \int_0^L z(x,y) e^{-2\pi i(f_x x + f_y y)} dxdy \right|^2. \tag{7.2}$$

Here L is the length of the scanned area, $z(x, y)$ is the surface topography which has a zero mean, and f_x and f_y are the two spatial frequencies components of the surface roughness where x and y are the two in-plane spatial coordinates. In Rayleigh-Rice scattering theory, there is a simple relation between the ARS and the PSD [135, 136],

$$ARS(\alpha_s) = Q\frac{16\pi^2}{\lambda^4} \cos(\alpha_i) \cos^2(\alpha_s) PSD(f). \tag{7.3}$$

Here α_i is the incident angle with respect to the normal to the scattering surface, Q is the polarization-dependent optical reflectance of the scattering surface, and f is the spatial frequency.

In Figure 7.5 (b) we plot the calculated PSD as a function of the spatial frequency for the surface topography shown in Figure 7.5 (a). In our experiments, $\alpha_i = 10°$, $\alpha_s = 18°$ and $Q = 0.68$ [122] for $\lambda = 800$ nm. The value for $\Delta\Omega$ is determined by the size of the aperture just in front of the photodiode and it was measured to be approximately 5.5×10^{-6} sr. The detector is placed at an angle such that it measures light scattered from a spatial frequency of $0.67\,\mu m^{-1}$, which is the spatial frequency of the buried grating. From Figure 7.5 (b), the PSD we obtain for the $0.67\,\mu m^{-1}$ spatial frequency is $10^{6.5} = 3.16 \times 10^6$ nm^4. Substituting all these values in Eq. 7.3, we calculate the ARS to be 6.48×10^{-4}. Using Eq. 7.1 the light scattering efficiency of rough interface along the direction of the photodetector (P_s/P_i) is calculated to be 3.56×10^{-9}.

Based on the above calculation, we have added a constant electric field along the direction of the first-order diffraction signal in the numerical simulations. The intensity of the scattered light was varied around the expected value of 3.56×10^{-9} times the intensity of the incident probe light. The best match with the measurements was observed when the intensity was 1.56×10^{-9} times the intensity of the incident probe light. The small deviation from the calculated value could be due to errors in the calculation of the PSD. It is known that PSD calculations can have errors due to limitations in accurately measuring large surface areas using an AFM. The finite size of the AFM tip and instrumental artifacts will also add to the error [137]. The phase of the added electric field is adjusted in order to obtain a good fit with the measured data for each sample. We like to point out that, despite having an RMS roughness below 0.5 nm, the contribution of the light scattered from interface roughness cannot be ignored when the diffraction signals are weak. To best of our knowledge, this is the first demonstration of the role of surface roughness in femto/picosecond laser-induced ultrasonics measurements.

7.3.7 All contributions combined:

Although we can numerically calculate the intensity of the diffracted probe pulse for each factor contributing to the diffracted signal, in actual measurements, we can only record the total diffracted intensity. The electric field of the diffracted light in a particular direction is the coherent sum of the diffracted electric fields in that direction. Therefore, the phase differences between all the diffracted electric fields are important. Of the five different effects discussed above, all except the surface roughness are induced by the pump pulse and therefore, will be dependent on the pump-probe delay. These four different effects result in gratings from which the probe pulse diffracts, and the diffracted light can be represented by a single electric field. This electric field can be written as,

$$E_a(r,t) = E_a e^{(\omega t - k\cdot r + \theta_1)}, \tag{7.4}$$

where E_a, and θ_1 are the pump-probe-delay-dependent amplitude and phase of the electric field, respectively. Note that the time dependence of the envelope of the optical ultra-short pulse is left out from the equation. However, the electric field of the light scattered due to the interface roughness from different samples has a constant amplitude and a constant but random phase. We can consider a rough interface to be the superposition of a large number of sinusoidal phase gratings with different orientations, periods, amplitudes, and phases. Since our detector is placed at a location where we expect the diffracted light from a 6 µm period grating, only roughness gratings with the same spatial frequency scatters light towards the detector. For all samples used in our experiments, we expect the roughness profile at the glass-Ni interface to be similar. Therefore we also expect the amplitude of the scattered electric field to be constant for all samples. However, the phase of the scattered electric field is random and can vary from one sample to another and also from one illumination spot to another on the same sample. Therefore, we can approximate the electric field of the light scattered due to the interface roughness along the direction of the first-order diffracted light as,

$$E_s(r,t) = E_s e^{(\omega t - k\cdot r + \theta_2)}. \tag{7.5}$$

Here, E_s and θ_2 are the *constant* amplitude and the phase of the electric field, respectively. The measured diffraction signal, which is the total intensity of the light incident on the detector, I, is proportional to the square of the total electric field. We can write,

$$I \propto |E_{tot}|^2 \tag{7.6}$$

where,

$$|E_{tot}|^2 = |E_s + E_a|^2 = |E_s|^2 + |E_a|^2 + 2|E_a||E_s|\cos(\theta_1 - \theta_2). \tag{7.7}$$

In our measurements, we numerically subtract the probe signal measured by the detector when the chopper blocks the pump pulse, thus removing the terms not induced by the pump pulse. Hence, we observe only terms that contain E_a in Eq. 7.7. The diffraction signal we plot, η, can thus be expressed as,

$$\eta \propto |E_a|^2 + 2|E_a||E_s|\cos(\theta_1 - \theta_2). \tag{7.8}$$

Now that we understand the different factors and how they contribute to the diffraction signal, we will explain why the shape of the diffracted signal is different for different samples. As the amplitude of the buried grating increases, the diffraction of the probe light due to pump-induced effects (displacement of the glass-Ni interface, strain-optic effect in Ni, thermo-optic effect in Ni and strain-optic effect in glass) gets stronger. However, the scattering of light due to the interface roughness is independent of the buried grating amplitude. In the cases of samples with 6 and 12 nm amplitude buried gratings, the diffraction from the gratings induced by the pump pulse (acoustic gratings and thermal grating) is strong (see Figure 7.4 (b)). As a result, $|E_a|$ is much larger than $|E_s|$ in the relation shown in Eq. 7.8. Therefore, in these measurements, the intensity of the light diffracted due to the gratings induced by the pump pulse, i.e., $|E_a|^2$, dominates the measured total signal. In the measured diffraction signal for 6 and 12 nm buried grating samples, the peak in diffraction signal at 46$\pm$1 ps is mostly due to the displacement of the interface. The oscillation that follows until about 200 ps is mainly due to the combined effect of the strain-optic effect and the displacement of the interface. After 200 ps, the strain-optic effect in

the glass and the thermo-optic effect dominates. The slow, gradual increase in the offset of the diffracted signal is explained by the formation of the thermal grating due to the thermo-optic effect.

For the samples with 0.5, and 2 nm amplitude buried gratings, $|E_a|$ is comparable to $|E_s|$ because the intensity of probe light diffracted from the gratings induced by the pump pulse is comparable to the intensity of the scattered probe light (see Figure 7.4 (a)). Hence, we observe the term $|E_a|^2 + 2|E_a||E_s|\cos(\theta_1 - \theta_2)$ from the relation shown in Eq. 7.8. As the grating-shaped acoustic wave propagates through the glass, the time-dependent phase of the diffracted light periodically changes between 0 and π. As a result, the value of $\cos(\theta_1 - \theta_2)$ oscillates periodically above and below zero and can result in a value of $|E_a|^2 + 2|E_a||E_s|\cos(\theta_1 - \theta_2) < 0$. This causes the "negative" diffraction signal observed in the measurements of 2 nm, and 0.5 nm amplitude buried gratings. For these measurements, the role of pump-induced effects (displacement, strain-optic effects, and thermo-optic effect) is similar to that of 12 and 6 nm buried grating samples. The only difference is the *relatively* low contribution of pump-induced effects compared to light scattered from the interface roughness, which makes the measured diffraction signal go negative. As a result, the overall shape of the diffracted signal looks different.

7.4 Conclusion

We have shown that it is possible to detect gratings with peak-to-valley amplitudes as small as 0.5 nm, underneath a 130 nm thick Ni layer, using laser-induced ultrasound. The diffraction of the probe pulse is due to displacement of the interface, the strain-optic effect, and the thermo-optic effect. Our model accurately predicts the shape of the time-dependent diffracted signal, and we explain how the shape of the measured signal is affected by the different physical effects. The light scattered from the interface due to roughness (<307 pm RMS) plays a very important role in understanding the measurements as the scattered optical electric field adds coherently to the optical fields diffracted by the acoustic waves. Scattered light should be taken into account when the strength of the diffracted probe light is comparable to that of the scattered light.

Bibliography

[1] "Computers in spaceflight: The NASA experience," https://history.nasa.gov/computers/Ch2-5.html. Accessed: 2020-02-13: 2020-02-13.

[2] H. J. Levinson, *Principles of lithography* (SPIE Bellingham, WA, 2005).

[3] G. E. Moore, "Cramming more components onto integrated circuits," IEEE Solid-State Circuits Society Newsletter **11**, 33–35 (2006).

[4] G. E. Moore, "Progress in digital integrated electronics," IEEE Solid-State Circuits Society Newsletter **11**, 36–37 (2006).

[5] C. A. Mack, "Fifty years of moore's law," IEEE Transactions on Semiconductor Manufacturing **24**, 202–207 (2011).

[6] "Technological progress," https://ourworldindata.org/technological-progress. Accessed: 2020-02-13.

[7] "7nm technology," https://www.tsmc.com/english/dedicatedFoundry/technology/7nm.htm. Accessed: 2020-02-13.

[8] "An introduction to photolithography imaging," https://staticwww.asml.com/doclib/productandservices/images/2007/Spring/Articles/Images_Spring_Edit_2007{\%}2020-22.pdf. Accessed: 2020-02-13.

[9] C. Wagner and N. Harned, "Lithography gets extreme," Nature Photonics **4**, 24–26 (2010).

[10] H. Wakabayashi, S. Yamagami, N. Ikezawa, A. Ogura, M. Narihiro, K. Arai, Y. Ochiai, K. Takeuchi, T. Yamamoto, and T. Mogami, "Sub-10-nm planar-bulk-CMOS devices using lateral junction control," IEEE International Electron Devices Meeting pp. 20.7.1–20.7.3 (2003).

[11] "TSMC and OIP ecosystem partners deliver industry's first complete design infrastructure for 5nm process technology," `https://www.tsmc.com/tsmcdotcom/PRListingNewsAction.do?action=detail&language=E&newsid=THPGWQTHTH`. Accessed: 2020-02-13.

[12] A. J. den Boef, "Optical wafer metrology sensors for process-robust CD and overlay control in semiconductor device manufacturing," Surface Topography: Metrology and Properties **4**, 023001 (2016).

[13] J. Alsmeier, "Ultrahigh density vertical nand memory device," (2012). US Patent 8,198,672.

[14] H. Kim, S.-J. Ahn, Y. G. Shin, K. Lee, and E. Jung, "Evolution of nand flash memory: From 2D to 3D as a storage market leader," 2017 IEEE International Memory Workshop (IMW), Monterey, CA pp. 1–4 (2017).

[15] D. Resnati, A. Goda, G. Nicosia, C. Miccoli, A. S. Spinelli, and C. M. Compagnoni, "Temperature effects in nand flash memories: A comparison between 2-d and 3-d arrays," IEEE Electron Device Letters **38**, 461–464 (2017).

[16] J.-M. Han, "Architecture and method for nand flash memory," (2008). US Patent 7,372,715.

[17] N. Mokhlesi and R. Scheuerlein, "Three dimensional nand memory," (2010). US Patent 7,851,851.

[18] H. Zhang, A. Antoncecchi, S. Edward, I. Setija, P. Planken, and S. Witte, "Unraveling phononic, optoacoustic, and mechanical properties of metals with light-driven hypersound," Phys. Rev. Applied **13**, 014010 (2020).

[19] S. Anisimov, B. Kapeliovich, and T. Perel-man, "Electron emission from metal surfaces exposed to ultrashort laser pulses," Journal of Experimental and Theoretical Physics **66**, 375–377 (1974).

[20] J. Güdde, J. Hohlfeld, J. Müller, and E. Matthias, "Damage threshold dependence on electron–phonon coupling in Au and Ni films," Applied Surface Science **127-129**, 40–45 (1998).

[21] J. Hohlfeld, S.-S. Wellershoff, J. Güdde, U. Conrad, V. Jähnke, and E. Matthias, "Electron and lattice dynamics following optical excitation of metals," Chemical Physics **251**, 237–258 (2000).

[22] M. Bonn, D. N. Denzler, S. Funk, M. Wolf, S.-S. Wellershoff, and J. Hohlfeld, "Ultrafast electron dynamics at metal surfaces: Competition between electron-phonon coupling and hot-electron transport," Phys. Rev. B **61**, 1101–1105 (2000).

[23] S.-S. Wellershoff, J. Hohlfeld, J. Güdde, and E. Matthias, "The role of electron-phonon coupling in femtosecond laser damage of metals," Applied Physics A **69**, S99–S107 (1999).

[24] C. Suárez, W. E. Bron, and T. Juhasz, "Dynamics and transport of electronic carriers in thin gold films," Phys. Rev. Lett. **75**, 4536–4539 (1995).

[25] M. C. Troparevsky, A. S. Sabau, A. R. Lupini, and Z. Zhang, "Transfer-matrix formalism for the calculation of optical response in multilayer systems: from coherent to incoherent interference," Opt. Express **18**, 24715–24721 (2010).

[26] C. C. Katsidis and D. I. Siapkas, "General transfer-matrix method for optical multilayer systems with coherent, partially coherent, and incoherent interference," Appl. Opt. **41**, 3978–3987 (2002).

[27] T. Qiu and C. Tien, "Heat transfer mechanisms during short-pulse laser heating of metals," Journal of Heat Transfer **115:4**, 835–841 (1993).

[28] J. E. B. J. K. Chen, "Numerical study of ultrashort laser pulse interactions with metal films," Numerical Heat Transfer, Part A: Appli-

cations **40**, 1–20 (2001).

[29] C. Thomsen, H. T. Grahn, H. J. Maris, and J. Tauc, "Surface generation and detection of phonons by picosecond light pulses," Phys. Rev. B **34**, 4129–4138 (1986).

[30] O. B. Wright, "Ultrafast nonequilibrium stress generation in gold and silver," Phys. Rev. B **49**, 9985–9988 (1994).

[31] P. M. Shearer, *Introduction to Seismology* (Cambridge University Press, New York, 2002).

[32] R. D. Blandford and K. S. Thorne, *Applications of Classical Physics* (Stanford University and California Institute of Technology, 2013).

[33] J. H. Ferziger and M. Peric, *Computational Methods for Fluid Dynamics* (Springer, 2002).

[34] K. Naugolnykh and L. Ostrovsky, *Nonlinear Wave Processes in Acoustics* (Cambridge University Press, 1998).

[35] B. C. Daly, K. Kang, Y. Wang, and D. G. Cahill, "Picosecond ultrasonic measurements of attenuation of longitudinal acoustic phonons in silicon," Phys. Rev. B **80**, 174112 (2009).

[36] D. Li and D. G. Cahill, "Attenuation of 7 GHz surface acoustic waves on silicon," Phys. Rev. B **94**, 104306 (2016).

[37] A. Devos, M. Foret, S. Ayrinhac, P. Emery, and B. Rufflé, "Hypersound damping in vitreous silica measured by picosecond acoustics," Phys. Rev. B **77**, 100201 (2008).

[38] A. Devos and C. Lerouge, "Evidence of laser-wavelength effect in picosecond ultrasonics: Possible connection with interband transitions," Phys. Rev. Lett. **86**, 2669–2672 (2001).

[39] J. J. Kasinski, L. Gomez-Jahn, K. J. Leong, S. M. Gracewski, and R. J. D. Miller, "Optical generation of coherent surface acoustics: an optically based probe of surface structure and dynamics," Opt. Lett. **13**, 710–712 (1988).

[40] T. F. Crimmins, A. A. Maznev, and K. A. Nelson, "Transient grating

measurements of picosecond acoustic pulses in metal films," Appl. Phys. Lett. **74**, 1344–1346 (1999).

[41] P. J. S. van Capel and J. I. Dijkhuis, "Time-resolved interferometric detection of ultrashort strain solitons in sapphire," Phys. Rev. B **81**, 144106 (2010).

[42] T. Saito, O. Matsuda, and O. B. Wright, "Picosecond acoustic phonon pulse generation in nickel and chromium," Phys. Rev. B **67**, 205421 (2003).

[43] M. Born and E. Wolf, *Principles of Optics* (Cambridge University Press, 1999).

[44] J. W. Goodman, *Introduction to Fourier optics* (Roberts & Co. Publishers, 2005).

[45] H. J. Eichler and A. Hermerschmidt, *Light-Induced Dynamic Gratings and Photorefraction* (Springer New York, 2006).

[46] S. Edward, A. Antoncecchi, H. Zhang, H. Sielcken, S. Witte, and P. C. M. Planken, "Detection of periodic structures through opaque metal layers by optical measurements of ultrafast electron dynamics," Opt. Express **26**, 23380–23396 (2018).

[47] M. Aeschlimann, M. Bauer, S. Pawlik, W. Weber, R. Burgermeister, D. Oberli, and H. C. Siegmann, "Ultrafast spin-dependent electron dynamics in fcc co," Phys. Rev. Lett. **79**, 5158–5161 (1997).

[48] S. D. Brorson, J. G. Fujimoto, and E. P. Ippen, "Femtosecond electronic heat-transport dynamics in thin gold films," Phys. Rev. Lett. **59**, 1962–1965 (1987).

[49] C.-K. Sun, F. Vallée, L. H. Acioli, E. P. Ippen, and J. G. Fujimoto, "Femtosecond-tunable measurement of electron thermalization in gold," Phys. Rev. B **50**, 15337–15348 (1994).

[50] C.-K. Sun, F. Vallée, L. Acioli, E. P. Ippen, and J. G. Fujimoto, "Femtosecond investigation of electron thermalization in gold," Phys. Rev. B **48**, 12365–12368 (1993).

[51] T. Avanesian and P. Christopher, "Adsorbate specificity in hot electron driven photochemistry on catalytic metal surfaces," The Journal of Physical Chemistry C **118**, 28017–28031 (2014).

[52] J. Gadzuk, "Hot-electron femtochemistry at surfaces: on the role of multiple electron processes in desorption," Chemical Physics **251**, 87 – 97 (2000).

[53] P. B. Corkum, F. Brunel, N. K. Sherman, and T. Srinivasan-Rao, "Thermal response of metals to ultrashort-pulse laser excitation," Phys. Rev. Lett. **61**, 2886–2889 (1988).

[54] G. K. P. Ramanandan, G. Ramakrishnan, N. Kumar, A. J. L. Adam, and P. C. M. Planken, "Emission of terahertz pulses from nanostructured metal surfaces," Journal of Physics D: Applied Physics **47**, 374003 (2014).

[55] G. Ramakrishnan and P. C. M. Planken, "Percolation-enhanced generation of terahertz pulses by optical rectification on ultrathin gold films," Opt. Lett. **36**, 2572–2574 (2011).

[56] F. Kadlec, P. Kužel, and J.-L. Coutaz, "Optical rectification at metal surfaces," Opt. Lett. **29**, 2674–2676 (2004).

[57] F. Kadlec, P. Kužel, and J.-L. Coutaz, "Study of terahertz radiation generated by optical rectification on thin gold films," Opt. Lett. **30**, 1402–1404 (2005).

[58] W. S. Fann, R. Storz, H. W. K. Tom, and J. Bokor, "Direct measurement of nonequilibrium electron-energy distributions in subpicosecond laser-heated gold films," Phys. Rev. Lett. **68**, 2834–2837 (1992).

[59] W. S. Fann, R. Storz, H. W. K. Tom, and J. Bokor, "Electron thermalization in gold," Phys. Rev. B **46**, 13592–13595 (1992).

[60] T. Juhasz, H. E. Elsayed-Ali, G. O. Smith, C. Suárez, and W. E. Bron, "Direct measurements of the transport of nonequilibrium electrons in gold films with different crystal structures," Phys. Rev. B **48**, 15488–15491 (1993).

[61] J. Hohlfeld, J. Müller, S.-S. Wellershoff, and E. Matthias, "Time-

resolved thermoreflectivity of thin gold films and its dependence on film thickness," Applied Physics B: Lasers and Optics **64**, 387–390 (1997).

[62] J. Hohlfeld, D. Grosenick, U. Conrad, and E. Matthias, "Femtosecond time-resolved reflection second-harmonic generation on polycrystalline copper," Applied Physics A **60**, 137–142 (1995).

[63] S. D. Brorson, A. Kazeroonian, J. S. Moodera, D. W. Face, T. K. Cheng, E. P. Ippen, M. S. Dresselhaus, and G. Dresselhaus, "Femtosecond room-temperature measurement of the electron-phonon coupling constant γ in metallic superconductors," Phys. Rev. Lett. **64**, 2172–2175 (1990).

[64] J. L. Hostetler, A. N. Smith, D. M. Czajkowsky, and P. M. Norris, "Measurement of the electron-phonon coupling factor dependence on film thickness and grain size in Au, Cr, and Al," Appl. Opt. **38**, 3614–3620 (1999).

[65] P. E. Hopkins and P. M. Norris, "Substrate influence in electron–phonon coupling measurements in thin Au films," Applied Surface Science **253**, 6289 – 6294 (2007).

[66] T. Juhasz, H. E. Elsayed-Ali, X. H. Hu, and W. E. Bron, "Time-resolved thermoreflectivity of thin gold films and its dependence on the ambient temperature," Phys. Rev. B **45**, 13819–13822 (1992).

[67] W. M. Ibrahim, H. E. Elsayed-Ali, C. E. Bonner, and M. Shinn, "Ultrafast investigation of electron dynamics in multi-layer metals," International Journal of Heat and Mass Transfer **47**, 2261 – 2268 (2004).

[68] J. Guo, T. Wang, D. Wang, J. Shao, A. Chen, and M. Jin, "Simulation of thermionic emission optimization in femtosecond laser irradiation metal film by two-layer structure," Applied Physics A **117**, 1367–1374 (2014).

[69] A. Chen, L. Sui, Y. Shi, Y. Jiang, D. Yang, H. Liu, M. Jin, and D. Ding, "Ultrafast investigation of electron dynamics in the gold-coated two-layer metal films," Thin Solid Films **529**, 209 – 216 (2013).

[70] R. H. M. Groeneveld, R. Sprik, and A. Lagendijk, "Effect of a nonthermal electron distribution on the electron-phonon energy relaxation process in noble metals," Phys. Rev. B **45**, 5079–5082 (1992).

[71] T. Qiu and C. Tien, "Short-pulse laser heating on metals," International Journal of Heat and Mass Transfer **35**, 719 – 726 (1992).

[72] A. N. Smith and P. M. Norris, "Influence of intraband transitions on the electron thermoreflectance response of metals," Appl. Phys. Lett. **78**, 1240–1242 (2001).

[73] P. E. Hopkins, J. L. Kassebaum, and P. M. Norris, "Effects of electron scattering at metal-nonmetal interfaces on electron-phonon equilibration in gold films," Journal of Applied Physics **105**, 023710 (2009).

[74] G. D. Tsibidis, "Thermal response of double-layered metal films after ultrashort pulsed laser irradiation: The role of nonthermal electron dynamics," Appl. Phys. Lett. **104**, 051603 (2014).

[75] W. Wang and D. G. Cahill, "Limits to thermal transport in nanoscale metal bilayers due to weak electron-phonon coupling in Au and Cu," Phys. Rev. Lett. **109**, 175503 (2012).

[76] A. M. Chen, Y. F. Jiang, L. Z. Sui, H. Liu, M. X. Jin, and D. J. Ding, "Thermal analysis of double-layer metal films during femtosecond laser heating," Journal of Optics **13**, 055503 (2011).

[77] G.-M. Choi, R. B. Wilson, and D. G. Cahill, "Indirect heating of Pt by short-pulse laser irradiation of Au in a nanoscale Pt/Au bilayer," Phys. Rev. B **89**, 064307 (2014).

[78] A. Chen, H. Xu, Y. Jiang, L. Sui, D. Ding, H. Liu, and M. Jin, "Modeling of femtosecond laser damage threshold on the two-layer metal films," Applied Surface Science **257**, 1678 – 1683 (2010).

[79] A. Guerra III, W. Bron, and C. Suárez, "Imaging metallic multilayer structures through ultrafast optically driven excited electron transport," Applied Physics B **68**, 405–409 (1999).

[80] M. Perner, P. Bost, U. Lemmer, G. von Plessen, J. Feldmann, U. Becker, M. Mennig, M. Schmitt, and H. Schmidt, "Optically in-

duced damping of the surface plasmon resonance in gold colloids," Phys. Rev. Lett. **78**, 2192–2195 (1997).

[81] H. E. Elsayed-Ali, T. B. Norris, M. A. Pessot, and G. A. Mourou, "Time-resolved observation of electron-phonon relaxation in copper," Phys. Rev. Lett. **58**, 1212–1215 (1987).

[82] Z. Lin, L. V. Zhigilei, and V. Celli, "Electron-phonon coupling and electron heat capacity of metals under conditions of strong electron-phonon nonequilibrium," Phys. Rev. B **77**, 075133 (2008).

[83] P. B. Johnson and R. W. Christy, "Optical constants of the noble metals," Phys. Rev. B **6**, 4370–4379 (1972).

[84] R. H. M. Groeneveld, R. Sprik, and A. Lagendijk, "Femtosecond spectroscopy of electron-electron and electron-phonon energy relaxation in Ag and Au," Phys. Rev. B **51**, 11433–11445 (1995).

[85] H. E. Elsayed-Ali, T. Juhasz, G. O. Smith, and W. E. Bron, "Femtosecond thermoreflectivity and thermotransmissivity of polycrystalline and single-crystalline gold films," Phys. Rev. B **43**, 4488–4491 (1991).

[86] P. Ruello and V. E. Gusev, "Physical mechanisms of coherent acoustic phonons generation by ultrafast laser action," Ultrasonics **56**, 21 – 35 (2015).

[87] T. Dehoux, N. Chigarev, C. Rossignol, and B. Audoin, "Effect of lateral electronic diffusion on acoustic diffraction in picosecond ultrasonics," Phys. Rev. B **77**, 214307 (2008).

[88] O. Matsuda, M. C. Larciprete, R. L. Voti, and O. B. Wright, "Fundamentals of picosecond laser ultrasonics," Ultrasonics **56**, 3 – 20 (2015).

[89] P. van Capel, E. Péronne, and J. Dijkhuis, "Nonlinear ultrafast acoustics at the nano scale," Ultrasonics **56**, 36 – 51 (2015).

[90] A. Devos, "Colored ultrafast acoustics: From fundamentals to applications," Ultrasonics **56**, 90 – 97 (2015).

[91] O. B. Wright and K. Kawashima, "Coherent phonon detection from ultrafast surface vibrations," Phys. Rev. Lett. **69**, 1668–1671 (1992).

[92] C. J. K. Richardson, M. J. Ehrlich, and J. W. Wagner, "Interferometric detection of ultrafast thermoelastic transients in thin films:theory with supporting experiment," J. Opt. Soc. Am. B **16**, 1007–1015 (1999).

[93] V. Gusev, "Generation of inhomogeneous bulk plane acoustic modes by laser-induced thermoelastic grating near mechanically free surface," Journal of Applied Physics **107**, 114906 (2010).

[94] M. Kouyaté, T. Pezeril, V. Gusev, and O. Matsuda, "Theory for optical detection of picosecond shear acoustic gratings," J. Opt. Soc. Am. B **33**, 2634–2648 (2016).

[95] R. M. Slayton and K. A. Nelson, "Picosecond acoustic transmission measurements. i. transient grating generation and detection of acoustic responses in thin metal films," The Journal of Chemical Physics **120**, 3908–3918 (2004).

[96] V. Gusev, "On generation of picosecond inhomogeneous shear strain fronts by laser-induced gratings," Appl. Phys. Lett. **94**, 164105 (2009).

[97] O. B. Wright and V. E. Gusev, "Acoustic generation in crystalline silicon with femtosecond optical pulses," Appl. Phys. Lett. **66**, 1190–1192 (1995).

[98] T. Saito, O. Matsuda, M. Tomoda, and O. B. Wright, "Imaging gigahertz surface acoustic waves through the photoelastic effect," J. Opt. Soc. Am. B **27**, 2632–2638 (2010).

[99] R. M. Slayton, K. A. Nelson, and A. A. Maznev, "Transient grating measurements of film thickness in multilayer metal films," Journal of Applied Physics **90**, 4392–4402 (2001).

[100] M. Lejman, V. Shalagatskyi, O. Kovalenko, T. Pezeril, V. V. Temnov, and P. Ruello, "Ultrafast optical detection of coherent acoustic phonons emission driven by superdiffusive hot electrons," J. Opt. Soc.

Am. B **31**, 282 (2014).

[101] K. E. O'Hara, X. Hu, and D. G. Cahill, "Characterization of nanostructured metal films by picosecond acoustics and interferometry," Journal of Applied Physics **90**, 4852–4858 (2001).

[102] D. Yarotski, E. Fu, L. Yan, Q. Jia, Y. Wang, A. J. Taylor, and B. P. Uberuaga, "Characterization of irradiation damage distribution near TiO_2/$PSrTiO_3$ interfaces using coherent acoustic phonon interferometry," Appl. Phys. Lett. **100**, 251603 (2012).

[103] A. Steigerwald, Y. Xu, J. Qi, J. Gregory, X. Liu, J. K. Furdyna, K. Varga, A. B. Hmelo, G. Lüpke, L. C. Feldman, and N. Tolk, "Semiconductor point defect concentration profiles measured using coherent acoustic phonon waves," Appl. Phys. Lett. **94**, 111910 (2009).

[104] T. Dehoux, K. Ishikawa, P. H. Otsuka, M. Tomoda, O. Matsuda, M. Fujiwara, S. Takeuchi, I. A. Veres, V. E. Gusev, and O. B. Wright, "Optical tracking of picosecond coherent phonon pulse focusing inside a sub-micron object," Light: Science & Applications **5**, e16082 (2016).

[105] K. A. Nelson, R. J. D. Miller, D. R. Lutz, and M. D. Fayer, "Optical generation of tunable ultrasonic waves," Journal of Applied Physics **53**, 1144–1149 (1982).

[106] C. Klieber, E. Peronne, K. Katayama, J. Choi, M. Yamaguchi, T. Pezeril, and K. A. Nelson, "Narrow-band acoustic attenuation measurements in vitreous silica at frequencies between 20 and 400 GHz," Appl. Phys. Lett. **98**, 211908 (2011).

[107] T. Pezeril, P. Ruello, S. Gougeon, N. Chigarev, D. Mounier, J.-M. Breteau, P. Picart, and V. Gusev, "Generation and detection of plane coherent shear picosecond acoustic pulses by lasers: Experiment and theory," Phys. Rev. B **75**, 174307 (2007).

[108] P. Babilotte, P. Ruello, D. Mounier, T. Pezeril, G. Vaudel, M. Edely, J.-M. Breteau, V. Gusev, and K. Blary, "Femtosecond laser generation and detection of high-frequency acoustic phonons in gaas semiconductors," Phys. Rev. B **81**, 245207 (2010).

[109] I.-J. Chen, P.-A. Mante, C.-K. Chang, S.-C. Yang, H.-Y. Chen, Y.-R. Huang, L.-C. Chen, K.-H. Chen, V. Gusev, and C.-K. Sun, "Graphene-to-substrate energy transfer through out-of-plane longitudinal acoustic phonons," Nano Letters **14**, 1317–1323 (2014).

[110] B. Bonello, B. Perrin, E. Romatet, and J. Jeannet, "Application of the picosecond ultrasonic technique to the study of elastic and time-resolved thermal properties of materials," Ultrasonics **35**, 223 – 231 (1997).

[111] F. Pérez-Cota, R. J. Smith, E. Moradi, L. Marques, K. F. Webb, and M. Clark, "High resolution 3D imaging of living cells with sub-optical wavelength phonons," Scientific Reports **6**, 1–11 (2016).

[112] D. H. Hurley and O. B. Wright, "Detection of ultrafast phenomena by use of a modified Sagnac interferometer," Opt. Lett. **24**, 1305–1307 (1999).

[113] G. Tas and H. J. Maris, "Electron diffusion in metals studied by picosecond ultrasonics," Phys. Rev. B **49**, 15046–15054 (1994).

[114] O. Wright and V. Gusev, "Ultrafast acoustic phonon generation in gold," Physica B: Condensed Matter **219-220**, 770 – 772 (1996).

[115] K. E. O'Hara, X. Hu, and D. G. Cahill, "Characterization of nanostructured metal films by picosecond acoustics and interferometry," Journal of Applied Physics **90**, 4852–4858 (2001).

[116] O. B. Wright, "Thickness and sound velocity measurement in thin transparent films with laser picosecond acoustics," Journal of Applied Physics **71**, 1617–1629 (1992).

[117] C. Thomsen, H. Grahn, H. Maris, and J. Tauc, "Picosecond interferometric technique for study of phonons in the brillouin frequency range," Optics Communications **60**, 55 – 58 (1986).

[118] H. T. Grahn, H. J. Maris, and J. Tauc, "Picosecond ultrasonics," IEEE Journal of Quantum Electronics **25**, 2562–2569 (1989).

[119] O. B. Wright and T. Hyoguchi, "Ultrafast vibration and laser acoustics in thin transparent films," Opt. Lett. **16**, 1529–1531 (1991).

[120] T. Požar, A. Babnik, and J. Možina, "From laser ultrasonics to optical manipulation," Opt. Express **23**, 7978–7990 (2015).

[121] P. Ruello, T. Pezeril, S. Avanesyan, G. Vaudel, V. Gusev, I. C. Infante, and B. Dkhil, "Photoexcitation of gigahertz longitudinal and shear acoustic waves in $BiFeO_3$ multiferroic single crystal," Appl. Phys. Lett. **100**, 212906 (2012).

[122] P. B. Johnson and R. W. Christy, "Optical constants of transition metals: Ti, V, Cr, Mn, Fe, Co, Ni, and Pd," Phys. Rev. B **9**, 5056–5070 (1974).

[123] S. Edward, H. Zhang, I. Setija, V. Verrina, A. Antoncecchi, S. Witte, and P. Planken, "Detection of hidden gratings through multilayer nanostructures using light and sound," arXiv:1911.08337 (2019).

[124] H. N. Lin, R. J. Stoner, H. J. Maris, and J. Tauc, "Phonon attenuation and velocity measurements in transparent materials by picosecond acoustic interferometry," Journal of Applied Physics **69**, 3816–3822 (1991).

[125] A. Devos, R. Côte, G. Caruyer, and A. Lefèvre, "A different way of performing picosecond ultrasonic measurements in thin transparent films based on laser-wavelength effects," Appl. Phys. Lett. **86**, 211903 (2005).

[126] O. Matsuda, T. Pezeril, I. Chaban, K. Fujita, and V. Gusev, "Time-domain brillouin scattering assisted by diffraction gratings," Phys. Rev. B **97**, 064301 (2018).

[127] V. E. Gusev and P. Ruello, "Advances in applications of time-domain brillouin scattering for nanoscale imaging," Applied Physics Reviews **5**, 031101 (2018).

[128] S. M. Nikitin, N. Chigarev, V. Tournat, A. Bulou, D. Gasteau, B. Castagnede, A. Zerr, and V. E. Gusev, "Revealing sub-mm and mm-scale textures in H_2O ice at megabar pressures by time-domain brillouin scattering," Scientific Reports **5**, 9352 (2015).

[129] A. Stovas and B. Ursin, "Equivalent time-average and effective

medium for periodic layers," Geophysical Prospecting **55**, 871–882 (2007).

[130] I. H. Malitson, "Interspecimen comparison of the refractive index of fused silica," J. Opt. Soc. Am. **55**, 1205–1209 (1965).

[131] K. Luke, Y. Okawachi, M. R. E. Lamont, A. L. Gaeta, and M. Lipson, "Broadband mid-infrared frequency comb generation in a si3n4 microresonator," Opt. Lett. **40**, 4823–4826 (2015).

[132] J. C. Stover, *Vector scattering theory* (SPIE Press, 1995).

[133] J. M. Elson and J. M. Bennett, "Vector Scattering Theory," Optical Engineering **18**, 116 – 124 (1979).

[134] S. O. Rice, "Reflection of electromagnetic waves from slightly rough surfaces," Communications on Pure and Applied Mathematics **4**, 351–378 (1951).

[135] S. Schröder, A. Duparré, L. Coriand, A. Tünnermann, D. H. Penalver, and J. E. Harvey, "Modeling of light scattering in different regimes of surface roughness," Opt. Express **19**, 9820–9835 (2011).

[136] T. V. Vorburger, E. Marx, and T. R. Lettieri, "Regimes of surface roughness measurable with light scattering," Appl. Opt. **32**, 3401–3408 (1993).

[137] T. D. B. Jacobs, T. Junge, and L. Pastewka, "Quantitative characterization of surface topography using spectral analysis," Surface Topography: Metrology and Properties **5**, 013001 (2017).

Summary

Detection of hidden gratings using light and sound

The ambition to stay in trajectory with Moore's Law has pushed the semiconductor industry to introduce a radical new design of memory chips called "3D-NAND" memory. During the fabrication of "3D-NAND" memory, it is often necessary to optically detect the presence of micro/nano structures buried underneath many dielectric and metallic layers. An example of suc a buried structure is a so-called alignment grating, which is a grating etched in Si. When light is diffracted off such a grating, a small change in position of the wafer changes the phase difference between the -1^{st} and $+1^{\text{st}}$ order diffracted light beams, which can be used to determine the position of the wafer with sub-nanometer accuracy. However, when optically opaque dielectric and metallic layers are deposited on top of these gratings, it becomes impossible to detect them using visible/IR light. Fortunately, materials that are opaque to visible/IR light are often transparent to sound.

In this thesis, the use of laser-induced ultrasound waves is proposed to detect hidden alignment gratings. We fabricated metal gratings on top of flat layers of metal/dielectric layers on a glass substrate and performed pump-probe experiments from the substrate side. Hence, both the 400 nm pump pulse and the 800 nm probe pulse see a nominally flat surface, and the grating is effectively optically hidden. The femtosecond pump pulse generates an acoustic wave in the metal layer that propagates through the metal/dielectric layers and reflects off the buried grating. The acoustic wavefront returning to the metal-glass interface now has a shape resembling that of the buried grating. This gives rise to a 'grating-shaped' deforma-

tion of the metal-glass interface. A delayed probe pulse diffracts from this imprinted grating, and the diffracted signal is observed. The observation of a diffraction signal indicates that we can detect the presence of a buried grating using the pump-probe technique.

The results of this thesis can be divided into three parts. The first part, consisting of Chapters 4 and 5, focuses on the generation of acoustic waves. The first step in the generation of extremely-high frequency acoustic waves is the absorption of light by the free-electron gas. The subsequent thermalization, cooling of the electron gas together with the electron energy diffusion, are essential ingredients to determine where the absorbed laser energy is transformed into lattice heat. In Chapter 4, measurements and calculations of electron dynamics in single metallic layers and in metallic bilayer upon excitation with a femtosecond laser pulse are shown. It was observed that the electron dynamics is strongly influenced by the thickness of the metal and by the strength of the electron-phonon coupling. These effects were then used to determine the presence and nature of a metal grating buried below an optically opaque gold layer. In Chapter 5, the measurements and calculations of transient-grating pump-probe experiments on flat metal layers are discussed. It was shown that it is possible to launch a grating-shaped acoustic wave in flat metal layers by means of transient-grating pump pulses, and that a probe pulse can diffract from the grating-shaped acoustic wave.

The second part of this thesis primarily focuses on the propagation of acoustic waves through metals and dielectrics, and the ability of laser-induced ultrasound to detect gratings buried below multilayers. It was shown in Chapter 6 that the high-frequency acoustic wave can propagate through a stack of tens of 18 nm thick SiO_2 and Si_3N_4 layers, reflect off the buried grating, and give rise to probe pulse diffraction from the grating-shaped acoustic echo. The shape and strength of the time-dependent diffraction signal can be accurately predicted using an elaborate numerical model. The diffracted signal strength is not strongly influenced by the number of dielectric layers through which the acoustic wave has to propagate, and the acoustic wave "sees" the SiO_2 and Si_3N_4 stack as an equivalent time-averaged acoustic medium.

The third and final part focuses on the detection of acoustic waves, and the limits of the photoacoustic technique are explored. In Chapter 7, pump-probe measurements on samples with buried gratings with amplitudes as small as 1 nm are shown. It was observed that probe light scattering from interface roughness constructively or destructively interferes with the light diffracted from the grating-shaped acoustic echoes. This drastically affects the shape and strength of the time-dependent diffracted signal. The intensity of the scattered light was quantified using Rayleigh-Rice scattering theory and later used to simulate the shape of the diffracted signals.

I have shown that pump-probe laser-induced ultrasound shows promise as a new, non-contact, all-optical grating detection- and imaging-modality for wafer alignment applications by using ultrasound to make an acoustic copy of the buried grating, while using conventional optical diffraction to read-out the copy when it reaches the surface.

Samenvatting

Verborgen uitlijntralies meten met licht en geluid

The ambitie om Moore's Law voort te zetten heeft in de halfgeleiderindustrie geleid tot het introduceren van een radicaal nieuw type flashgeheugen, genaamd '3D-NAND'. Tijdens de fabricage van een "3D-NAND" geheugenchip is het vaak nodig om op optische wijze micro/nano structuren te detecteren. Deze structuren zijn vaak bedekt met meerdere lagen van een diëlektricum of een metaallaag. Een voorbeeld van zo'n bedekte structuur is een zogeheten uitlijntralie geëtst in een Si wafer. Als een lichtbundel dit tralie belicht zal een kleine verandering in de positie van de wafer een verandering van het optische faseverschil tussen de -1^e en +1^e orde diffractiebundels tot gevolg hebben. Deze verandering van het faseverschil kan gebruikt worden om de positie van de wafer te bepalen met sub-nanometer precisie. Echter, wanneer ondoorzichtige lagen van een metaal of een diëlektricum op dit uitlijntralie worden gedeponeerd, wordt het onmogelijk om deze te detecteren met zichtbaar/IR licht. Gelukkig zijn materialen die onzichtbaar zijn voor zichtbaar/IR licht vaak transparant voor geluidsgolven. In dit proefschrift wordt het gebruik van laser-geïnduceerde ultrasone geluidsgolven voorgesteld als methode voor het detecteren van verborgen uitlijntralies. Om dit te testen hebben we metalen tralies gefabriceerd bovenop vlakke lagen van een metaal en diëlektrica op een substraat van glas. Vervolgens hebben we 'pomp-probe' experimenten uitgevoerd vanaf de substraatkant. In deze configuratie 'zien' zowel de 400 nm pomppuls als de 800 nm probepuls een vlak oppervlak en is het tralie optisch verborgen. De femtoseconde pomppuls lanceert een geluidsgolf in de metaallaag die zich voortplant door het metaal en de diëlektrische lagen. Aangekomen bij het

verborgen tralie zal de geluidsgolf reflecteren en terugkeren naar het glazen substraat. Het golffront van de gereflecteerde geluidsgolf heeft na reflectie een vorm vergelijkbaar met dat van het tralie. Wanneer deze geluidsgolf het grensvlak tussen de metaallaag en het glazen substraat bereikt, zal het deze daardoor verstoren met een zelfde ruimtelijke periode. Deze modificatie van het grensvlak functioneert vervolgens zelf als een tralie voor een vertraagde probepuls die dit tralie belicht. De diffractie van de probepuls aan dit tralie kan vervolgens worden gedetecteerd en markeert de aanwezigheid van het oorspronkelijke verborgen tralie. De resultaten beschreven in dit proefschrift kunnen worden onderverdeeld in drie delen. Deel één omvat Hoofdstuk 4 en 5, en focust op het genereren van geluidsgolven. De eerste stap in de generatie van geluidsgolven met extreem hoge frequenties is de absorptie van lichtpulsen door het vrije-elektronengas. Een beschrijving van de daarop volgende thermalisatie, d.w.z. het afkoelen van het elektronengas en de elektronenergiediffusie, is essentieel om te achterhalen waar de geabsorbeerde laser energy overgaat in opwarming van het atoomrooster. In Hoofdstuk 4 word de elektrondynamica, die plaatsvindt na excitatie door een femtoseconde laserpuls, voor zowel een enkele als een dubbele metaallaag, beschreven door middel van metingen en berekeningen. We constateren dat de elektrondynamica sterk afhangt van de dikte van de metaallaag en van de koppeling tussen de elektronen en de fononen. Aansluitend wordt deze kennis gebruikt om de aanwezigheid en het karakter van een metalen tralie, bedekt onder een ondoorzichtbare laag goud, te bepalen. In Hoofdstuk 5 worden metingen en berekeningen aan transiente-tralies in pomp-probe experimenten, behandeld. In deze experimenten wordt een geluidsgolf met de vorm van een tralie gelanceerd in vlakke metaallagen door gebruik te maken van twee, onder een hoek interfererende, pomppulsen. Er word aangetoond dat een probepuls diffracteert aan de tralies veroorzaakt door meerdere akoestische echo's die terugkeren naar het oppervlak. Het tweede deel van dit proefschrift gaat voornamelijk over de voortplanting van geluidsgolven door metalen en diëlektrica, en het detecteren van tralies bedekt onder meerdere lagen, gebruik makend van ultrasone geluidsgolven. In Hoofdstuk 6 word aangetoond dat een hoogfrequente geluidsgolf zich kan voortplanten door enkele tientallen lagen SiO_2 en Si_3N_4 van 18 nm dik, vervolgens reflecteert aan het bedekte tralie, en als tralie-vormige echo diffractie van een probepuls kan veroorza-

ken. De vorm en intensiteit van het tijdsafhankelijke diffractiesignaal kan nauwkeurig worden voorspeld door een uitgebreid numeriek model. De intensiteit van het diffractiesignaal is niet sterk afhankelijk van het aantal diëlectrische lagen waar de geluidsgolf zich door voortplant. Verder blijkt dat de gestapelde SiO_2 en Si_3N_4 lagen kunnen worden beschreven als een enkele laag met een effectieve dikte en met materiaal eigenschappen die tussen die van SiO_2 en Si_3N_4 inliggen. Het derde en laatste deel behandelt de detectie van geluidsgolven en verkent de limieten van de fotoakoestische techniek. In Hoofdstuk 7 worden pomp-probe metingen beschreven aan bedekte tralies met amplitudes in de orde van een enkele nanometer. We hebben gevonden dat probe licht dat verstrooit aan grensvlakoneffenheden, constructief of destructief kan interfereren met de diffractie afkomstig van de tralie-vormige geluidsgolf. Dit heeft een sterke verandering van de vorm en intensiteit van het tijdsafhankelijke diffractiesignaal tot gevolg. De intensiteit van het verstrooide licht kan gekwantificeerd worden met behulp van de Rayleigh-Rice theorie en naderhand worden gebruikt om de vorm van het diffractiesignaal te simuleren. Ik heb laten zien dat pomp-probe, laser-geïnduceerd ultrageluid potentie heeft als een nieuwe, contactloze en volledig optische tralie-detectie- en afbeeld-modaliteit voor waferuitlijnapplicaties. Met behulp van ultrageluid wordt een akoestische kopie van het verborgen tralie gemaakt welke, wanneer deze het oppervlak bereikt, vervolgens wordt gedetecteerd met conventionele optische diffractie.

Publications

This thesis is based on the following publications:

1 **S. Edward**, A. Antoncecchi, H. Zhang, H. Sielcken, S. Witte, and P. C. M. Planken, "Detection of periodic structures through opaque metal layers by optical measurements of ultrafast electron dynamics," Opt. Express **26**, 23380–23396 (2018) (**Chapter 4**).

2 H. Zhang, A. Antoncecchi, **S. Edward**, I. Setija, P. Planken, and S. Witte, "Unraveling phononic, optoacoustic, and mechanical properties of metals with light-driven hypersound," Phys. Rev. Appl. **13**, 014010 (2020) (**Chapter 5**).

3 **S. Edward**, H. Zhang, I. Setija, V. Verrina, A. Antoncecchi, S. Witte, and P. Planken, "Detection of hidden gratings through multilayer nanostructures using light and sound," Accepted in Phys. Rev. Appl. (2020) (**Chapter 6**).

4 **S. Edward**, H. Zhang, S. Witte, and P. Planken, "Role of surface roughness in photoacoustic detection of low amplitude buried grating," Under review (**Chapter 7**).

The author contributed to the following publications:

1 **S. Edward**, et al. and P. Planken, " Photoacoustics, thermal transport and electron dyanmics in thin film Ru," In Preparation.

2 V. Verrina, **S. Edward**, H. Zhang, A. Antoncecchi, S. Witte, and P. Planken, "Role of scattering by surface roughness in the photoacoustic detection of hidden micro-structures," Under review.

3 V. Verrina, **S. Edward**, H. Zhang, S. Witte, and P. Planken "Photo acoustic detection of low duty-cycle gratings through optically opaque layers," Under review.

4 A. Antoncecchi, H. Zhang, **S. Edward**, V. Verrina, P. Planken, and S. Witte, "Scanning pump-probe for sub-surface microscopy," Under review.

Acknowledgements

This thesis is a culmination of my Ph.D. work but also represents the end of an amazing and memorable period of my life. It was interesting, exciting, challenging, but also quite audacious. The best part: I never hated Mondays!!

Of course, such a wonderful experience could not have been possible without the help of my supervisor, Paul. Working under your supervision was a great learning experience. You gave me the freedom to do crazy stuff in the lab, and to you, no ideas were stupid. I could walk into your office anytime and discuss physics with you, which I think is a privilege that I always took for granted. Your enthusiasm for the subject and eagerness to learn is admirable. I appreciate your kindness, understanding, and the support you showed. You taught me how to be critical about my work, how to write a research article, and how to do science. Thank you for everything.

Stefan, although you became my co-supervisor only recently, you were always very helpful and supportive, even from the beginning of the Ph.D. I'm glad that his project was in collaboration with your group. Despite not being in your group, I believe you gave me the freedom to discuss the project with you at any time. Thanks for reading all of my manuscripts carefully and providing constructive criticism. An interesting aspect of working at ARCNL is the collaboration with ASML. This collaboration went very well, thanks to your efforts, Irwan. Every discussion I had with you was extremely fruitful and made me think deeper about my work and the physics underlying it. Your explanations of difficult concepts were always very clear and very helpful. In a way, you were like my third supervisor.

I'm fortunate that it was with you whom I started this project, Ale. You took me out with your friends on the first weekend I was here, you introduced me to your circle of friends, and you made me feel welcome in Amsterdam. It was so easy to work with you, despite yelling at each other occasionally (serious discussion ;)). You were there to help me every time I needed something, quite often, even without even asking. And of course, it's not easy to forget the amount of beer we had together. Don't change, ever! Vanessa, we both started our PhDs in the same group at roughly the same time. Although we worked on slightly different projects, we ended up working together, which was great. You helped me a lot with cleanroom-related work. You were such a great friend who was always there if I needed something. It was always fun to hang out with you after work, and very often, it was relaxing to have a conversation with you. Hao, the photoacoustic numerical model you developed was very helpful in understanding a lot of the measurements I did. Thank you for your patience and willingness to explain your codes.

Nishant, you made my integration into the group a very easy task. I very much enjoyed those late evening sessions with you in the lab. I learned a lot about THz science during our discussions. Martijn, it was great working with you. It was quite easy to be your daily supervisor, and I learned a lot from working with you. You were always understanding and a great person to work with. Guido, it was fun to have you in the group, and thanks for all of the help you provided during the final phase of my Ph.D. Nick Spook, you were of immense help during my first year. Thank you for being kind enough to help me whenever possible.

Building an experimental setup is challenging, even more when you have to start with an empty table and an empty lab. Thomas, having you as the group technician made my life a bit easier. I could walk into your office and ask for your help in making various things in the workshop. Your quick skills in the workshop helped me during the initial phase of my Ph.D. when we were setting up the lab. Nik and Reinout, thank you for helping me when Thomas was occasionally unavailable. During my time at ARCNL, I spent a significant amount of time in the AMOLF Cleanroom, fabricating hundreds of samples, (literally). It would not have been possible without the help of the cleanroom staff, especially Bob and Andries. You guys

helped me a lot with nanofabrication and were always there to answer any questions. Being next to AMOLF had many advantages, perhaps the main one being the use of their facilities. Thanks to everyone in the ICT and the electronics department for all your help. Duncan, all of the electronic devices you built worked perfectly for me. Also, thank you for explaining, in detail, the working principles behind these devices. Marco, thanks for designing and maintaining the data acquisition software.

One privilege of being at ARCNL was the ease of discussing science with different group leaders: Joost, Fred, Sonia, Peter, Oscar, and Kjeld. I'm grateful for answering my questions whenever I knocked on your doors. Marjan: thank you for helping with all administrative things.

Having friendly and warm people around you goes a long way in helping to endure a Ph.D. Maisie, it was great to have you as an office mate. You made the office lively with your cheerful and playful nature. Also, it was fun to argue with you and occasionally annoy you. Thanks a lot for all of the house parties, board game nights, and dinners that you and Randy organized. Of course, one party will always stand out. Randy, you were the Dutch friend who familiarised me with Dutch culture. Thanks a lot for translating the summary of this thesis into Dutch. John, although I met you only a year ago, it feels like you have been talking for five years non-stop. You became a close friend in such a short span, maybe because of all that time we spent at Maslow or in the US. Thank you for reading my thesis and for providing me with feedback. Fiona, thank you for proofreading as well and helping with the AFM whenever I asked you. You were very kind, supportive, and fun to be with. Neha, you are a friend I could ring up anytime and start a conversation. It was always comforting to have a chat with you over all the delicious food you cooked for me. Zhuang-Yan, I'm glad I met such an interesting person like you. You made life more colorful.

Certainly, life at ARCNL would have been dull and boring if it wasn't for a lot of amazing colleagues and friends. At the risk of forgetting some: Gorsel, Victor, Ruben, Lucas, Cristina, Tiago, Lars, and Ale T. It was great fun hanging out with you guys on many weekend evenings. I had a lot of fun and exciting conversations over lots of beers. You guys made my social life in Amsterdam vibrant and exciting. You guys kept ARCNL lively. Amelie,

Joris, Anne, Flippo, Sylvianne, Najmeh, Christos, Bo, Maarten, Zeudi, Jan, Feng-Chun, Zoi: you guys made my time at ARCNL more enjoyable. All of the foosball games and the borrels we had were real stress-busters.

Nikhil, Shyama, and John, you guys made me feel at home in Amsterdam. I enjoyed all the get-togethers we had, movies, board games, Kerala food, and all those long conversations. Namrata, you were a great inspiration to me, and always a source of constant motivation. All the trips we had together and the memories we shared will be forever with me. During my time in Amsterdam, I got to meet a lot of wonderful people with whom I share a lot of great memories. Marco, Caroline, Lorenzo, Masha, Jenny, Florian, Vishnu, Rakesh,.... I'm glad that our paths crossed. Ritwick Das and Deepak Mathur, I wouldn't be working in optics if I hadn't undertaken projects in your labs. Thank you for making the subject interesting and fun. Thanks to my friends from NISER, who was always a phone call away.

Lastly, my parents, appa, you were my first physics teacher. I won't forget when you taught me physics when I was 11, how you pushed me to go beyond my comfort zone, how you let me move away from home when I was 16. I know that wasn't easy for you. I know this thesis wouldn't have been possible if it wasn't for all those little decisions. I feel that this thesis means a lot more to you than it will ever mean to me. Amma, since I can remember, you taught me everything: math, science, moral values, and these days a bit of cooking. Thanks for being so lovely, caring, understanding, and for tolerating all my tantrums, even today. I can't begin to tell how much I'm thankful for having you both as my parents. Anna, you made our life more fun. Thanks for being such a loving, caring, and sweet little sister.